GRADUATE AERONAUTICAL LABORATORIES
CALIFORNIA INSTITUTE OF TECHNOLOGY

Premixed Hydrocarbon Stagnation Flames: Experiments and Simulations to Validate Combustion Chemical-Kinetic Models

Laurent J.-M. Benezech

Engineer's Thesis

JUNE 2008

Firestone Flight Sciences Laboratory

Guggenheim Aeronautical Laboratory

Karman Laboratory of Fluid Mechanics and Jet Propulsion

Pasadena

Premixed Hydrocarbon Stagnation Flames: Experiments and Simulations to Validate Combustion Chemical-Kinetic Models

Thesis by

Laurent Jean-Michel Benezech

In Partial Fulfillment of the Requirements

for the Degree of

Engineer

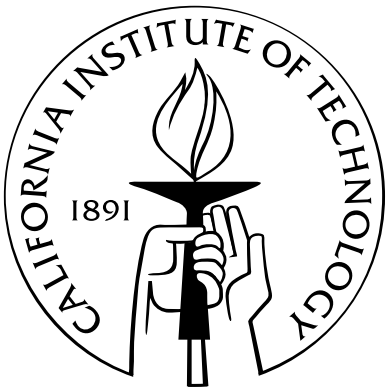

California Institute of Technology

Pasadena, California

2008

(Submitted May 30, 2008)

Acknowledgements

This work was carried out at the California Institute of Technology under the guidance of Professor Paul Dimotakis. I would like to thank him for providing everything I needed to carry out this work. I am especially grateful for his good advice, and because he cares about my education and always pushes me to get a better understanding. I am very grateful for the opportunity that I was given to work as the lead investigator on a challenging multidisciplinary project while developing project management skills, which prepared me very well for my next step in industry. I am also indebted to the other members of my committee, Professor Joseph Shepherd and Professor Daniel Meiron, for their constructive criticism of this thesis. Learning combustion from the class taught by Professor Joseph Shepherd and benefiting from his advice were very valuable to the work presented here.

I would like to thank Assistant Professor Jeff Bergthorson specially, for providing me such a nice starting experimental set-up. During my first year here, I learned a lot and received constant support from him, as an advisor as well as a friend. Even after he left to become Assistant Professor at McGill University in the department of Mechanical Engineering, he still contributed to this project with his guidance and support.

I would like to thank Professor David Goodwin for the availability and continuous development of the CANTERA software package. I am grateful for the frequent advice that I received from Dr. Kazuo Sone and Georgios Matheou regarding simulation issues, and for the discussions about experimental issues with Dr. Aris Bonanos. Dr. Kazuo Sone also helped me by producing some jet simulations discussed in this work. I am indebted to Georgios Matheou, Jan Lindheim, and Dr. Dan Lang for their availability and efficiency in maintaining the computational resources of our group. Dr. Dan Lang's expertise and assistance with digital imaging, electronics, lasers, data-aquisition, and all computer matters (among which were key backups) are very much appreciated. I would also like to acknowledge Garrett Katzenstein for his technical advice on mechanical designs. The drawings would be nothing without Joe Haggerty, Bradley St. John, and Ali Kiani from the Aeronautics machine shop, whose work is remarkable. Administrative support from Christina Mojahedi is appreciated and her presence as a friend is even more appreciated.

This work was funded by the Air Force Office of Scientific Research (AFOSR grants FA9550-04-1-0020, FA9550-07-1-0091, & FA9550-04-1-0253), with additional funding through the Caltech

Northrop Chair, and the computing resources were supported in part by NSF grant EIA-0079871. The support from these grants is gratefully acknowledged.

I thank my friend, Adeline, for her constant support and encouragement despite the distance.

I thank my family who have always been present when emotional support was needed.

Abstract

A methodology based on the comparison of flame simulations relying on reacting flow models with experiment is applied to C_1–C_3 stagnation flames. The work reported targets the assessment and validation of the modeled reactions and reaction rates relevant to (C_1–C_3)-flame propagation in several detailed combustion kinetic models. A concensus does not, as yet, exist on the modeling of the reasonably well-understood oxidation of C_1–C_2 flames, and a better knowledge of C_3 hydrocarbon combustion chemistry is required before attempting to bridge the gap between the oxidation of C_1–C_2 hydrocarbons and the more complex chemistry of heavier hydrocarbons in a single kinetic model.

Simultaneous measurements of velocity and CH-radical profiles were performed in atmospheric propane(C_3H_8)- and propylene(C_3H_6)-air laminar premixed stagnation flames stabilized in a jet-wall configuration. These nearly-flat flames can be modeled by one-dimensional simulations, providing a means to validate kinetic models. Experimental data for these C_3 flames and similar experimental data for atmospheric methane(CH_4)-, ethane(C_2H_6)-, and ethylene(C_2H_4)-air flames are compared to numerical simulations performed with a one-dimensional hydrodynamic model, a multi-component transport formulation including thermal diffusion, and different detailed-chemistry models, in order to assess the adequacy of the models employed. A novel continuation technique between kinetic models was developed and applied successfully to obtain solutions with the less-robust models. The 2005/12 and 2005/10 releases of the San Diego mechanism are found to have the best overall performance in C_3H_8 & C_3H_6 flames, and in CH_4, C_2H_6, & C_2H_4 flames, respectively.

Flame position provides a good surrogate for flame speed in stagnation-flow stabilized flames. The logarithmic sensitivities of the simulated flame locations to variations in the kinetic rates are calculated via the "brute-force" method for fifteen representative flames covering the five fuels under study and the very lean, stoichiometric, and very rich burning regimes, in order to identify the most-important reactions for each flame investigated. The rates of reactions identified in this manner are compared between the different kinetic models. Several reaction-rate differences are thus identified that are likely responsible for the variance in flame-position (or flame-speed) predictions in C_1–C_2 flames.

Contents

List of Figures

List of Tables

Chapter 1

Introduction

A number of chemical-kinetic mechanisms are available in the literature, each predicting different flame behavior in various regimes. The imbalance between the hundreds of constants (each with an associated uncertainty) used in each model and the small number of data sets available to validate such mechanisms leads to indeterminacies and non-uniqueness in the various models (Frenklach et al. 1992). Two different paths can be followed in the development of such mechanisms. One involves the optimization of a base mechanism to multiple data sets of diverse parameters. The GRI-Mech initiative (Smith et al.) successfully applied such optimization techniques to a dataset of laminar flame speeds, ignition delay times, and species profiles obtained from laminar flames, shock-tube experiments, and flow reactors. Thus the current benchmark mechanism for natural gas combustion was created: GRI-Mech 3.0. However, the resulting improved agreement to a finite set of experiments comes at a price: such a mechanism must be regarded as interpolative and its use is not recommended outside the domain of its optimization targets. Such a mechanism should therefore not be used as the basis upon which to build a model for larger hydrocarbon fuels. Mechanisms such as Leeds (Hughes et al. 2001) or the Battin-Leclerc *et al.* C_0–C_2 mechanism (Barbe et al. 1995, Bauge et al. 1997) follow a different approach: recommended rate data are used wherever possible with minimum modifications. In order to make progress towards a universal model of flame kinetics that would not only reconcile diverse experimental data but also be predictive, high-accuracy measurements of multiple quantities (flame speeds, species concentrations and peak positions, ignition delays and temperatures, extinction strain-rates,...) are needed in different environments (laminar flames, reactors, shock tubes) under comprehensive conditions (temperature, pressure, fuel, burning regime,...) for validation. Because of the complexity of these models, consistency checks are essential to check that the reaction rate coefficients, thermodynamic, and transport data used are consistent (like in Wang & Frenklach 1997), and to check that the experimental data sets used to build the mechanism are mutually consistent (Feeley et al. 2004). Comparisons of mechanisms are also needed, whether via comparisons of their kinetic data (Rolland & Simmie 2004); or based on their different predictions related to flame propagation, using criteria such as the CH-peak position in premixed

stagnation flames (Bergthorson et al. 2005a, Bergthorson & Dimotakis 2007, Benezech et al. 2008); ignition and extinction, using criteria such as ignition and extinction strain rates in non-premixed flames (Egolfopoulos & Dimotakis 2001); or major/minor species concentrations in flames, e.g., concentrations of acetylene, the principal species responsible for soot growth, or polycyclic aromatic hydrocarbons, PAHs, the presumed soot precursors (Appel et al. 2000).

Stagnation flames stabilized in a jet-wall configuration are studied in the present work. The flow near the jet axis can be approximated by the one-dimensional model by Kee et al. (1989, 2003), making detailed simulations achievable in a reasonable amount of time. The axisymmetric two-dimensional flame simulations performed by Sone (2007) showed that flame speed is sensitive to even slight flame front curvature as well as to its finite extension in the radial direction. Although these two-dimensional effects are discernible, they remain small in the nearly-flat flames investigated in the present work. The boundary conditions needed to simulate the flow can be measured accurately in the stagnation-wall geometry, thus enabling reliable comparison between experiment and simulation Bergthorson et al. (2005a). The jet-wall configuration was chosen over the conventional counter-flow apparatus because it allows for the precise specification of the stagnation-plane location and boundary conditions (temperature, no-species flux), which reduces uncertainty in numerical simulations. In an opposed-jet configuration, small mismatches or changes in the two jet-exit velocities can result in a displacement, or movement, of the stagnation plane. Moreover, the stagnation-plane location cannot be reliably specified in opposed-jet experiments from particle velocimetry measurements because of poor resolution of small velocity values, or particle inertia effects. The jet-wall geometry is also found to yield more stable flames than the opposed-jet geometry (Egolfopoulos et al. 1997).

Of the three key parameters that affect kinetics the most, i.e., pressure, fuel, and burning regime, the dependence of atmospheric-pressure flames on variations of both fuel (methane CH_4, ethane C_2H_6, ethylene C_2H_4, propane C_3H_8, & propylene C_3H_6) and burning regime (from very lean to very rich, by varying the equivalence ratio Φ) are explored. Simultaneous measurements of velocity and CH-radical profiles are performed in C_3H_8 & C_3H_6 flames by particle tracking velocimetry (PTV) and by CH planar laser-induced fluorescence (PLIF), respectively. Comparisons are made between these measurements in C_3 flames, similar measurements in CH_4, C_2H_6, & C_2H_4 flames (Bergthorson & Dimotakis 2007), and one-dimensional predictions using the CANTERA software package (Goodwin 2003), a multi-component transport formulation including thermal diffusion (Kee et al. 2003), & various chemical-kinetic models. Relatively few comparisons of stagnation-flame simulations with experiment, such as a previous investigation of C_1–C_2 flames (Bergthorson & Dimotakis 2007), are available. Even fewer comparisons are available for C_3H_8 and C_3H_6, which capture more of the chemical kinetics of heavier hydrocarbons. The present work adds C_3-flame data and detailed simulations analogous to previous studies on C_3 laminar flame speeds (Vagelopoulos et al. 1994,

Davis et al. 1999, Jomaas et al. 2005). The present work also uses sensitivity analysis to guide a detailed comparison of the reaction-rate parameters used in fifteen different mechanisms, addressing CH_4, C_2H_6, and C_2H_4 flames in order to assess the differences in the various mechanisms that lead to the variation observed in the model predictions of a set of experimental stagnation-flame data (Bergthorson 2005b, Bergthorson & Dimotakis 2007).

The purpose of the present work is:

- to validate a low-scatter, high-spatio-temporal resolution velocimetry technique that does not disturb flames (i.e., particle-tracking velocimetry, PTV) in non-reacting impinging jets against the previous investigations of Bergthorson et al. (2005b).
- to document the performance of the PTV technique in C_3 flames.
- to document a practical continuation technique to transition from a solution obtained with a robust mechanism to a new solution obtained with a less-robust mechanism.
- to present a new experimental data set (velocity and CH-radical profiles) in atmospheric C_3H_8 and C_3H_6 premixed stagnation flames, available, upon request, for use as validation or optimization targets, following the collaborative-data approach (Frenklach et al. 2004).
- to validate four recent detailed kinetic models against these C_3-flame data.
- to validate fifteen detailed kinetic models against CH_4-, C_2H_6-, and C_2H_4-flame data.
- to identify the reaction rates that likely contribute to the variance in the C_1–C_2 predictions from the fifteen mechanisms investigated by coupling sensitivity analysis with a comparison of the kinetic rates among mechanisms.

Chapter 2

Chemical-kinetic models

2.1 List of chemical-kinetic models

Sixteen recent chemical-kinetic models (also called mechanisms), with their associated thermodynamic and transport data, are used in the present work.

- G1, G2, and G3

The GRI-Mech mechanism was developed and optimized to model natural-gas combustion, including NO formation and reburn chemistry in its more recent releases. Three versions are used in the present work: GRI-Mech 1.2 (Frenklach et al. 1995, Frenklach et al.), hereafter referred to as "G1" (32 species and 177 reactions); GRI-Mech 2.11 (Bowman et al., Frenklach et al.), hereafter referred to as "G2" (49 species and 279 reactions); and GRI-Mech 3.0 (Smith et al.), hereafter referred to as "G3" (53 species and 325 reactions). The GRI-Mech mechanism will be referred to as "GRI", when no distinction is made between the releases. The parameters of the reactions present in G1 were not changed in G2, except for one reaction that is important in prompt NO formation and that does not alter the C-H-O chemistry of methane (CH_4) combustion. G2 expands G1 by including nitrogen chemistry relevant to natural-gas chemistry and reburning. The better description of NOx formation and removal in natural gas flames in G2 cost a loss in reliability regarding C-H-O chemistry compared with G1. G3 differs from G2 in that kinetics and target data have been updated, improved, and expanded. C_2 oxidation products have been added: acetaldehyde (CH_3CHO) and vinoxy (CH_2CHO) chemistry are included to better describe ethylene (C_2H_4) oxidation. New formaldehyde (H_2CO) and NO formation & reburn targets are also included. The two older releases, G1 & G2, and the C_2H_4 flame predictions by G3 are included for reference only, as this mechanism is widely relied upon in the literature. Natural gas contains C_3H_8 (and some higher hydrocarbons that may be approximately represented by C_3H_8), therefore a minimal set of C_3H_8 kinetics is included to model this species, as a minor constituent only. As a consequence, G3 simulations of C_3H_8 flames are also included for reference only. G3 simulations of C_3H_6 flames are not included because C_3H_6 is not present in the mechanism.

- DLW

The Davis-Law-Wang mechanism (Davis et al. 1999), hereafter referred to as "DLW", was developed to describe the combustion of C_3 hydrocarbons. It is largely based on GRI-Mech 1.2 (Frenklach et al. 1995, Frenklach et al.), which was further expanded and validated against ethylene (C_2H_4) and acetylene (C_2H_2) flame data in particular, with modifications and additions made concerning C_3 kinetics. It was shown (Davis et al. 1999) that this mechanism could reconcile a significant body of combustion data for propylene (C_3H_6), propyne (C_3H_4 or $H_3C\text{-}C{\equiv}CH$, also called methylacetylene), allene (C_3H_4 or $H_2C{=}C{=}CH_2$), and propane (C_3H_8). DLW relies on 71 species and 469 reactions.

- ABF

The detailed kinetic model for soot formation from Appel-Bockhorn-Frenklach (Appel et al. 2000) consists of two principal components: gas-phase chemistry and soot-particle dynamics. The gas-phase submodel is key as the flame structure it predicts is used as an input by the soot-particle dynamics submodel. Three versions of the gas-phase submodel are available (Appel et al. 2000) for 90 torr, 1 bar, and 10 bar pressures, respectively. The 1 bar version, hereafter referred to as "ABF" (relying on 101 species and 544 reactions), is used in the present work on atmospheric-pressure flames. ABF is an updated version of the Wang-Frenklach mechanism (Wang & Frenklach 1997) that relies on 99 species and 527 reactions. The Wang-Frenklach mechanism can be used to model the oxidation of CH_4, ethane (C_2H_6), C_2H_4, and C_2H_2 at flame temperatures. It is based on GRI-Mech 1.2 (Frenklach et al. 1995, Frenklach et al.) and a consistent set of rate coefficients, thermodynamic data, and transport data for reactions of aromatics developed by Wang and Frenklach. ABF improves on the underprediction of two-, three-, and four-ring aromatic species seen in the Wang-Frenklach mechanism (Wang & Frenklach 1997).

- WL

The Wang-Laskin comprehensive reaction model (Wang & Laskin 1998), hereafter referred to as "WL", of C_2H_4 and C_2H_2 combustion was motivated by progress in the fundamental reaction kinetics relevant to C_2H_4 and C_2H_2 oxidation, and noticeably in the reaction kinetics of the vinyl radical (C_2H_3). In this model, C_1–C_2 chemistry is largely based on GRI-Mech 1.2 (Frenklach et al. 1995; Frenklach et al.). The reaction kinetics of C_2H_4 and C_2H_2 are based on work reported previously (Sun et al. 1996, Wang & Frenklach 1997, Laskin & Wang 1999). The C_3 kinetics were taken from DLW (Davis et al. 1999). The kinetic model retains a reasonable number of C_4 species to ensure proper simulation under fuel-rich conditions. Thus WL predicts the combustion properties of both C_2 and C_3 fuels. WL relies on 75 species and 529 reactions.

- S1, S2, S3, S4, and S5

The San Diego mechanism has been developed to model the combustion of C_1–C_3 hydrocarbons. In this approach, the numbers of species and reactions are kept to the minimum needed to describe the systems and phenomena addressed, thereby minimizing as much as possible the uncertainties in

the rate parameters employed. Five versions are used in the present work: "S1" (2003/08 release with 39 species and 173 reactions), "S2" (2005/03 release with 39 species and 175 reactions), "S3" (2005/06 release with 40 species and 175 reactions), "S4" (2005/10 release with 40 species and 180 reactions), and "S5" (2005/12 release with 46 species and 235 reactions). The San Diego mechanism will be referred to as "SD", when no distinction is made between releases. As shown below, S4 and S5 yield very similar results in C_1–C_2 flames, which is not surprising since the reaction rates were unchanged from S4 to S5 and only an ethanol reaction set was added.

- MRN

The Marinov mechanism (Marinov 1998), hereafter referred to as "MRN", for ethanol (C_2H_5OH) combustion was developed through tests against C_2H_4, C_2H_2, and C_2H_5OH flames. The detailed chemical-kinetic model was assembled using reaction submechanisms developed previously for hydrogen (H_2) (Marinov et al. 1996b), CH_4 (Marinov et al. 1996a), C_2H_4 (Marinov & Malte 1995, Castaldi et al. 1996), C_2H_6 (Marinov et al. 1996a), and C_3H_8 oxidation (Marinov et al. 1997). MRN relies on 57 species and 383 reactions.

- DAG

The Dagaut et al. full mechanism (Dagaut & Nicolle 2005), hereafter referred to as "DAG" (relying on 97 species and 732 reactions), is an update to the C_1–C_3 Tan et al. mechanism (Tan et al. 1994) that relies on 78 species and 473 reactions, and is a comprehensive mechanism developed to describe the oxidation of CH_4, C_2H_4, C_2H_2, C_3H_8, and C_3H_6, both individually and as blends. The base set of DAG is the detailed chemical-kinetic reaction mechanism developed for the modeling of NO reburning by C_1–C_4 hydrocarbons, the oxidation of liquefied petroleum gas (LPG) (Dagaut & Hadj 2003) and of various fuels from methane to kerosene (Dagaut 2002). It includes both low and high temperature combustion chemistry.

- BLB

A particular effort was made to build the C_0–C_2 Battin Leclerc-Barbe mechanism (Barbe et al. 1995, Bauge et al. 1997), hereafter referred to as "BLB", in a comprehensive way. This mechanism was generated in a systematic way; it includes all the unimolecular or bimolecular reactions involving radicals or molecules containing less than three carbon atoms. Thus, BLB constitutes not only a well-balanced scheme for the oxidation of CH_4 and C_2H_6, but also the starting point and the basic kernel for further development and improvement in the area of combustion processes and oxidation of higher hydrocarbons. The kinetic data were preferentially those proposed by Baulch et al. (Baulch et al. 1994) or Tsang et al. (Tsang & Hampson 1986, Tsang 1987), and are consistent with the thermochemistry. BLB relies on 64 species and 439 reactions.

- BL

The C_3 mechanism of Battin-Leclerc et al. (Gueniche et al. 2006), hereafter referred to as "BL", models the oxidation of C_3–C_4 unsaturated hydrocarbons with an accurate description of the reac-

tions of allene ($H_2C{=}C{=}CH_2$), propyne ($H_3C\text{-}C{\equiv}CH$), and propargyl ($HC{\equiv}C\text{–}CH_2\text{–}$) radicals. BL relies on 91 species and 686 reactions.

- KON

The C_1–C_3 Konnov mechanism (Konnov 2000), hereafter referred to as "KON", is a detailed reaction mechanism for small hydrocarbon combustion. It was tested in a wide range of experimental conditions for H_2, CO, CH_4, C_2H_6, and C_3H_8 flames. KON relies on 127 species and 1207 reactions.

The five mechanisms: G3, DLW, S5, BL, & KON are used in the C_3 flames study (see Chapter 5) and the fifteen mechanisms: G1, G2, G3, DLW, ABF, WL, S1, S2, S3, S4, S5, MRN, DAG, BLB, & KON are used in the C_1–C_2 flames study (see Chapter 6).

Except for G1 and ABF, the number of species and the number of reactions present in a mechanism follow a linear relation (see Fig. 2.1). A linear fit was performed through all points in Fig. 2.1 except S1, S2, and S3 that are represented by S4. The approximate linear relationship found was: Number of Reactions $\simeq 9.7 \times$ Number of Species - 196, and is also plotted in Fig. 2.1. G1 is an old release, which may explain its different ratio between number of reactions and number of species. As for ABF, intended for use with a soot particle dynamics model, its relatively larger number of species is not surprising given that heavier hydrocarbons play an important role in soot formation (Wang & Frenklach 1997, Appel et al. 2000).

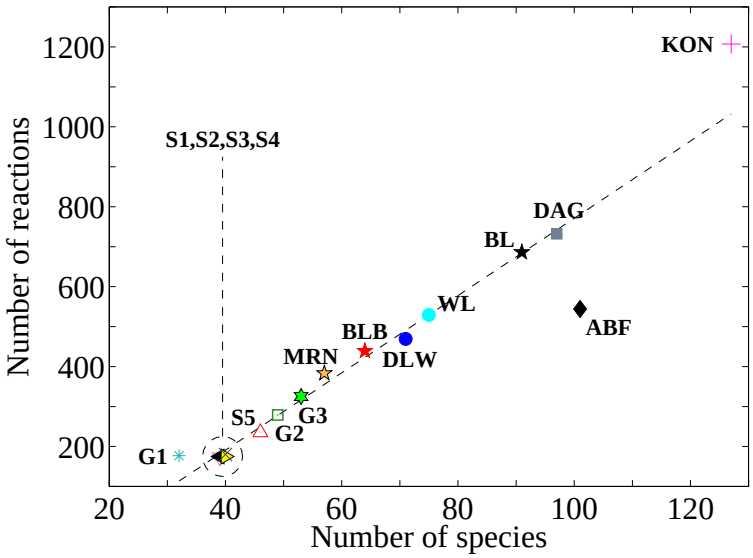

Figure 2.1: Comparison of the numbers of species and reactions for the sixteen mechanisms under study.

2.2 Continuation technique between chemical-kinetic models

Simulations would only rarely converge with the mechanisms MRN, DAG, BLB, BL, and KON, whereas simulations converge with the more-robust mechanisms G1, G2, G3, DLW, ABF, WL, S1, S2, S3, S4, and S5. Therefore, a continuation technique was developed to transition from a solution obtained with a robust mechanism to a new solution obtained with a less-robust mechanism, as recommended by P. Dimotakis (private communication).

To enable a converged simulation with the mechanism where no convergence could occur directly before, $mech_{\mathrm{no-cv}}$, a hybrid mechanism, $mech_{\mathrm{hybrid}}(\lambda)$, is used that incorporates the kinetic model adopted in both $mech_{\mathrm{no-cv}}$ and another mechanism for which the simulation converged, $mech_{\mathrm{cv}}$, in such a manner that each reaction rate from $mech_{\mathrm{cv}}$ is multiplied by (1-λ) and each reaction rate from $mech_{\mathrm{no-cv}}$ is multiplied by λ. Thus, a smooth transition is enabled between the kinetic model present in $mech_{\mathrm{cv}}$ ($mech_{\mathrm{cv}} \sim mech_{\mathrm{hybrid}}(\lambda{=}0)$) and the kinetic model present in $mech_{\mathrm{no-cv}}$ ($mech_{\mathrm{no-cv}} \sim mech_{\mathrm{hybrid}}(\lambda{=}1)$), by varying the parameter λ from 0 to 1 in increments as small as necessary for reconvergence.

In practice, the thermodynamic and transport data in $mech_{\mathrm{hybrid}}$ are chosen to be those in $mech_{\mathrm{no-cv}}$, and two blocks of reactions (with their associated reaction rates) are used in $mech_{\mathrm{hybrid}}$: firstly, the block of reactions (and associated reaction rates) present in $mech_{\mathrm{cv}}$, and secondly, the block of reactions (and associated reaction rates) present in $mech_{\mathrm{no-cv}}$. Some modifications are brought to the first block of reactions: the species names are modified for consistency when necessary, and reactions involving species not present in $mech_{\mathrm{no-cv}}$ are omitted. An external simulation script gains access to $mech_{\mathrm{hybrid}}$, and has the ability to multiply the reaction rates in the first block by (1-λ) and the reaction rates in the second block by λ. Thus, the hybrid mechanism, $mech_{\mathrm{hybrid}}$, needs only be constructed once (one hybrid mechanism for each less-robust mechanism), and can be used for any flame.

Finally, a converged simulation obtained with $mech_{\mathrm{hybrid}}(\lambda \sim 1)$ can be used as initialization for a simulation that uses $mech_{\mathrm{no-cv}}$, which, this time, will be successful. A summary of the procedure follows:

(i) choice of a mechanism $mech_{\mathrm{cv}}$

(ii) elaboration of $mech_{\mathrm{hybrid}}$ (requires less time if $mech_{\mathrm{cv}}$ is similar to $mech_{\mathrm{no-cv}}$)

(iii) converged simulation, $sim_{\lambda=0}$, of the flame, from scratch, using $mech_{\mathrm{hybrid}}(\lambda{=}0)$

(iv) march towards $\lambda \sim 1$: converged simulations, sim_{λ_n}, initialized with $sim_{\lambda_{n-1}}$, where the increments between the λ_n are as small as necessary to get reconvergence

(v) converged simulation with $mech_{\mathrm{no-cv}}$, initialized with $sim_{\lambda\sim1}$.

Chapter 3

Non-reacting impinging jets

Impinging jets were chosen to validate the new velocimetry technique. Particle-tracking velocimetry (PTV) images were recorded (see sample images shown in Figs. A.4a–f), and the Bernoulli velocity, U_{B}, was determined concurrently from the static pressure drop, Δp, across the nozzle contraction, for different Reynolds numbers, Re (Bergthorson et al. 2005b).

$$U_{\mathrm{B}} = \sqrt{\frac{2\,\Delta p/\rho}{1-(d/d_{\mathrm{P}})^4}} \quad ,$$

where $\rho = 1.2\,\mathrm{kg/m^3}$ is the density of the jet fluid (air), $d = 0.99\,\mathrm{cm}$ is the diameter of the nozzle exit, and $d_{\mathrm{P}} = 3.81\,\mathrm{cm}$ is the plenum diameter. Experiments were conducted at Reynolds numbers, $Re \equiv U_\infty \rho d/\mu = 407$, 708, 1409, 2524, 5049, and 9120. $\mu = 1.84\,10^{-5}\,\mathrm{kg/(m.s)}$ is the dynamic viscosity of the jet fluid (air). The nozzle-to-plate separation distance (normalized by the nozzle diameter) is $L/d = 1.5$ so that the free jet regime (where the velocity is constant) is recovered.

For cold impinging jets, an error function represents the profiles (Bergthorson et al. 2005b):

$$\frac{u(x)}{U_\infty} = \mathrm{erf}\Big[\alpha\ (\frac{x}{d} - \frac{\delta}{d})\Big] \quad ,$$

where U_∞ is suggested to be U_{B}, α is a strain-rate free parameter, and x is the distance from the wall. δ/d is a scaled-offset length, which is proportional to the scaled wall boundary-layer thickness, and can be related to α, such that

$$\frac{\delta}{d}(Re,\alpha) = 0.755\ \sqrt{\frac{1}{Re\cdot\alpha}} \quad .$$

The error-function fits to the experimental data with the two free parameters U_∞ and α represent well the velocity data for all Reynolds numbers investigated (see Figs. 3.1a–f). U_{B} is shown on these figures and is in agreement with U_∞ at all Reynolds numbers except the smallest: $Re = 407$. This is because the uncertainty in the offset pressure (see error bar on U_{B} on Fig. 3.1a) is not negligible

for such low velocities. From $Re = 708$, the uncertainty in the offset pressure is negligible ($< 0.8\,\%$ of $U_{\rm B}$ for $Re = 708$ (see error bar on $U_{\rm B}$ on Fig. 3.1b), and $< 0.1\,\%$ of $U_{\rm B}$ for $Re \geq 1409$).

Table 3.1 shows the fit parameters and resulting scaled rms errors, $\epsilon_{\rm rms}/U_\infty$ ($\lesssim 1\,\%$). The values of α seem to be consistent with those previously found in Bergthorson et al. (2005b) (see Table 3.2) for the low Re range, where only one free parameter had been used in the error-function fit (U_∞ was chosen equal to $U_{\rm B}$).

Figures 3.2a and 3.2b show the influence of Re on the fitted velocity profiles. From the axisymmetric-viscous simulations using the spectral element method (Patera 1984) performed by K. Sone that give us nozzle-exit velocity profiles (see Fig. 3.3), the jet momentum diameter (Dahm & Dimotakis 1987),

$$d^* \equiv \frac{2\,\dot{m}_0}{\sqrt{\pi\,\rho_\infty\,J_0}}$$

can be calculated (see results in Table 3.3), where

$$\dot{m}_0 \equiv 2\,\pi\,\rho_0 \int_0^\infty u_0(r)\,r\,dr$$

and

$$J_0 \equiv 2\,\pi\,\rho_0 \int_0^\infty u_0^2(r)\,r\,dr$$

are the jet mass and momentum fluxes at the jet nozzle, respectively, ρ_∞ is the density of the entrained reservoir fluid far from the jet, ρ_0 is the nozzle-fluid density (in our experiments $\rho_\infty = \rho_0 = \rho_{\rm air}$), and u_0 is the nozzle-exit axial velocity. The $Re = 5049$ and $Re = 9120$ simulations were not performed because of their larger computational cost. These simulations at higher Re require a higher resolution, and therefore also smaller time steps. Small time steps are a source of instability (private communication with K. Sone) because the right hand side of the pressure Poisson equation (Eq. 2.45b in Sone 2007) approaches 0/0. Although simulations in the literature that use the spectral element method are typically investigating flows at $Re \lesssim 3000$, the non-reacting impinging jet $Re = 5049$ and $Re = 9120$ simulations are probably possible with careful construction and distribution of the elements.

Even scaled by the jet momentum diameter (see Fig. 3.2b), the Re effect on the axial-velocity field is still significant. A power fit, $\alpha = \alpha_\infty + C\,/\,Re^n$, was used to characterize the dependence of the strain-rate parameter α on Re (see Fig. 3.4), using the values in Table 3.1. The values of the constants were found to be: $\alpha_\infty = 1.66$ (smaller than the value of 1.775 found in Bergthorson et al. 2005b, where data up to $Re = 1400$ only had been used), $C = 127$, and $n = -0.885$.

After validating the PTV velocimetry technique in the investigation of non-reacting impinging jets, the PTV technique was used to measure axial-velocity profiles in the C_3 stagnation flames studied in Chapter 5.

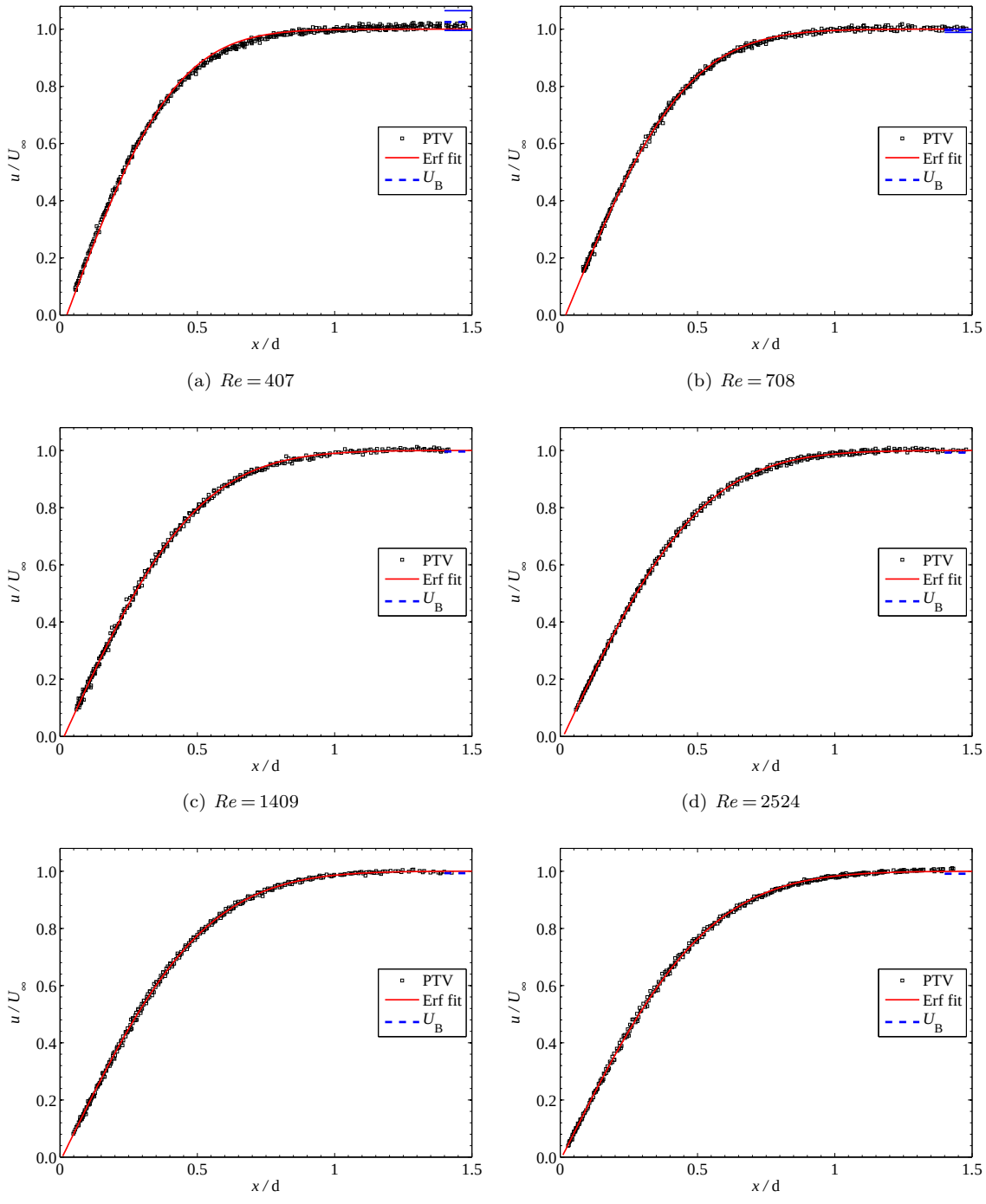

(a) $Re = 407$ (b) $Re = 708$

(c) $Re = 1409$ (d) $Re = 2524$

(e) $Re = 5049$ (f) $Re = 9120$

Figure 3.1: Comparison of error-function fits to experimental data.

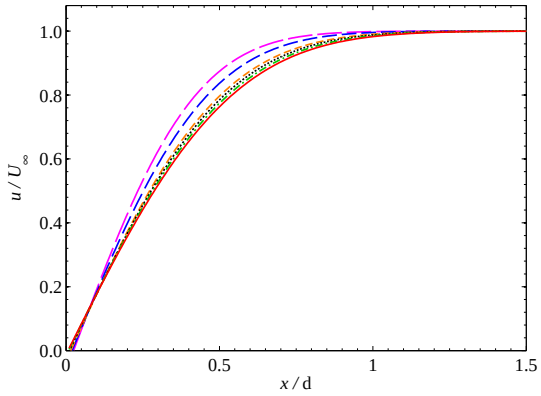

(a) The axial distance from the plate is normalized by the nozzle diameter, d.

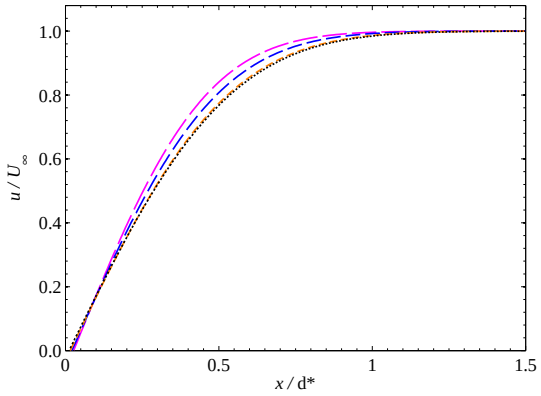

(b) For each Re, the axial distance from the plate is normalized by the corresponding jet momentum diameter d^*. (Calculated from simulations performed by Kazuo Sone at all Re but 5049 and 9120.)

Figure 3.2: Influence of Re on the fitted velocity profiles: $Re = 407$ (long-dashed line), $Re = 708$ (medium-dashed line), $Re = 1409$ (dashed line), $Re = 2524$ (dotted line), $Re = 5049$ (dash-dotted line), and $Re = 9120$ (solid line).

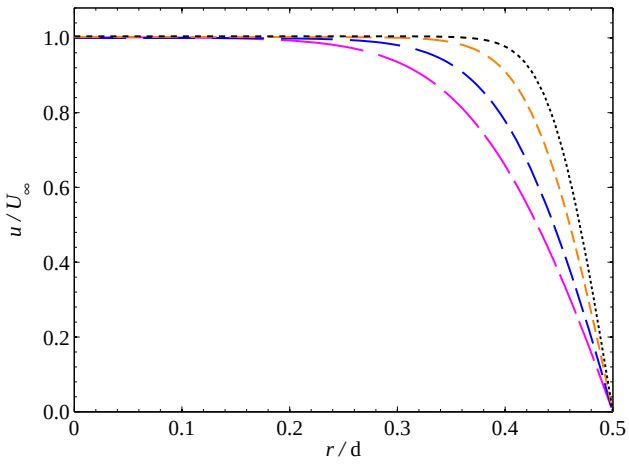

Figure 3.3: Influence of Re on nozzle-exit velocity profile: $Re = 407$ (long-dashed line), $Re = 708$ (medium-dashed line), $Re = 1409$ (dashed line), and $Re = 2524$ (dotted line). (Simulations performed by Kazuo Sone.)

Re	α	U_∞	$\epsilon_{\mathrm{rms}}/U_\infty$	$(U_\infty - U_\mathrm{B})/U_\infty$
407	2.28	0.63	0.011	-0.025
708	2.05	1.09	0.007	0.003
1409	1.85	2.17	0.008	0.004
2524	1.79	3.89	0.005	0.008
5049	1.74	7.78	0.008	0.007
9120	1.69	14.05	0.006	0.009

Table 3.1: Error-function fit parameters and rms error ϵ_{rms} of fits to experimental data.

Re	$\alpha_{\mathrm{Bergthorson}}$	$\epsilon_{\mathrm{rms,Bergthorson}}/U_{\mathrm{B,Bergthorson}}$
400	2.21	0.017
700	2.00	0.010
1400	1.88	0.011

Table 3.2: Error-function fit parameter and rms error ϵ_{rms} of fits to experimental data. Extracted from Bergthorson et al. (2005b).

Re	d^*
407	0.9182
708	0.9329
1409	0.9489
2524	0.9598

Table 3.3: Influence of Re on jet momentum diameter d^*. (Calculated from simulations by Kazuo Sone.)

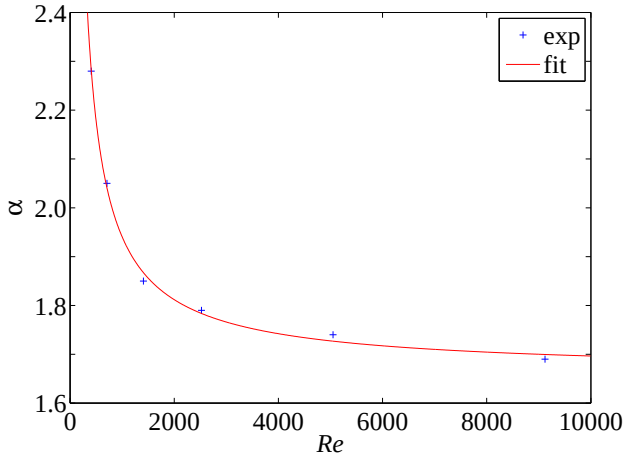

Figure 3.4: Dependence of α on Re.

Chapter 4

Numerical method

4.1 Stagnation-flame simulations

The axisymmetric premixed flame simulations described in Chapters 5 and 6 below are performed with the CANTERA reacting-flow software package (Goodwin 2003), using the one-dimensional model from Kee et al. (1989, 2003) validated against non-reacting impinging-jet experiments and axisymmetric two-dimensional direct numerical simulations in Bergthorson et al. (2005b). The velocity and velocity gradient are set to zero at the stagnation wall, $x = 0$ mm (no-penetration and no-slip conditions), and are specified at the inlet: ~ 1 mm upstream of the flame. The results are not found to be sensitive to this choice (Bergthorson 2005a, Section 3.1.2). The fluid-velocity and velocity-gradient values specified at the inlet are determined from the experimental particle-velocity profile (Bergthorson et al. 2005a), taking into account the lag of the tracer particles (Bergthorson & Dimotakis 2006). The inlet composition, inlet temperature, and stagnation-wall temperature are specified from measurements of fuel & air volumetric flow rates and from temperature measurements, respectively. A no-flux (multi-component with thermal diffusion) boundary condition for species is applied at the wall. The boundary conditions for each experiment are reported in Table D.1.

The simulations use a multi-component transport model that includes thermal diffusion (Kee et al. 2003) and different chemical-kinetic mechanisms used with their associated thermodynamic and transport data. The C_3H_8 and C_3H_6 flame simulations in Chapter 5 were performed with five mechanisms: G3, DLW, S5, BL, and KON. G3 simulations of C_3H_8 flames are shown for reference only (see Chapter 2), and G3 simulations of C_3H_6 flames are not included because C_3H_6 is not present in the mechanism. The CH_4, C_2H_6, and C_2H_4 flame simulations in Chapter 6 were performed with fifteen mechanisms: G1, G2, G3, DLW, ABF, WL, S1, S2, S3, S4, S5, MRN, DAG, BLB, and KON. C_2H_4-flame simulation results using G1, G2, and G3 are shown for reference only (see Chapter 2).

4.2 Particle-tracking corrections

Particle-tracking corrections are applied to the simulated velocity (u_{fluid}) profile. First, the simulated particle-velocity profile is determined by including the effects of particle inertia and thermophoresis (Bergthorson & Dimotakis 2006). Secondly, the modeled-particle tracking velocity ($u_{\text{modeled}-\text{PT}}$) profile is calculated that also accounts for the finite temporal resolution of the velocimetry technique (Bergthorson & Dimotakis 2006), characterized by the finite time interval, Δt, between two successive particle positions. $\Delta t = 1 \,/\, \nu_{\text{c}}$ (ν_{c} is the PSV chopper wheel frequency employed) or $1 \,/\, \nu_{\text{p}}$ (ν_{p} is the PTV laser repetition rate employed) when particle-streak velocimetry (PSV) or particle-tracking velocimetry (PTV) is used, respectively. Thus, the modeled-PT velocity profile is a prediction of the measured PSV or PTV profile.

Chapter 5

Premixed laminar C_3H_8- and C_3H_6-air stagnation flames: experiments and simulations with detailed kinetic models

5.1 Introduction

Atmospheric-pressure stagnation flames had been studied at variable stoichiometry for C_1–C_2 fuels: CH_4, C_2H_6, and C_2H_4 (Bergthorson & Dimotakis 2007). Because of the hierarchical nature of combustion (Gardiner-Jr. 1999), a next step is the investigation of C_3H_8 and C_3H_6 whose oxidation is more representative of that of heavier hydrocarbons, and for which few data are available.

5.2 Experimental method

A co-flow nozzle system is used to generate a combustible gas mixture (premixed fuel and air) jet of diameter, $d = 9.9\,\text{mm}$, impinging on a temperature-controlled (water-cooled) stagnation plate. The inert gas co-flow stabilizes and lifts the flame off the nozzle. Helium is used as the co-flow inert gas because its density closely matches that of the hot products and enables flatter flames than with nitrogen. The nozzle-to-plate separation distance is $L = 8\,\text{mm}$. Figure 5.1 (extracted from Bergthorson 2005a) shows the coflow nozzle apparatus with the water-cooled stagnation plate. PTV and PLIF are used to measure the velocity and CH relative concentration profiles (Crosley 1989) on the jet axis, respectively.

PTV keeps the low particle-loading advantage of the particle-streak velocimetry (PSV) technique used in previous work (Bergthorson et al. 2005a), while featuring a 16-times-larger spatio-temporal resolution than PSV (thus no dilution is needed in the flames involving large velocities), with a reduced scatter in the measurements compared with PSV (see Table D.5). The PTV illumination

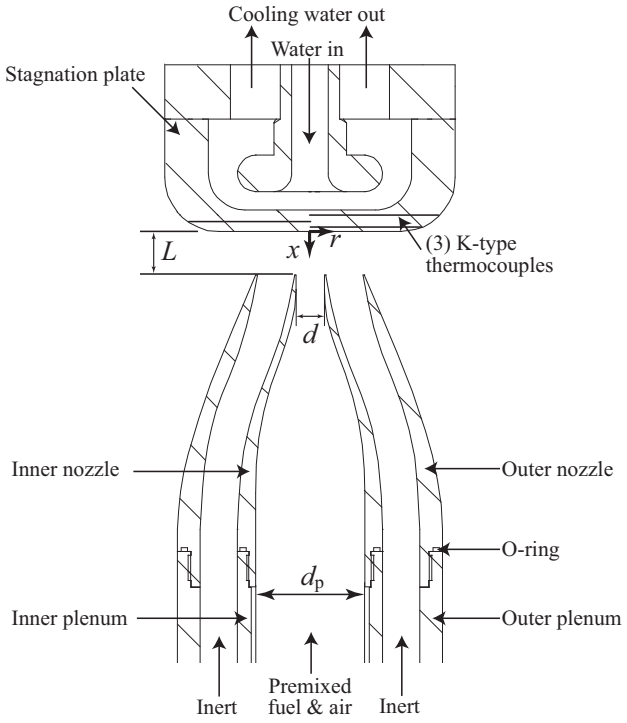

Figure 5.1: Coflow nozzle apparatus with water-cooled stagnation plate. (courtesy of Bergthorson 2005a)

source is a pulsed Coherent Nd:YLF 527 nm laser with repetition rates, ν_p, from 1 to 20 kHz. Images are recorded using a digital-imaging system (PCO.4000) that relies on a low-noise (cooled), 4008×2672 pixels^2 CCD. Exposure times of 250 ms result in multiple dotted trajectories of particles that completely traverse the image during the exposure (see Fig. 5.2). Only dots of diameters 2–3 pixels are processed excluding larger dots that come from agglomerated particles (like the dots of the central trajectory in Fig. 5.2, chosen for display purposes). Sample PTV images in C_3 flames are shown in Section A.3. The resulting dot record is processed to determine the locations of each dot. The particle displacement multiplied by ν_p provides the velocity estimate, located at the average position of the particle over the period between pulses. The particles seeded in the flow are 1 μm diameter alumina particles ($\rho_p \cong 3830\,\mathrm{kg/m^3}$), and ν_p is 5 kHz for the leanest & richest flames, for both fuels under study, and 10 kHz for the other flames. The advantages of the new PTV technology are discussed further in Appendix A, and more details about the key element in this technique — the laser — are available in Appendix F.

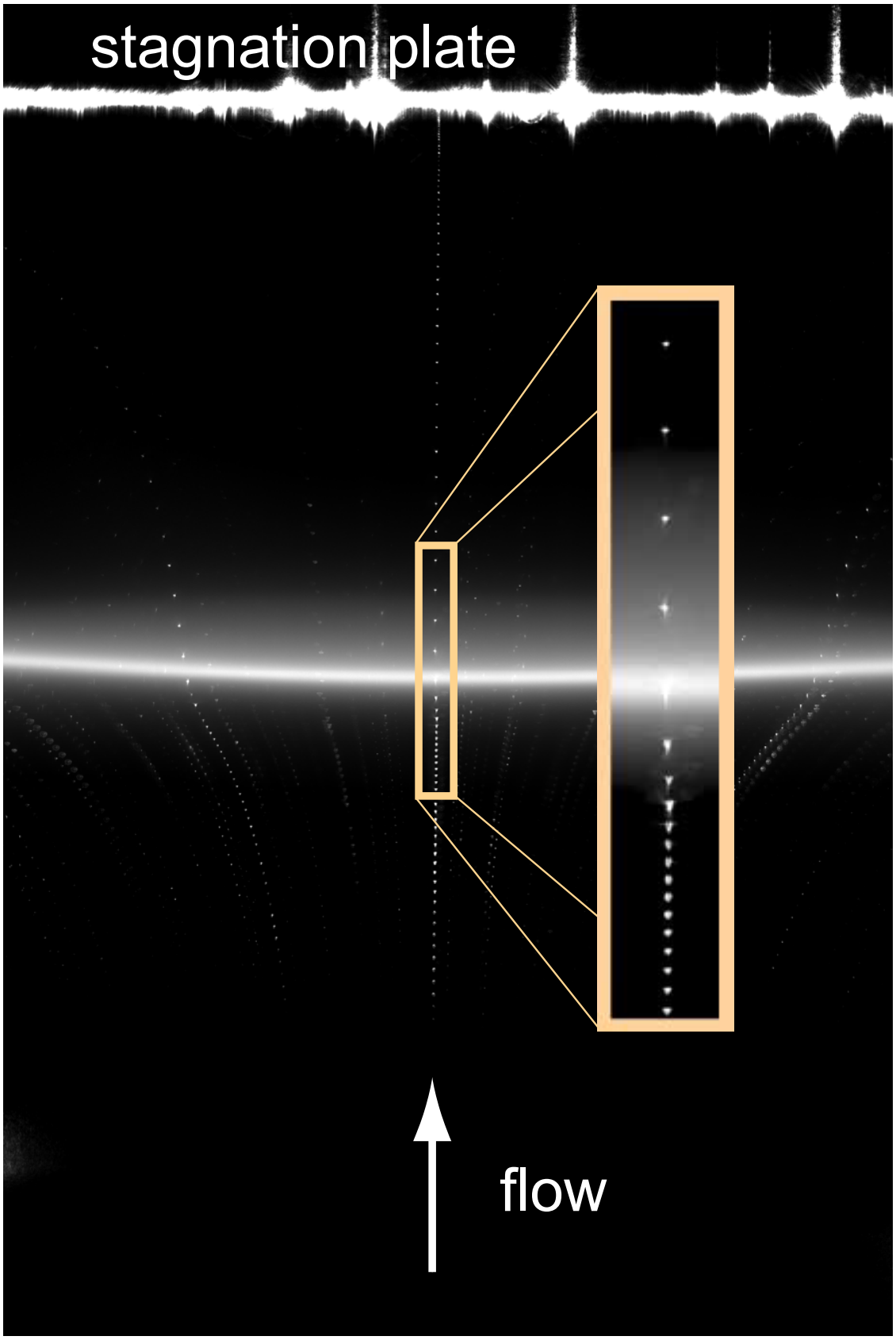

Figure 5.2: PTV image in a Φ=1.0 C_3H_8-air flame (ν_p=10 kHz).

The CH-PLIF technique relies on the excitation to the B state by a Sirah tunable dye laser and measures the two-dimensional CH fluorescence from the A-X transition (Carter et al. 1998, Sutton & Driscoll 2003) in the saturated fluorescence regime, using a lens-coupled intensifier with a cooled CCD binned to $344\times260\,\text{pixels}^2$, illuminated only during a 200 ns gate to reject chemiluminescence while retaining fluorescence (Bergthorson et al. 2005a, Bergthorson & Dimotakis 2007). The broadband fluorescence signal from polycyclic aromatic hydrocarbons interfering with the CH fluorescence (Norton & Smyth 1991) is suppressed by measuring the fluorescence signal both on & off of the resonance line, and taking the difference of the two (Sutton & Driscoll 2003). Composite (single and averaged images) CH-PLIF images in C_3 flames are shown in Appendix B. The simultaneous use of PTV with CH PLIF was enabled by the use of optical filters. Specifically, a FF01-510/84 Semrock green bandpass filter is used in front of the PTV camera to reject the UV-laser light (390 nm) that excites the CH radicals, the fluorescence of the CH radicals (430 nm), and some of the light coming from the C_2 Swan bands, thus enabling a better resolution of the velocity profile within the flame. In front of the CH-PLIF camera, a Schott KV-418 longpass filter is used to reject the UV-laser light (390 nm), and a NF01-532U Semrock notch filter is used to reject the green light (527 nm) used by the PTV laser, while not decreasing the CH-fluorescence signal.

The fuel flow rate is set and measured using a flow controller (Omega FMA) and the air flow rate is set using a sonic metering valve and measured concurrently by a flow meter (Omega FMA). Both the flow controller and the flow meter are calibrated using a Bios DryCal ML-500 dry-piston calibrator. The estimated volumetric flow rate uncertainty for each stream is 0.6 %, which results in a total uncertainty in Φ of 0.8 % (not including the C_3H_8 and C_3H_6 purities $\geqslant 99.5\,\%$). Simultaneous measurements of fuel and air volumetric fluxes, as well as of inlet-gas temperature and stagnation-plate temperature, provide accurate boundary conditions for simulations. Further details on the experimental apparatus and the CH-PLIF methodology are available (Bergthorson 2005a, Appendix C).

5.3 Results and discussion

Figures 5.3 and 5.4 show a comparison of experimental PTV axial-velocity, u, and CH-PLIF profiles with numerical predictions, using S5 in C_3H_8- & C_3H_6-air flames (under very lean, stoichiometric, & very rich conditions), and using DLW in a stoichiometric C_3H_8-air flame, respectively. The high PTV-laser repetition rate, ν_p, results in the simulated particle velocity profile and the modeled-PT velocity profile being almost identical. Therefore, only the simulated fluid and modeled-PT velocity profiles are included for clarity. In Figs. 5.3 and 5.4, the central column (jet axis) CH-PLIF profiles, averaged over 1000 images, are plotted. The experimental CH-peak location, $x_{\text{CH,exp}}$, is determined from this profile by a cubic fit to its peak portion. The CH-PLIF averaged profiles are not as

smooth in the leanest and richest flames (see Figs. 5.3a, 5.3e, 5.3f, and 5.3j) because the smaller CH concentrations in these flames result in reduced signal-to-noise ratios in single images. CH-profile asymmetry is noticeable in the richest C_3H_8 and C_3H_6 flames (see Figs. 5.3e and 5.3j), as observed previously (Bergthorson & Dimotakis 2007). With the current experimental setup, stable C_3H_8- and C_3H_6-air flames were established for equivalence ratios in the range $0.7 \lesssim \Phi \lesssim 1.5$ and $0.7 \lesssim \Phi \lesssim 1.6$, respectively. Figure 5.3 shows that S5 predictions are very close to experiment in C_3H_8 flames, while both velocities and CH-peak position are underpredicted in very lean & stoichiometric C_3H_6 flames and overpredicted in the very rich C_3H_6 flame. For certain conditions (given fuel and stoichiometry) where the chemistry seems adequately modeled by a given mechanism, the modeled-PT profile accurately captures the shape of the experimental velocity profile (see Fig. 5.4). Particle-inertia and thermophoretic effects are discernible only within the flame and in the vicinity of the wall, and accounting for them enables good agreement even in these high-gradient regions that cause slight deviations of the particle velocity profiles from the gas velocities. Including finite particle-track interval effects is more important when lower-resolution velocimetry systems are used (Bergthorson & Dimotakis 2006).

Experimental velocity (see Fig. 5.5a) and relative-CH-concentration (see Fig. 5.5b) profiles are compared with the predictions from five different mechanisms in order to assess their relative performance, in a very lean ($\Phi = 0.7$) C_3H_8-air flame. For this flame, DLW underpredicts velocities and CH-profile location, BL & G3 overpredict velocities and CH-profile location, and S5 & KON yield predictions closest to experiment. From the detailed information contained in the velocity and relative-CH-concentration profiles, two specific scalar validation targets can be extracted for use by kineticists that capture a significant portion of the combustion chemistry: the strained stagnation flame speed, S_u, where S_u is taken as the velocity-profile minimum upstream of the flame, and the CH-peak location, x_CH. These two scalars, S_u and x_CH, can be used to assess the adequacy of kinetic mechanisms.

The relative difference, $\widetilde{dS}_\mathrm{u}$, between the predicted stagnation flame speed, $S_\mathrm{u,sim}$ (determined from the interpolated simulated profile) and the measured stagnation flame speed, $S_\mathrm{u,exp}$ (determined from a cubic fit around the minimum of the experimental profile), is shown in Fig. 5.6. Figure 5.6 also shows the scaled difference, $\widetilde{dx}_\mathrm{CH}$, between the predicted CH-profile peak location, $x_\mathrm{CH,sim}$, and the measured CH-profile peak location, $x_\mathrm{CH,exp}$, scaled by the stoichiometric CH-layer thickness simulated with S5, i.e., $\delta_{\mathrm{CH,S5},\Phi=1}$ (Bergthorson 2005a). δ_CH is determined by taking the full width at half maximum of the interpolated CH profile. Positive values of $(x_\mathrm{CH,sim} - x_\mathrm{CH,exp})/\delta_{\mathrm{CH,S5},\Phi=1}$ indicate that the simulated CH profile is upstream of the (measured) PLIF profile. A gray-filled band represents the experimental uncertainties, Σ_exp, on $\widetilde{dS}_\mathrm{u}$ and $\widetilde{dx}_\mathrm{CH}$ in Fig. 5.6 (see Appendix E, and more specifically Eqs. E.6–E.12), obtained by taking into account both the uncertainties on $x_\mathrm{CH,exp}$ ($S_\mathrm{u,exp}$) and $x_\mathrm{CH,sim}$ ($S_\mathrm{u,sim}$). The uncertainties on $x_\mathrm{CH,sim}$ and $S_\mathrm{u,sim}$ were obtained by propagat-

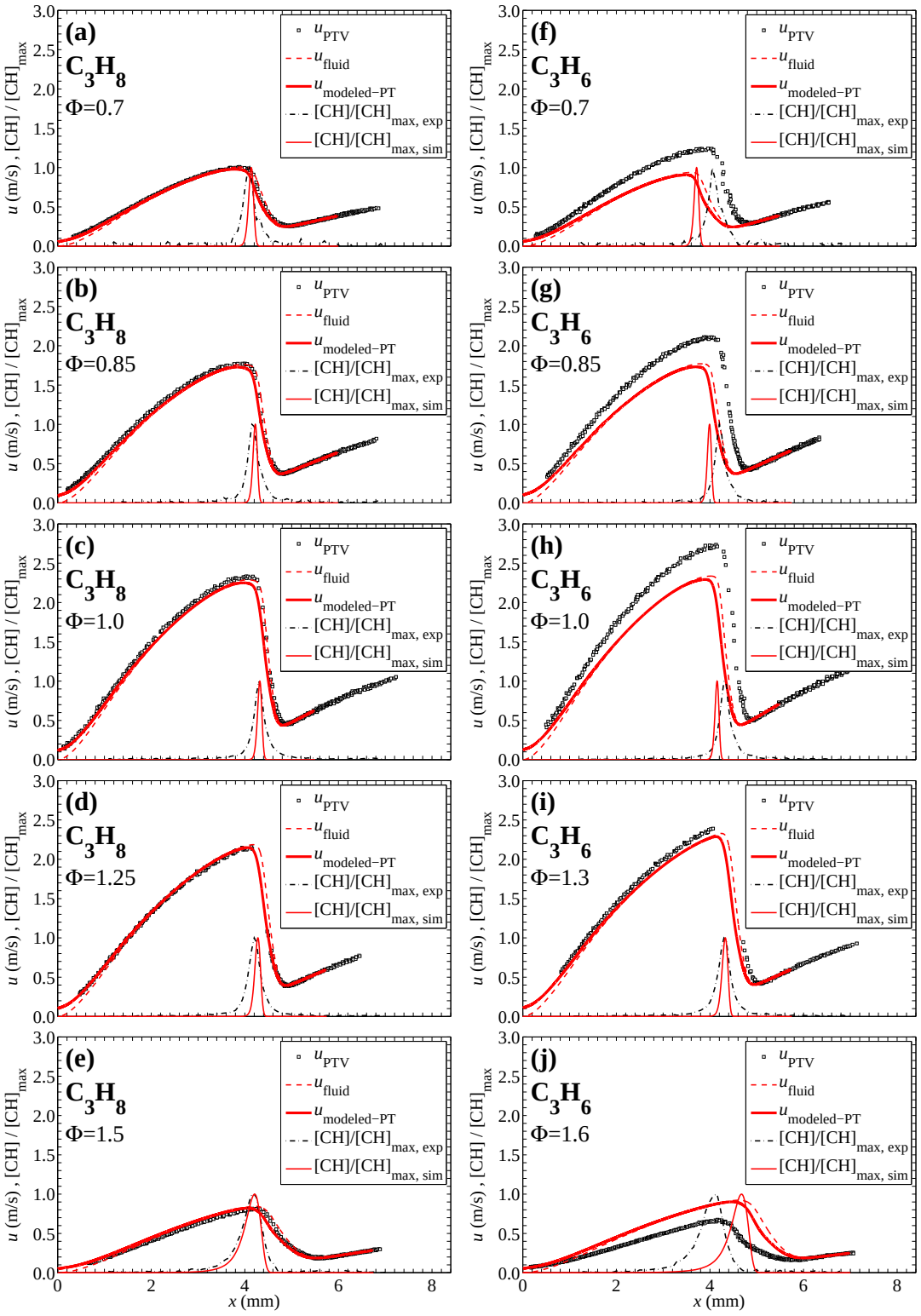

Figure 5.3: C_3H_8-air (left) and C_3H_6-air (right) flame profiles simulated with the S5 mechanism.

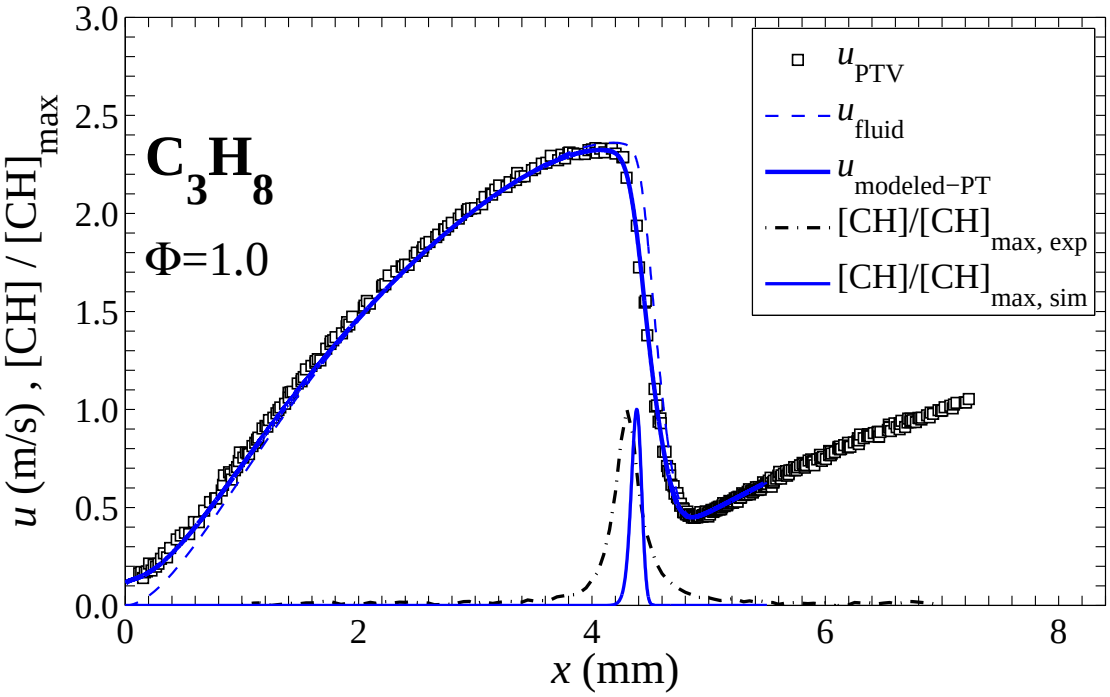

Figure 5.4: $\Phi = 1.0$ C_3H_8-air flame profiles simulated with the DLW mechanism.

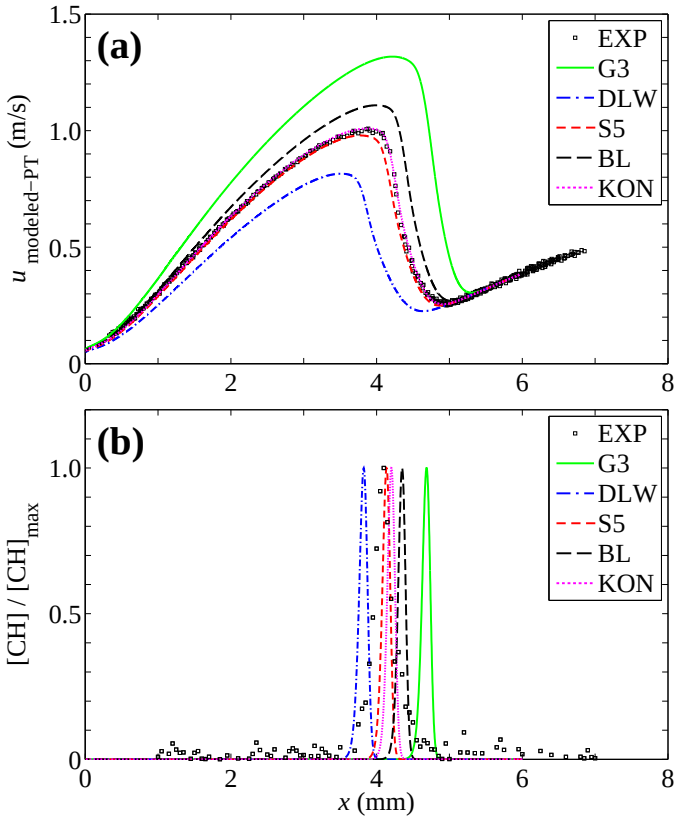

Figure 5.5: Comparison of predicted velocity (a) and relative-CH-radical concentration (b) with experiment, for different kinetic mechanisms, in a $\Phi = 0.7$ C_3H_8-air flame.

ing the experimental uncertainties on the measurements of the simulation input parameters (pressure: $\sim 0.2\,\%$, equivalence ratio: $\sim 0.8\,\%$, percentage of oxygen in air: $\sim 0.2\,\%$, inlet velocity: $\sim 0.6\,\%$, inlet velocity gradient: $\lesssim 4.7\,\%$, inlet temperature: $\sim 0.3\,\%$, and wall temperature: $\sim 0.8\,\%$) weighted by the sensitivity of $x_{\mathrm{CH,sim}}$ and $S_{\mathrm{u,sim}}$ to each of them. Σ_{exp} depends weakly on the mechanism used; Σ_{exp} displayed in Fig. 5.6 is the largest value of Σ_{exp} evaluated using DLW, S5, BL, and KON. Uncertainties associated with the models are not estimated here, but will be addressed in future work. No correction to $S_{\mathrm{u,exp}}$ and $x_{\mathrm{CH,exp}}$, such as the first-order correction suggested by Markstein (1951), using curvature Markstein lengths (Bradley et al. 1996), is attempted to account for the effect of the small curvature of the experimental flames (Sone 2007). Two-dimensional discernible effects may slightly alter the conclusions, such as in a $\Phi = 1.2$ CH_4-air flame, where Sone (2007) showed that the stagnation-flame speed predicted by the two-dimensional simulation using G3 was $\sim 9\,\%$ lower than experiment whereas the stagnation-flame speed predicted by the one-dimensional simulation using G3 was almost identical to the experimental value. The curvatures were obtained from parabolic fits to the central portion (around the jet axis) of the two-dimensional CH-PLIF data (concave towards the stagnation plate for all flames studied) and are listed in Table D.4.

Figure 5.6 shows that except for the very rich C_3H_6 flame, where S_{u} and x_{CH} are largely overpredicted by all mechanisms compared, BL and KON performances are similar in C_3H_8 and C_3H_6 flames. On the other hand, DLW and S5 predictions exhibit a larger variance from experiment in C_3H_6 flames. Such increased variance from a fuel with single bonds connecting the carbon atoms to a fuel with double C=C bonds was noticed in earlier work (Bergthorson & Dimotakis 2007), where DLW and the 2005/03 release of the San Diego mechanism yielded predictions further from experimental data in C_2H_4 flames than in C_2H_6 flames, especially under very lean and very rich conditions. S5 and BL are found to be the best mechanisms to simulate the C_3H_8 and C_3H_6 flames investigated, respectively. When considering the C_3H_8 and C_3H_6 flames investigated (each fuel is given the same weight), S5 was found to have the best overall performance over the range of stoichiometries studied.

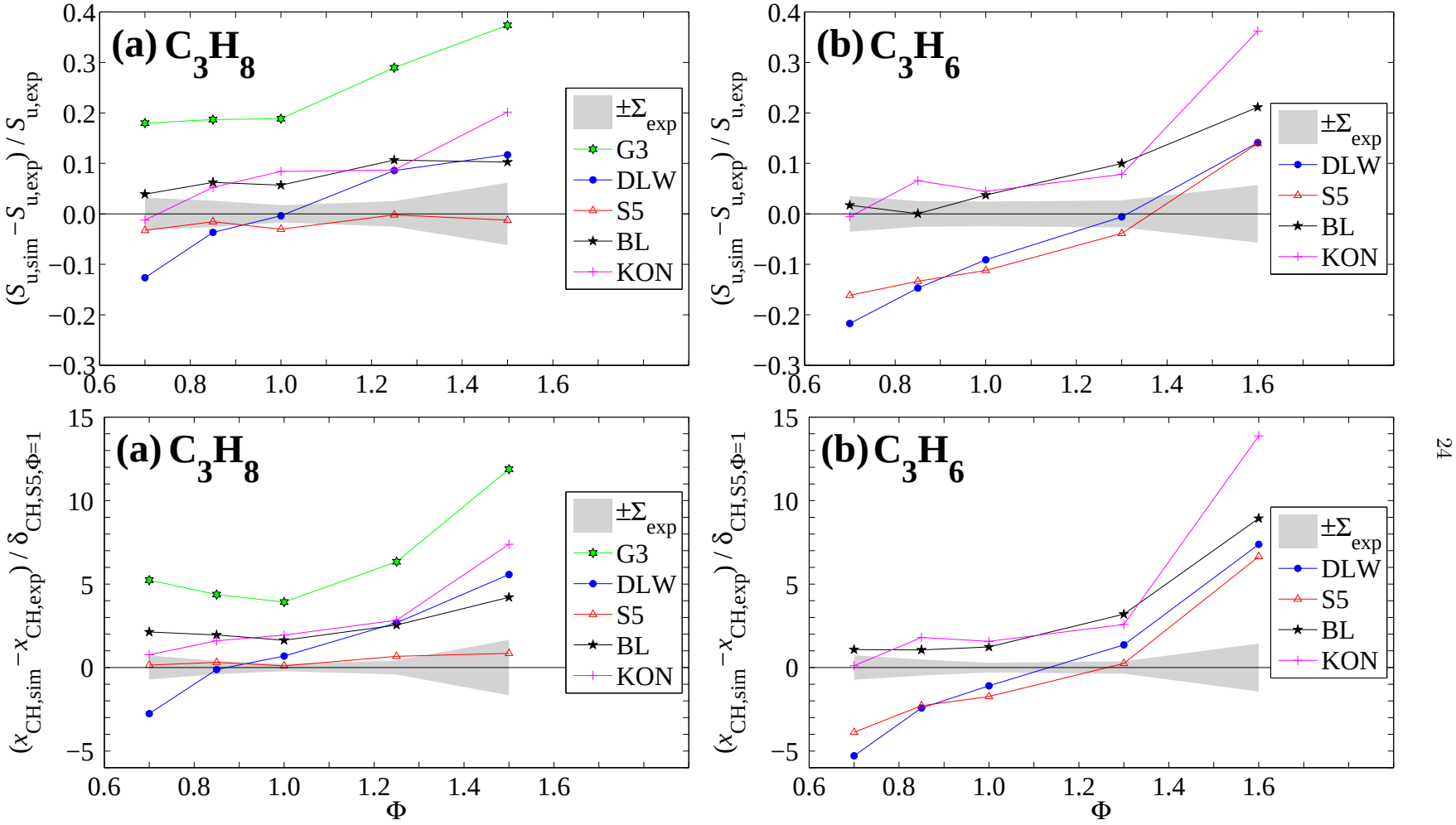

Figure 5.6: Difference between simulated and measured stagnation-flame speeds (top) and CH-peak locations (bottom) for: (a) C_3H_8-air and (b) C_3H_6-air flames. (C_3H_6 is not present in G3.)

S5 predictions are very close to experiment for C_3H_8 flames, even in the very rich C_3H_8 flame where S_u and x_{CH} are overpredicted by all other mechanisms tested. As for the C_3H_6 flames, close agreement between simulation with S5 and experiment is also reached at Φ=1.3, but S5 underpredicts both S_u & x_{CH} in very lean to stoichiometric flames and overpredicts both of them in the very rich flame. Experimental data are well captured by DLW in moderately-lean and stoichiometric C_3H_8 flames, consistent with Davis et al. (1999). In very lean C_3H_8 & C_3H_6 flames, S_u & x_{CH} are underpredicted by DLW, despite the good agreement of simulated and experimental laminar flame speeds shown in Davis et al. (1999), and DLW predictions are lower than those of the other mechanisms. S_u and x_{CH} are also underpredicted by DLW in lean and stoichiometric C_3H_6 flames. The flame speed underpredictions by DLW in very lean to stoichiometric C_3H_6 flames found in the present work are in contrast with the overprediction of laminar flame speeds shown in Jomaas et al. (2005) and the good agreement shown in Davis et al. (1999). Unlike the slight underprediction of rich C_3H_8 laminar flame speeds (Vagelopoulos et al. 1994) and the clear underprediction of rich C_3H_6 laminar flame speeds, both shown in Davis et al. (1999), flame speeds are overpredicted by DLW in rich C_3H_8 and very rich C_3H_6 flames in the present work, consistent with the rich C_3H_6 laminar flame speed clear overpredictions in Jomaas et al. (2005). BL slightly overpredicts S_u & x_{CH} in lean to stoichiometric C_3H_8 flames, and overpredicts them more in rich C_3H_8 & C_3H_6 flames. Nevertheless, BL predicts well very lean to stoichiometric C_3H_6 flame experimental data. KON predicts very well the leanest C_3H_8 & C_3H_6 flame experimental data, but overpredicts S_u & x_{CH} in all other flames, with an increasing disagreement between simulation and experiment as the flame becomes increasingly rich. Previous comparisons of BL and KON predictions with C_3 flame-speed data were not found in the literature.

In order to identify the most-important reactions for the flames investigated, the logarithmic sensitivities of simulated flame positions (defined as the CH-peak locations, x_{CH}) to changes in the reaction rate values are computed for six representative flames covering the two fuels under study, and the very lean, stoichiometric, and very rich burning regimes, using the DLW mechanism (see Figs. 5.7a and 5.7b) because it yields similar results to S5 and has more reactions. The mixture-averaged transport model, which yields results that are close to the full multi-component model, is used in the sensitivity analyses to save computing time. To determine the sensitivity of x_{CH} to variations in kinetic rates, the "brute-force" method is utilized as suggested by Frenklach (1984). Simulations are performed varying a single kinetic rate at a time, and x_{CH} is compared to its original predicted value to determine the effect of each reaction rate. The logarithmic sensitivity for the CH-peak location to each reaction rate, k_j, can be calculated using: $LS(x_{CH})_j = \mathrm{dlog}x_{CH}/\mathrm{dlog}k_j = \Delta x_{CH}/x_{CH} \cdot k_j/\Delta k_j = (x_{CH}(k_j+\Delta k_j) - x_{CH}(k_j))/x_{CH}(k_j) \cdot k_j/\Delta k_j$. The reactions displayed on Figs. 5.7a and 5.7b were selected by keeping only the reactions with a logarithmic sensitivity (in absolute value) larger than 5 % in at least one of the flames investigated. Figures 5.7a and 5.7b show that flame position is sensitive

only to a small number of reactions for the two fuels studied, among which a few reactions involving C_3H_6 and the allyl radical (aC_3H_5). The sensitivity variations to equivalence ratio changes are also very similar between the C_3H_8 and C_3H_6 flames investigated.

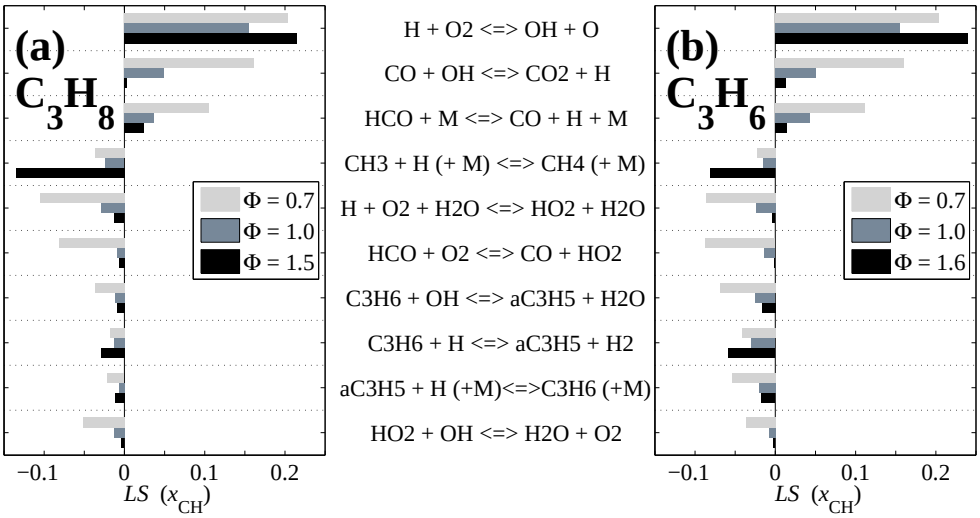

Figure 5.7: Logarithmic sensitivity of the CH-peak locations computed with DLW in: (a) C_3H_8-air and (b) C_3H_6-air flames.

A simple comparison of individual reaction rates between mechanisms may reveal a possible source of the variance between predictions from different mechanisms. The same reaction rate is used for $C_3H_6 + H \rightleftharpoons aC_3H_5 + H_2$ in DLW, S5, and BL, but a lower reaction rate is used in KON. In the very rich C_3H_6 flame investigated, C_3H_6 & H or aC_3H_5 & H_2 are simultaneously present at temperatures between 950 and 1740 K, where the KON reaction rate is 2 to 6 times smaller than the rate in DLW, S5, and BL. Since $C_3H_6 + H \rightleftharpoons aC_3H_5 + H_2$ has a negative effect on flame position (and on flame speed), the large overprediction of S_u and x_{CH} by KON in the very rich C_3H_6 flame (see Fig. 5.6b) may be partly attributable to this reaction-rate difference. A sensitivity analysis was also performed using S5 in order to try to explain the large variance from experiment in C_3H_6 flames (see Fig. 5.6b). Although the cause of the lower predictions of S_u and x_{CH} by S5 in very lean to stoichiometric C_3H_6 flames remains unclear, a peculiar feature was noted that may be related to the overprediction of S_u and x_{CH} by S5 in very rich C_3H_6 flames. The logarithmic sensitivity of flame position to an increase in the S5 reaction rate of $CH_3 + H (+ M) \rightleftharpoons CH_4 (+ M)$ is negative in all the C_3H_8 flames investigated, consistent with sensitivity analysis (see Figs. 6.4–6.6) using S5 in CH_4, C_2H_6, and C_2H_4 flames studied in Bergthorson & Dimotakis (2007). However, the same logarithmic sensitivity in the very rich C_3H_6 flame is positive: $\sim +10\%$, compared to $\sim -15\%$ in the very rich C_3H_8 flame. The same peculiar feature can be noted with $C_3H_6 + H \rightleftharpoons aC_3H_5 + H_2$, with a logarithmic sensitivity $\sim -5\%$ in very rich C_3H_8 flames and $\sim +7\%$ in very rich C_3H_6 flames.

Chapter 6

Validation of chemical-kinetic models against CH_4-, C_2H_6-, and C_2H_4-air stagnation-flame experiments and comparative sensitivity analysis

6.1 Validation of C_1–C_3 kinetic mechanisms against CH_4-, C_2H_6-, and C_2H_4-air stagnation-flame experiments at variable stoichiometry

6.1.1 Flame position: a good surrogate for flame speed in stagnation-flow-stabilized flames

The present study builds upon the work of Bergthorson & Dimotakis (2007), where detailed axial-velocity and CH-radical profile measurements in laminar premixed flames stabilized in a jet-wall stagnation flow are compared with flame simulations in order to validate and compare chemical-kinetic mechanisms. The simulations rely on the one-dimensional hydrodynamic model from Kee et al. (1989, 2003), a multi-component transport formulation including thermal diffusion, & several detailed chemical-kinetic mechanisms, and are performed with CANTERA (Goodwin 2003). More details about the numerical method were presented in Chapter 4. The experimental velocities measured using particle-streak velocimetry (PSV) (Bergthorson et al. 2005a) are compared with the simulated velocities, which are corrected to account for the effects of inertia & thermophoresis on the particle motion and to account for the finite temporal resolution of the velocimetry technique (Bergthorson & Dimotakis 2006). In addition, the experimental CH-radical profiles measured using planar laser-

induced fluorescence (PLIF) can be directly compared to the simulated CH profiles. Figure 6.1 shows the experimental PSV and simulated axial-velocity, u, profiles, as well as the experimental PLIF and simulated relative-CH-radical concentrations, in a CH_4-air flame of equivalence ratio $\Phi = 0.7$ (only four representative mechanisms are plotted for clarity). Kinetic mechanisms performance can be assessed from such comparisons: for this lean CH_4-air flame, DLW clearly appears to be the only mechanism that does not overpredict both velocities and CH-profile location.

CH is a short-lived radical with a narrow spatial profile confined to the reaction zone (Crosley 1989). Thus, the CH-peak location, x_{CH}, yields a sharp estimate of flame location that is predicted by the detailed flow-kinetic models and can be directly compared with experiment. Moreover, differences between measured and predicted CH-peak location correlate well with differences between measured and predicted strained stagnation-flame speed, S_{u} (Bergthorson & Dimotakis 2008), where S_{u} is defined as the value of the velocity-profile minimum upstream of the flame. The information contained in the axial velocity and CH-radical profiles can therefore be reduced to a single scalar: the CH-peak location, x_{CH}.

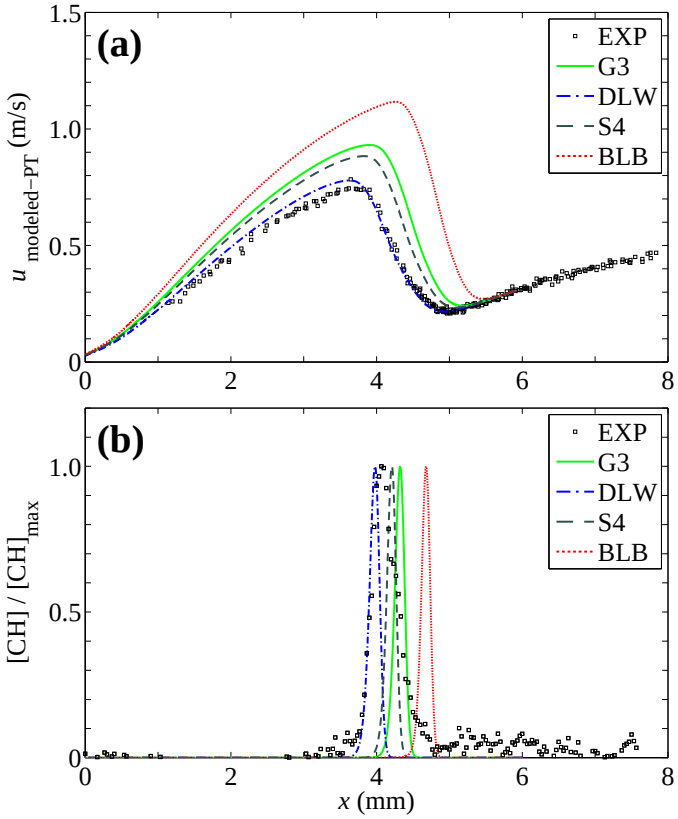

Figure 6.1: Comparison of predicted velocity (a) and relative-CH-radical concentration (b) with experiment for different kinetic mechanisms, in a $\Phi = 0.7$ CH_4-air flame.

6.1.2 Comparison of predicted flame positions with experiment

The experiments in CH_4-, C_2H_6-, and C_2H_4-air flames cited in the present study are the experiments discussed in Bergthorson & Dimotakis (2007). There was no dilution in the CH_4- and C_2H_6-air flame experiments, where the percentage of oxygen (O_2) in the "air" (composed of O_2 and nitrogen, N_2) is given by $21\,\%O_2/(O_2{+}N_2)$ at all values of Φ. In order to reduce the flame speeds for near-stoichiometric conditions, N_2 dilution was employed for the C_2H_4-air flames. The resulting compositions were: $\Phi = 0.6$, $21\,\%O_2/(O_2{+}N_2)$; $\Phi = 0.8$, $19.5\,\%O_2/(O_2{+}N_2)$; $\Phi = 1.0$, $17\,\%O_2/(O_2{+}N_2)$; $\Phi = 1.2$, $16.5\,\%O_2/(O_2{+}N_2)$; $\Phi = 1.4$, $18\,\%O_2/(O_2{+}\,N_2)$; $\Phi{=}1.6$, $21\,\%O_2/(O_2{+}N_2)$; and $\Phi = 1.8$, $21\,\%O_2/(O_2{+}N_2)$. The compositions of all of these flames are summarized in Table D.1. The multicomponent flame simulations in the present study include thermal diffusion that is not included in Bergthorson & Dimotakis (2007). The thermal diffusion effect on flame location is quantified in Section C.2. Moreover, the kinetic mechanisms: G1, G2, ABF, WL, S3, S4, S5, MRN, DAG, BLB, and KON are used in the present study, in addition to those considered in Bergthorson & Dimotakis (2007). Simulations would only rarely converge with the less-robust mechanisms MRN, DAG, BLB, and KON. Therefore, a continuation technique between mechanisms was elaborated that enables converged solutions with these less-robust mechanisms. The continuation technique was presented in detail in Section 2.2. Between 300 and 500 gridpoints are needed for converged solutions (see Section C.1).

Figures 6.2a–c plot the difference between predicted and measured CH-peak locations, x_{CH}, scaled by the stoichiometric flame thickness simulated with S4, $\delta_{\mathrm{CH,S4},\Phi=1}$ (different for each fuel, estimated as the full width at half maximum of the CH profile), for CH_4-, C_2H_6-, and C_2H_4-air flames, respectively, at variable stoichiometry. Positive values of $(x_{\mathrm{CH,sim}} - x_{\mathrm{CH,exp}})/\delta_{\mathrm{CH,S4},\Phi=1}$ indicate that the simulated CH profile is upstream of the measured CH profile and that the predicted flame speed is higher than experiment ($x = 0$ at the wall). The uncertainty in the boundary-condition measurements corresponds to a total estimated uncertainty in the predicted flame location of $\sim 0.5\,\delta_{\mathrm{CH}}$ (Bergthorson 2005a, Section 2.6).

An error, Δ_m, is defined that quantifies the difference between the predictions from a given mechanism, m, and the experiment for a data set considering flames of different fuels and stoichiometries:

$$\Delta_m = \text{Average over the flame data set of } \left| \frac{x_{\mathrm{CH,sim\ with\ mechanism}\ m} - x_{\mathrm{CH,exp}}}{\delta_{\mathrm{CH,S4},\Phi=1}} \right| \quad . \tag{6.1}$$

The "best" mechanism is then defined as the mechanism for which:

$$\Delta_{\mathrm{best}} = \min_{m=1,\ldots,N_{\mathrm{mech}}} \{\Delta_m\} \quad , \tag{6.2}$$

where N_{mech} is the number of mechanisms considered.

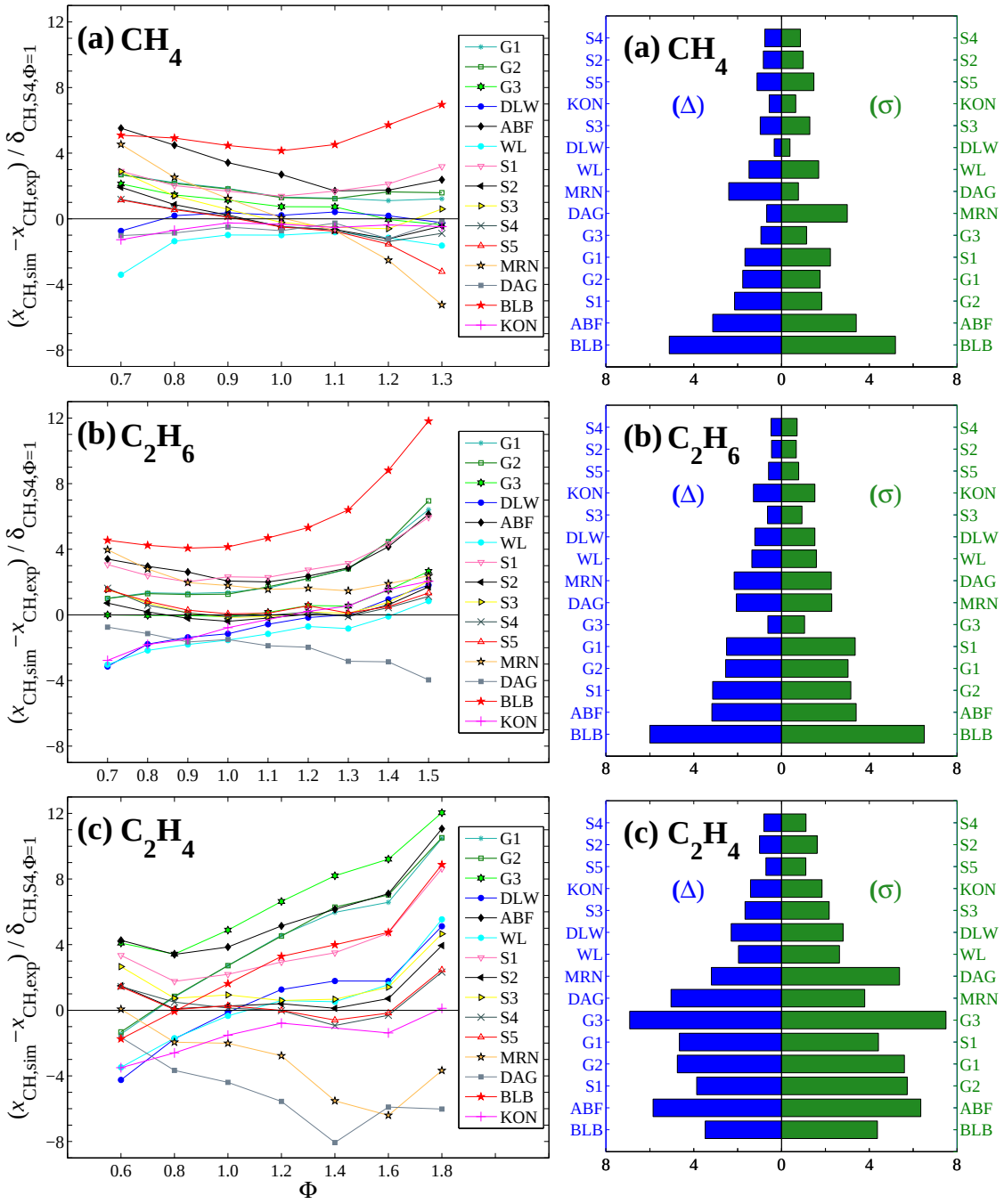

Figure 6.2: Difference between simulated and measured CH-peak locations (left), and comparison of the average performance (over the equivalence ratios investigated) of the different kinetic mechansims (right) for: (a) CH_4-, (b) C_2H_6-, and (c) C_2H_4-air flames.

Another error norm, σ_m, can be defined that can be minimized more naturally, that penalizes large variances:

$$\sigma_m{}^2 = (1/N_{\text{flames in data set}}) \cdot \sum_{\text{flame data set}} \left(\frac{x_{\text{CH,sim with mechanism } m} - x_{\text{CH,exp}}}{\delta_{\text{CH,S4,}\Phi=1}} \right)^2 \quad , \tag{6.3}$$

where $N_{\text{flames in data set}}$ is the number of flames in the data set considered. According to this second error norm, the "best" mechanism is defined as the mechanism for which:

$$\sigma_{\text{best}} = \min_{m=1,\ldots,N_{\text{mech}}} \{\sigma_m\} \quad . \tag{6.4}$$

Using either criterion, DLW (see Fig. 6.2a), S2 (see Fig. 6.2b), and S5 (see Fig. 6.2c) are found to be the "best" mechanism to simulate the CH_4, C_2H_6, and C_2H_4 flames investigated, respectively. This dependency on fuel of the "best" mechanism is not a good sign for the current state of combustion modeling, since the reactions set needed to model CH_4 combustion should be present in a model for C_2 oxidation, and conversely modeling rich CH_4 flames requires a robust set of reactions involving C_2 species (Kee et al. 2003, Section 14.3.1.2). When considering all of the CH_4, C_2H_6, and C_2H_4 flames investigated (each fuel is given the same weight), S4 has the "best" overall performance (see Fig. 6.3). Not surprisingly, G3 does poorly simulating C_2H_4 flames, for which it was not optimized and as found previously (Egolfopoulos & Dimotakis 2001).

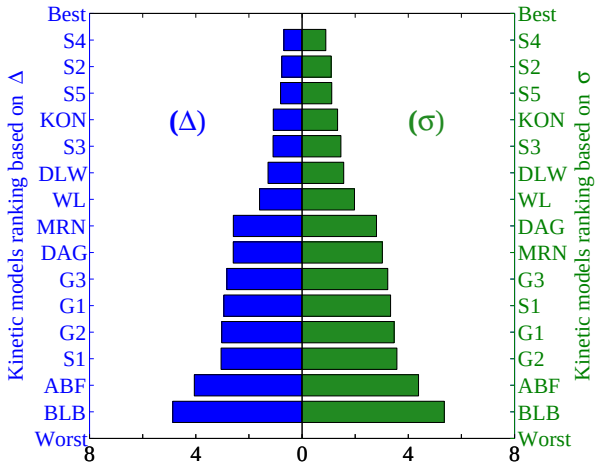

Figure 6.3: Ranking (based upon the criteria expressed in Eqs. 6.2 and 6.4) of the different kinetic mechanisms, in their ability to predict CH_4-, C_2H_6-, and C_2H_4-air flame positions, or flame speeds. (Each fuel is given the same weight.)

6.2 Comparison of reaction rates among the mechanisms

6.2.1 Comparative sensitivity analysis

The logarithmic sensitivities of the simulated flame positions (defined as the CH-peak locations) to changes in the reaction-rate values are computed for nine representative flames covering the three fuels under study, and the very lean, stoichiometric, and very rich burning regimes, using seven different representative mechanisms. G1 & G2, WL & ABF, and S1, S2, S3, & S4 are represented by G3, DLW, and S5, respectively, because their reactions & reaction rates are very similar, and therefore their sensitivities are expected to be very similar as well. To determine the sensitivity of the CH-peak location to variations in the kinetic rates, the "brute-force" method is utilized as suggested by Frenklach (1984). Simulations are performed varying a single kinetic rate at a time, and the CH-peak location is compared to its original predicted value to determine the effect of each reaction rate. The logarithmic sensitivity coefficient for the CH-peak location, x_{CH}, to each reaction rate, k_j, can be calculated using:

$$LS(x_{\mathrm{CH}})_j \;=\; \frac{\mathrm{d}\log \mathrm{x_{CH}}}{\mathrm{d}\log \mathrm{k_j}} \;=\; \frac{\Delta x_{\mathrm{CH}}}{x_{\mathrm{CH}}}\,\frac{k_j}{\Delta k_j} \;=\; \frac{x_{\mathrm{CH}}(k_j+\Delta k_j)-x_{\mathrm{CH}}(k_j)}{x_{\mathrm{CH}}(k_j)}\,\frac{k_j}{\Delta k_j} \quad . \tag{6.5}$$

The reaction rates were increased by a factor 1.5 ($\Delta k_j/k_j = 1/2$), which is sufficient to observe changes in the CH-peak location, while preventing large changes and corresponding increases in the computational time required for re-convergence. Reaction-rate increases by a factor smaller than 1.5 (some very close to 1 for DAG and KON) had to be used in order to get re-convergence for several reactions with MRN, DAG, BLB, and KON. This adds a difficulty to exploiting the information from the absolute sensitivities for DAG and KON. However this is not an issue as the present study does not exclusively focus on comparisons of logarithmic sensitivity values, rather sensitivity analysis indicates which reactions are key, and their reaction rates are compared among the different mechanisms. The mixture-averaged transport model is used to save computing time. For each flame, a fixed grid with 300 to 500 points is used in this study, although lower resolution simulations would have provided very similar sensitivity results. For highly sensitive results (such as the CH-peak location) in regions of high gradients, one would expect that the sensitivities could themselves be very sensitive to grid resolution. However, a study of the influence of resolution was performed with G3, which showed that the rms difference between the logarithmic sensitivity vectors at low resolution (~ 140 gridpoints) and at high resolution (~ 1000 gridpoints) is smaller than 0.4 % for all the flames studied. Figures 6.4–6.6 show comparisons of the logarithmic sensitivity of the CH-peak location to the most important reactions in the different mechanisms for each of the nine flames investigated. The average (over the different mechanisms) absolute value of the logarithmic sensitivity for each displayed reaction is large relative to the logarithmic sensitivity to other reactions (present in the

mechanism and not displayed here) in at least one of the flames investigated. As expected, Figs. 6.4–6.6 show that different mechanisms exhibit similar sensitivities to the same reactions and that flame position (or flame speed) is sensitive to a relatively small number of reactions only, for the three fuels studied.

6.2.2 Comparison of reaction rates

Given that there exists a broad consensus regarding the reaction set needed to model CH_4 combustion (there is greater disagreement for higher hydrocarbons), the challenge comes down to determining the ideal values for the various model parameters. Among these parameters, the variance in the chosen kinetic-rate constants is the largest source of disagreement between the different model predictions. Sensitivity analysis identifies reactions that have the largest effect on the flame, thus the corresponding kinetic rates can be compared between the different mechanisms in order to explain the discrepancies shown in Fig. 6.2. First, the positive ($LS_j > 0$) or negative ($LS_j < 0$) effect on flame position of an increase in the kinetic rate of each reaction j identified by the sensitivity analysis is determined for the flames investigated. The kinetic rates, k_j, are then compared between different mechanisms. The flame position is further assumed to depend only on the kinetic rate, k_j. This allows "a priori" comparisons of flame positions between different mechanisms. This assumption may often be invalid, because the flame position also depends on the relative importance of reaction j, which also varies from mechanism to mechanism. This approach focuses on individual reactions and is therefore not suited for the comparison of branching ratios that are representative of the relative importance of a subset of reaction rates. Also, sensitivity analysis would provide partial, and therefore biased, insight only, if key species and reactions were missing in the mechanism, which may happen when describing heavier hydrocarbons oxidation.

Despite these shortcomings, several reactions are shown to be the likely contributors to some of the clear differences between the predictions made by the various mechanisms studied (see Fig. 6.2). The overall variances in the model predictions can be summarized as:

- DLW & WL predict lower flame-position values in lean flames (see Reactions 1, 2, 3, 4, and 5).
- Despite its similarities with DLW, WL yields lower predictions than DLW in lean CH_4 flames (see Reaction 8), in rich C_2H_6 flames, and in moderately rich C_2H_4 flames (see Reactions 9 and 11). The better performance of WL in C_2H_4 flames is expected since WL has been developed to model C_2H_4 and C_2H_2 flames.
- ABF consistently overpredicts flame positions (see Reaction 10).
- S1 consistently overpredicts flame positions (see Reactions 8 and 10).
- S4 and S5 yield lower predictions than earlier releases of the SD mechanism (see Reactions 1, 3, 6, 7, and 9).
- MRN is the only mechanism that largely underpredicts rich CH_4 flame positions (see Reac-

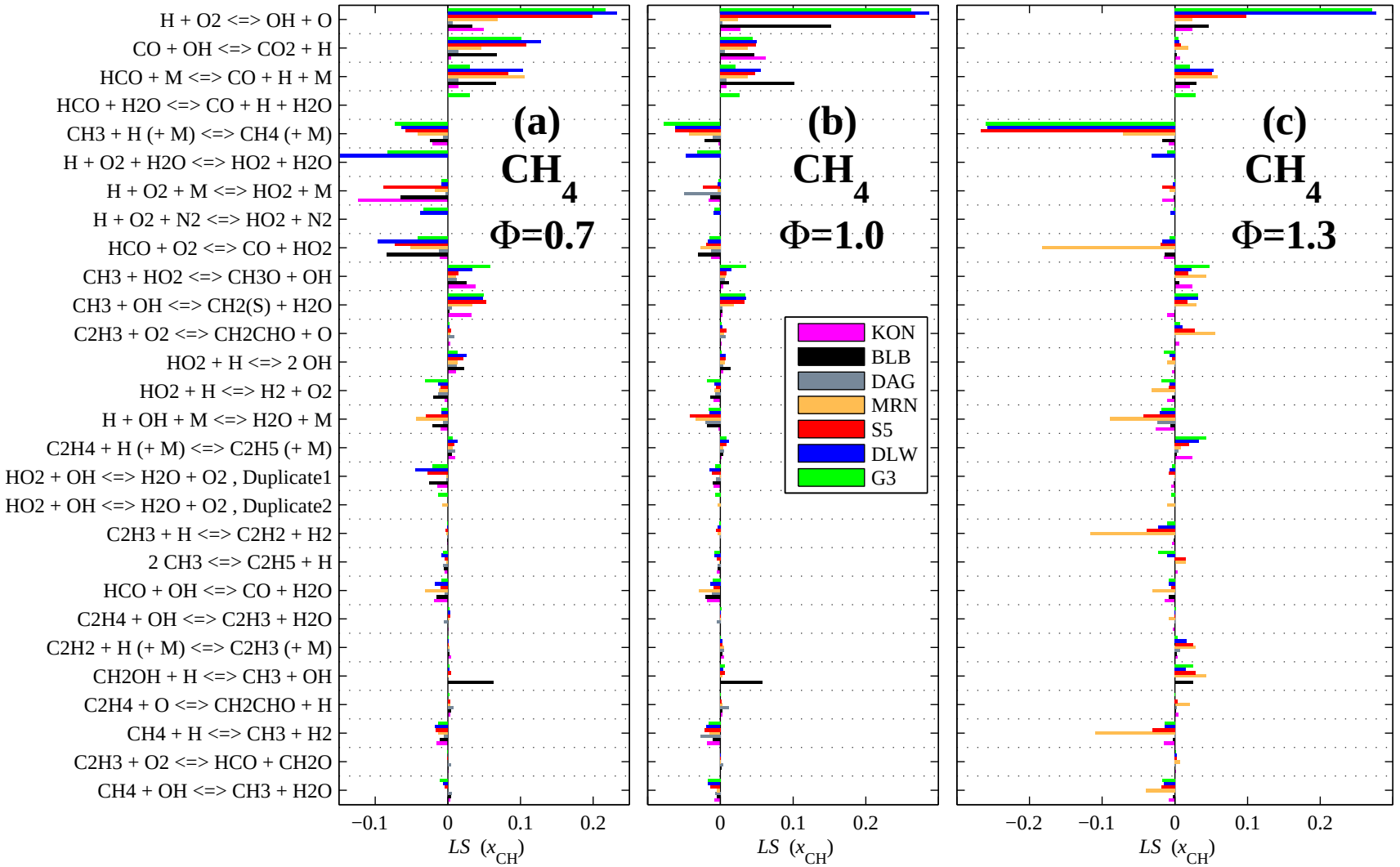

Figure 6.4: Logarithmic sensitivity of the CH_4-air flame CH-peak position with: (a) $\Phi = 0.7$, (b) $\Phi = 1.0$, and (c) $\Phi = 1.3$.

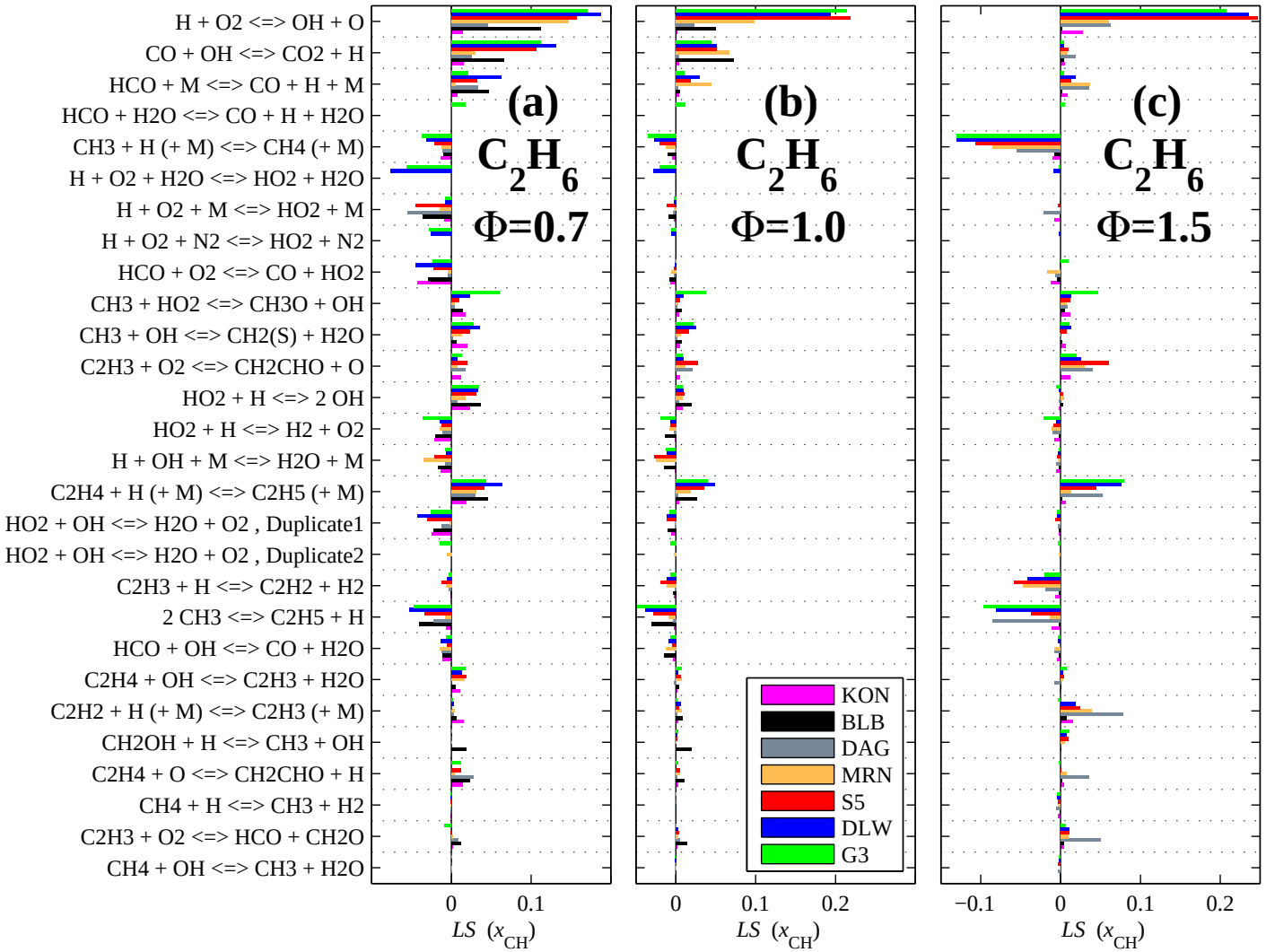

Figure 6.5: Logarithmic sensitivity of the C_2H_6-air flame CH-peak position with: (a) $\Phi = 0.7$, (b) $\Phi = 1.0$, and (c) $\Phi = 1.5$.

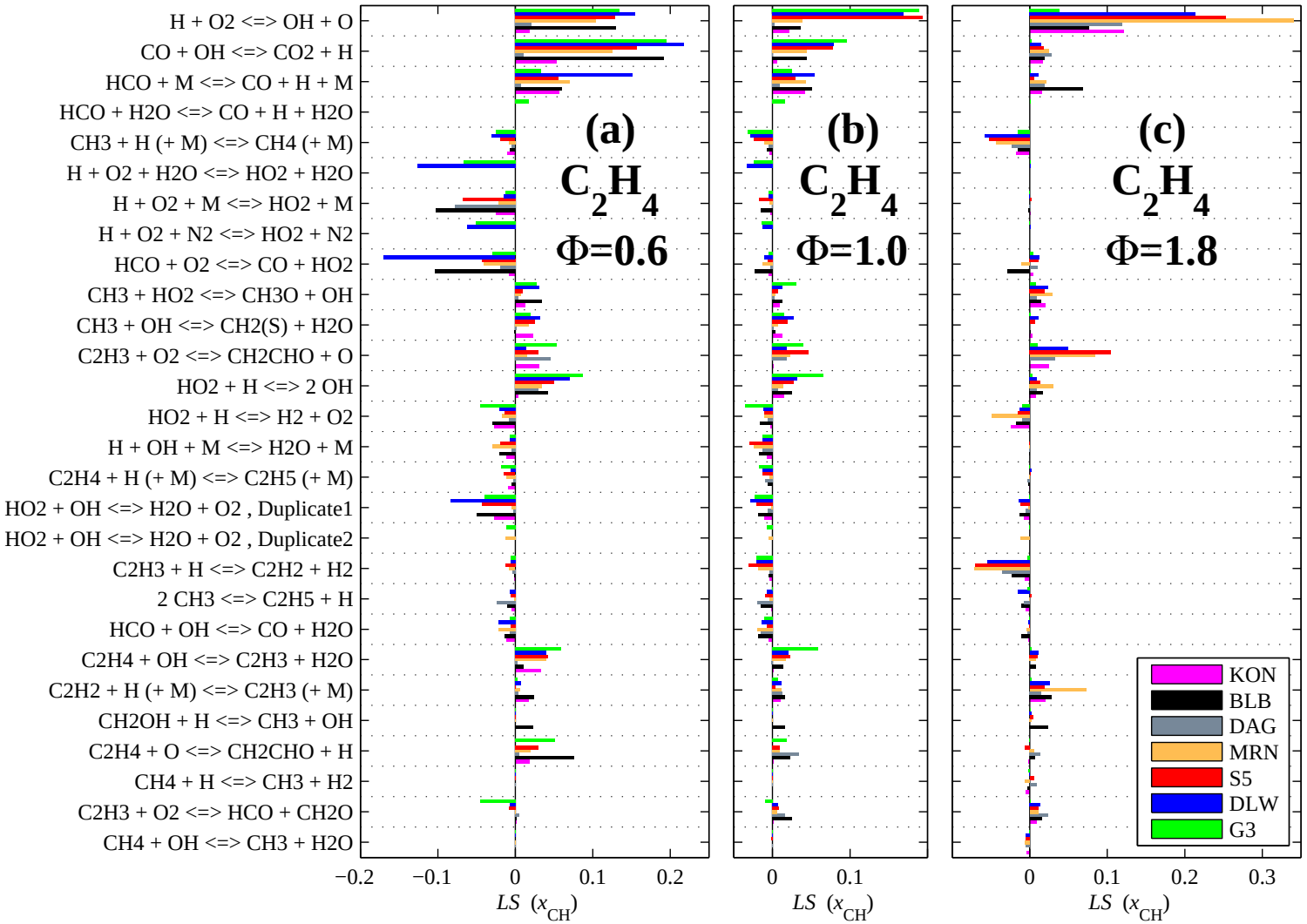

Figure 6.6: Logarithmic sensitivity of the C_2H_4-air flame CH-peak position with: (a) $\Phi = 0.6$, (b) $\Phi = 1.0$, and (c) $\Phi = 1.8$.

tions 3, 7, and 11). It also underpredicts all but the leanest C_2H_4 flame positions (see Reaction 11). Finally, it overpredicts lean CH_4 and all C_2H_6 flame positions.

- BLB consistently overpredicts flame positions (see Reactions 1, 9, and 12), except in lean C_2H_4 flames (see Reactions 2 and 3).
- DAG consistently underpredicts flame positions (see Reaction 13).
- KON consistently underpredicts flame positions by a small amount, except in rich C_2H_6 flames. It yields similar predictions as DLW and WL in C_2H_6 flames and it is the only mechanism to yield a correct prediction for the richest C_2H_4 flame.

Figures 6.7–6.16 show the temperature dependence between 300 K and 3000 K, of the reaction rates k_j (with concentration units mol/cm^3), at atmospheric pressure, for the reactions discussed later on. Some of the reactions that are discussed in this study involve a third collision partner: either a particular species, or an "inert", "bath-gas", or "third-body" species denoted by M. Curly brackets are used around the third partner in the reaction names when this reaction is modeled by a three-body reaction rate in some mechanisms (Arrhenius-type model, independent of pressure) and by a fall-off reaction rate in other mechanisms (dependent on temperature, but also on pressure). Traditionally, no brackets are used in the name of the reaction for a three-body reaction rate model, and simple brackets are used for a fall-off reaction rate model. For some of these reactions, a fall-off reaction rate model is used, whose value does not only depend on temperature, but also on the total molar concentration $[M]$. As explained in Gardiner-Jr. & Troe (1984), in the simplest view, M would represent collectively all the atoms and molecules of the reacting gas. From the ideal gas law, the bath-gas concentration $[M]$ in this view is then given by

$$[M] = P/RT \quad . \tag{6.6}$$

Eq. 6.6 was used to determine the fall-off reaction rate values in Fig. 6.7, Fig. 6.8, and Fig. 6.12, with $P = 1\,\mathrm{atm}$ and $R = 1.987\,\mathrm{cal{\cdot}K^{-1}{\cdot}mol^{-1}}$.

In the legends of Figs. 6.7–6.16, several abbreviations are used to stress the reaction-rate differences among the mechanisms:

$k_{mech1,mech2\sim mech3}$ means that $k_{mech1} = k_{mech2} \sim k_{mech3}$, and

$f_i\, k^{\mathrm{base}}_{mech1,mech2\sim mech3}$ means that k_{mech1} $(=f_i\, k^{\mathrm{base}}_{mech1})$ $= k_{mech2}$ $(=f_i\, k^{\mathrm{base}}_{mech2})$ $\sim k_{mech3}$ $(=f_i\, k^{\mathrm{base}}_{mech3})$, where f_i is the same in *mech1*, *mech2*, and *mech3*. k or k^{base} is omitted when there is no ambiguity. The exponents "a" (for Arrhenius), "tb" (for three-body), "fo" (for fall-off), "d" (for duplicate), and "-" (for reverse reaction) appear to stress the differences in modeling among the different mechanisms. When they do not appear, it means that all mechanisms use the same model and same direction of progress for the reaction. Sometimes a mechanism uses the sum of two different reaction rates to determine a given reaction-rate value; the two identical reactions with different reaction

rates are called duplicate reactions. In Fig. 6.11, only the resulting summed reaction rate is plotted. When a mechanism, *mech1*, uses the backward kinetic rate, $k^{\mathrm{b}1}$, of a reaction, the comparison between the corresponding forward rate, $k^{\mathrm{f}1}$, with the forward kinetic rate, $k^{\mathrm{f}2}$, of this reaction in another mechanism, *mech2*, is made possible by calculating the equilibrium constant $K_{\mathrm{c}1}$ from the thermodynamic data used in *mech1*: $k^{\mathrm{f}1} = K_{\mathrm{c}1} \cdot k^{\mathrm{b}1}$.

During the simulations, an effective concentration, $[M]$, is used that is calculated from the concentration of each species present in the model, $[M_i]$, and from the corresponding collision efficiency (that may vary among different kinetic models), f_i, through the formula: $[M] = \sum f_i M_i$. When non-default collision efficiencies are not specified in the reaction-rate model, the default value, $f_i = 1$, is used. When focusing on the reaction with the particular third body M_i, the "base" reaction rate, k^{base}, of the reaction involving the general third body M must be multiplied by the collision efficiency, f_i, to yield the actual reaction rate, $k = f_i\, k^{\mathrm{base}}$. To illustrate this, let us consider the association reaction A + B + $M_i \rightleftharpoons$ C + M_i (the following reasoning applies to dissociation reactions as well), and its reaction rate, k. In different mechanisms, this reaction may appear under two different forms: either A + B + $M_i \rightleftharpoons$ C + M_i with its associated Arrhenius reaction rate, $k_{mech1\,\mathrm{a}}(T)$, or A + B + $M \rightleftharpoons$ C + M with either an associated three-body reaction rate, $k_{mech2\,\mathrm{tb}}(T)$ (that depends only on temperature and that uses collision efficiencies), or with an associated fall-off reaction rate, $k_{mech3\,\mathrm{fo}}(T, [M])$ (that depends not only on temperature but also on pressure or $[M]$ and that uses collision efficiencies).

Mechanism	Reaction-rate model type	d[C]/dt	k = d[C]/dt / ([A][B][M_i])
mech1	Arrhenius	$k_{mech1\,\mathrm{a}}(T)$ [A][B][M_i]	$k_{mech1\,\mathrm{a}}(T)$
mech2	three-body	$k^{\mathrm{base}}_{mech2\,\mathrm{tb}}(T)$ [A][B](f_i[M_i])	$f_i \times k^{\mathrm{base}}_{mech2\,\mathrm{tb}}(T)$
mech3	fall-off	$k^{\mathrm{base}}_{mech3\,\mathrm{fo}}(T, [M])$ [A][B](f_i[M_i])	$f_i \times k^{\mathrm{base}}_{mech3\,\mathrm{fo}}(T, [M])$

Table 6.1: Comparison of a three-body reaction (A + B + $M_i \rightleftharpoons$ C + M_i) rate, k, despite possible modeling differences among various mechanisms.

Thanks to the flame-location (shown to be a good surrogate for flame speed in Section 6.1.1) sensitivity analysis coupled with the comparison of rates among mechanisms, the rate-modeling differences of the following reactions are shown to be the likely contributors to the variance in the predictions by the various mechanisms studied:

1. $\underline{\mathrm{H} + \mathrm{O_2} + M \rightleftharpoons \mathrm{HO_2} + M \quad (LS < 0)}$

Although flame position is rather sensitive to H + O_2 {+ N_2} $\rightleftharpoons$ HO_2 {+ N_2} under lean conditions, no major differences appear in the modeling of its rate: the same rates are used in G3, DLW, and WL (using a separate reaction), and no non-default collision efficiency is ever used in the other mechanisms. On the other hand, many differences appear in the modeling of the rate of the reaction

with H_2O. Flame position is extremely sensitive to the reaction with H_2O under lean conditions (and slightly less sensitive under stoichiometric conditions), whether the reaction is modeled either by a separate reaction H + O_2 {+ H_2O} ⇌ HO_2 {+ H_2O} or by the general reaction H + O_2 {+ M} ⇌ HO_2 {+ M}. For the mechanisms that use a separate reaction with H_2O (GRI, DLW, ABF, WL, and MRN), flame position is not sensitive to H + O_2 {+ M} ⇌ HO_2 {+ M} (that uses a zero collision efficiency for H_2O) at any stoichiometry for the three fuels; therefore, the reaction with H_2O is the only crucial reaction. Figure 6.7 shows that the rates for the reaction H + O_2 {+ H_2O} ⇌ HO_2 {+ H_2O} are such that $1\,k_{\rm BLB}^{\rm base} \ll k_{\rm G1,G2,ABF} \sim 16.25\,k_{\rm DAG}^{\rm base} \sim k_{\rm G3} < k_{\rm DLW,WL}$ ($k_{\rm DLW,WL} \sim 1.5\,k_{\rm G3} \sim 1.5 \cdot 18\,k_{\rm BLB}$). This may contribute to the lower predictions of DLW & WL, and to the larger predictions of BLB, in lean flames with the three fuels (these two conclusions are tempered by the analysis of the reaction HCO + M ⇌ CO + H + M). In the various SD releases, the changes brought to the fall-off reaction-rate parameters of the reaction with H_2O illustrate the lack of certainty in this important reaction rate. From S1 to S2, the base rate was kept but the collision efficiency was changed from 12 to 7, and from S2 to S3, the fall-off low-pressure limiting rate was more than doubled and the collision efficiency was changed from 7 to 16. These changes are consistent with the lower predictions of the newer SD releases (the rate parameters used in S4 & S5 are the same as in S3) in lean flames.

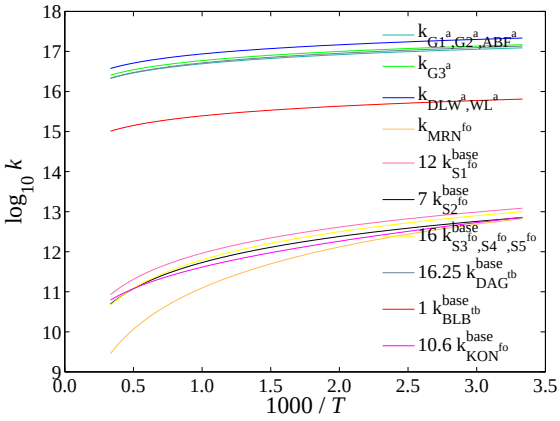

Figure 6.7: H + O_2 {+ H_2O} ⇌ HO_2 {+ H_2O} kinetic-rate comparison between mechanisms.

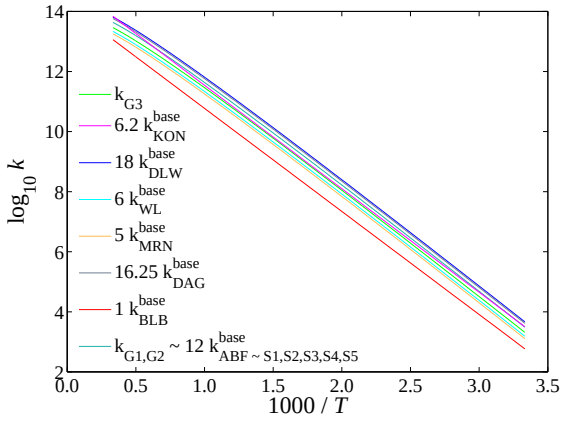

Figure 6.8: HCO + H_2O ⇌ CO + H + H_2O kinetic-rate comparison between mechanisms.

2. HCO + M ⇌ CO + H + M $\quad (LS > 0)$

Flame position is sensitive to this reaction in all flames studied, with larger sensitivities under lean conditions. The base reaction rate is approximately the same in all mechanisms except BLB and KON that use a slightly smaller one ($k_{\rm BLB\sim KON} \sim 0.5\,k_{\rm other\ mechs}$). However, a strong variance can be found among the values of the collision efficiency for H_2O. A separate reaction: H + O_2 + H_2O ⇌ HO_2 + H_2O, with its associated rate, is even used in GRI. As a result, the rates of the reaction with H_2O are at variance (see Fig. 6.8). The smaller rate in BLB does not explain its generally

larger predictions, but could contribute to its lower predictions in lean C_2H_4 flames. The largest rate in DLW probably compensates to some extent the effect of the largest rate in DLW for the reaction $H + O_2 \{+ H_2O\} \rightleftharpoons HO_2 \{+ H_2O\}$.

3. $HCO + O_2 \rightleftharpoons CO + HO_2$ $(LS < 0)$

Other than the exceptionally large sensitivity with MRN in rich CH_4 flames, flame position is sensitive to this reaction under lean conditions only. Also, the sensitivity is larger in CH_4 and C_2H_4 flames than in C_2H_6 flames. For each fuel, HCO is present only above 1000 K in the leanest flame studied, where Fig. 6.9 shows that: $k_{S1,S2,S3} < k_{DAG} < k_{S4,S5,MRN} \sim k_{G1,G2,DLW,ABF,WL} < k_{G3} < k_{KON} < k_{BLB}$. Although the rate in DLW and WL is neither small nor large relative to the other mechanisms, the extremely large sensitivity in lean flames may be a sign that this reaction rate is involved in the lower predictions of DLW and WL in lean flames. The lower predictions of the latest SD releases S4 and S5 in lean flames is consistent with the increase in the exponential prefactor of this Arrhenius reaction rate by $\sim$150 % from S3 to S4 (the same rate parameters are used in S1, S2, & S3, and in S4 & S5, respectively). The large rate in BLB may explain why BLB yields low predictions in lean C_2H_4 flames, given the noticeably large sensitivity to this reaction under these conditions. As for MRN, the low predictions in CH_4 flames under rich conditions are likely due to this reaction.

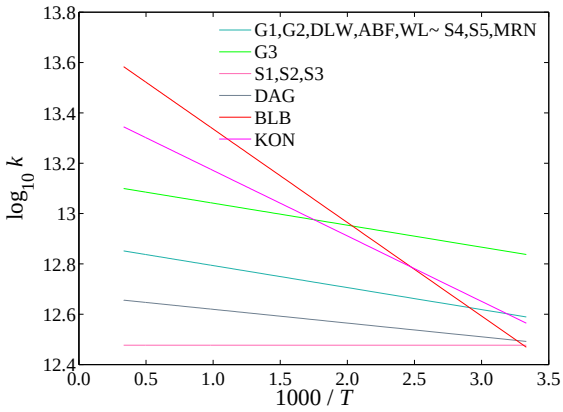

Figure 6.9: $HCO + O_2 \rightleftharpoons CO + HO_2$ kinetic-rate comparison between mechanisms.

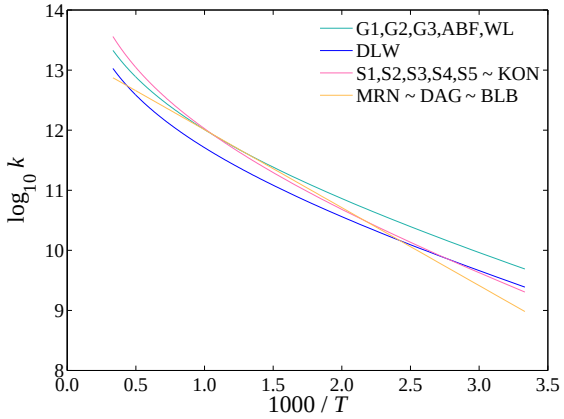

Figure 6.10: $C_2H_4 + OH \rightleftharpoons C_2H_3 + H_2O$ kinetic-rate comparison between mechanisms.

4. $C_2H_4 + OH \rightleftharpoons C_2H_3 + H_2O$ $(LS > 0)$

It is not surprising that only C_2H_4 flame positions are sensitive to this reaction since this reaction accounts for C_2H_4 consumption in flames, together with $C_2H_4 + H \rightleftharpoons$ Products (Warnatz 1984, Section 6.3). Moreover, C_2H_4 flame positions are more sensitive to this reaction under lean conditions. Figure 6.10 shows that at temperatures between 1000 K and 2000 K (where C_2H_4 and OH are simultaneously present for the flames investigated): $k_{DLW} < k_{MRN} \sim k_{DAG} \sim k_{BLB} < k_{\text{other mechs}}$ (it is explicitly noted in DLW that $k_{DLW} = 0.5\, k_{G3}$ in order to lower C_2H_4 flame speeds). The smaller

rate in DLW may contribute to its lower predictions in lean C_2H_4 flames.

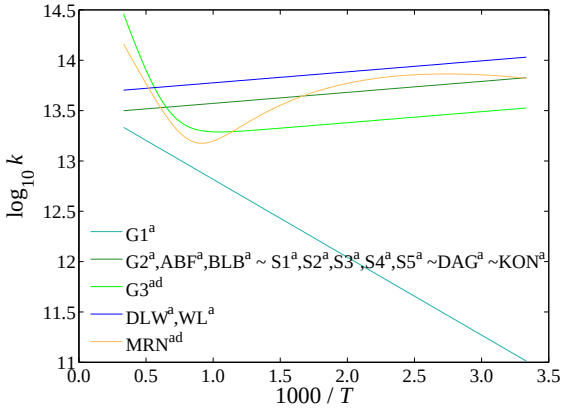

Figure 6.11: $HO_2 + OH \rightleftharpoons H_2O + O_2$ kinetic-rate comparison between mechanisms. (sum of 2 duplicate reaction rates in G3 and MRN)

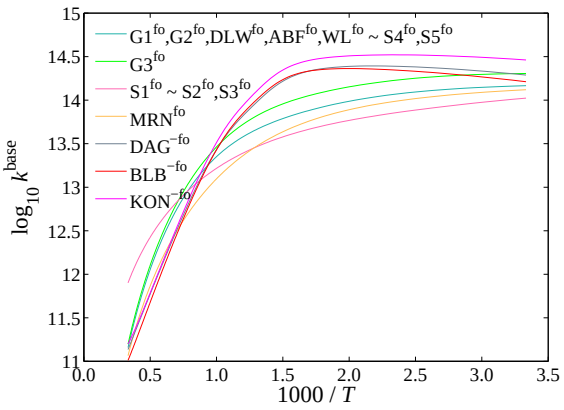

Figure 6.12: $CH_3 + H (+ M) \rightleftharpoons CH_4 (+ M)$ kinetic-rate comparison between mechanisms.

5. $\underline{HO_2 + OH \rightleftharpoons H_2O + O_2 \quad (LS < 0)}$

CH_4, C_2H_6, and C_2H_4 flame positions are sensitive to this reaction under lean conditions only. Aside from G1 included for reference, Fig. 6.11 shows that similar activation energies were chosen for the different mechanisms (almost the same slopes). The atypical rates for G3 and MRN are made possible by summing the Arrhenius rates of two duplicate reactions, thus the reaction rate is significantly increased at high temperatures (above 1800 K). However, in the lean flames investigated, the maximal temperature is below 1800 K, and OH is present with HO_2 only above $\sim$1300 K. In this range of temperatures, the rates can be ordered as follows: $k_{G1} < k_{MRN} < k_{G3} < k_{G2,ABF,BLB} \sim k_{SD} \sim k_{DAG} \sim k_{KON} < k_{DLW,WL}$. Furthermore, it is explicitly noted in DLW that $k_{DLW} \sim 1.5\,k_{G1}$ in order to lower C_2H_4 flame speeds. This may be another reason why DLW and WL yield lower predictions in lean flames.

6. $\underline{CH_3 + H\ (+\ M) \rightleftharpoons CH_4\ (+\ M) \quad (LS < 0)}$

As expected, flame position is extremely sensitive to this reaction in CH_4 flames. Flame position is also extremely sensitive to this reaction under rich conditions, in CH_4, C_2H_6, and C_2H_4 flames. S1, S2, S3, DAG, and BLB use default collision efficiencies, while the other mechanisms use non-default collision efficiencies that have more or less the same values for the third partners: argon (Ar), C_2H_6, CH_4, CO, CO_2, H_2, and H_2O. Figure 6.12 compares the base reaction rates in the various mechanisms and shows that below 1200 K: $k^{base}_{S1\sim S2,S3} < k^{base}_{G1,G2,DLW,ABF,WL\ \sim\ S4,S5} < k^{base}_{G3} < k^{base}_{DAG\sim BLB} < k^{base}_{KON}$, and above 1200 K: $k^{base}_{BLB} \sim k^{base}_{DAG} \sim k^{base}_{KON} \sim k^{base}_{MRN} < k^{base}_{G1,G2,DLW,ABF,WL\ \sim\ S4,S5} \sim k^{base}_{G3} < k^{base}_{S1\sim S2,S3}$. The reaction studied is the reverse of the CH_4 thermal decomposition, which strongly influences the ignition of CH_4 (Warnatz 1984, Section 5.1). Given that such initiation reactions are important where the fuel starts to break down to produce H atoms, and given the enhanced collision efficiencies present in S4 & S5 and absent in S1, S2, & S3, one would be tempted to conclude that S4 & S5 would yield lower flame speeds than the other SD mechanisms in rich flames, which is the case. However, in the CH_4-air stagnation-flame simulations, half of the initial amount of CH_4 is still present at 960 K, 1060 K, & 1140 K, for $\Phi = 0.7$, 1.0, & 1.3, respectively, and 90 % of the initial amount of CH_4 is decomposed at 1470 K, 1650 K, & 1730 K, for $\Phi = 0.7$, 1.0, & 1.3, respectively. This tempers the previous conclusion, which assumes that the temperature regime below 1200 K prevails.

7. $\underline{C_2H_3 + H \rightleftharpoons C_2H_2 + H_2 \quad (LS < 0)}$

Flame position is sensitive to this reaction under rich conditions, in C_2H_6 and C_2H_4 flames and even in CH_4 flames. This is not surprising since the CH_4 rich oxidation pathway includes the species: $CH_4 \rightarrow CH_3 \rightarrow C_2H_6 \rightarrow C_2H_5 \rightarrow C_2H_4 \rightarrow C_2H_3 \rightarrow C_2H_2 \rightarrow$ HCCO $\rightarrow$ CO & CO_2 , whereas the lean CH_4 oxidation pathway includes the species: $CH_4 \rightarrow CH_3 \rightarrow CH_2O \rightarrow$ HCO $\rightarrow$ CO $\rightarrow CO_2$. In all the mechanisms studied, this reaction rate does not depend on temperature, and $k_{BLB,KON} \sim k_{S1,S2,S3} < k_{G1,G2,G3,WL,DAG} < k_{ABF,S4,S5} < k_{DLW} < k_{MRN}$ (their values are respectively: $1.2{\cdot}10^{13}$,

$1.21{\cdot}10^{13}$, $3{\cdot}10^{13}$, $4{\cdot}10^{13}$, $6{\cdot}10^{13}$, and $9{\cdot}10^{13}$). The increase in the rate in the SD mechanism by a factor 3.3 from S3 to S4 may contribute to the lower predictions of the newer SD releases S4 and S5 in rich flames (the same rate parameters are used in S1, S2, & S3, and in S4 & S5, respectively). Although the rate used in MRN is the largest, it is only in the rich CH_4 flames that flame position is extremely sensitive (see Fig. 6.4). The larger rate in MRN would then likely contribute to the very low predictions of MRN in rich CH_4 flames.

8. $HO_2 + H \rightleftharpoons 2\,OH$ $\quad (LS > 0)$

Flame position is sensitive to this reaction under lean conditions, in CH_4, C_2H_6, and C_2H_4 flames (less sensitive for CH_4 and most sensitive for C_2H_4). Flame position is less sensitive in stoichiometric C_2H_4 flames. In the leanest C_2H_6 and C_2H_4 flames studied, HO_2, H, and OH are simultaneously present above $\sim$1350 K, where Fig. 6.13 shows that $k_{\mathrm{WL\sim S2\sim S3\sim S4,S5}} < k_{\mathrm{G3}} < k_{\mathrm{G1,G2,DLW,ABF}} \sim k_{\mathrm{MRN}} < k_{\mathrm{BLB}} \sim k_{\mathrm{S1\sim DAG\sim KON}}$ ($k_{\mathrm{S1}}/k_{\mathrm{WL}} \sim 1.4$ at most). This is one of the rare reactions for which WL uses a different rate than DLW. Despite the small difference in rate, the smaller rate in WL may contribute to its lower predictions compared to DLW in lean CH_4 flames. Also, the larger rate in S1 may contribute to its larger predictions compared to the other SD releases in lean flames.

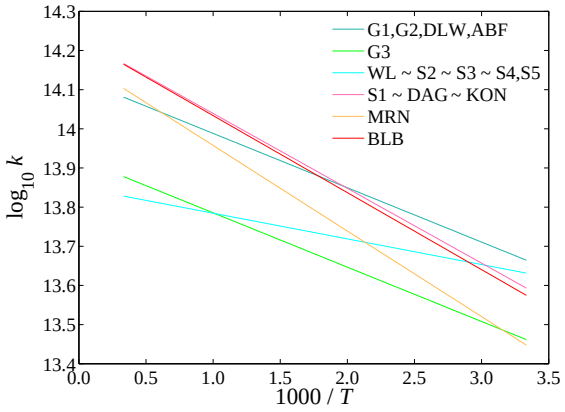

Figure 6.13: $HO_2 + H \rightleftharpoons 2\,OH$ kinetic-rate comparison between mechanisms.

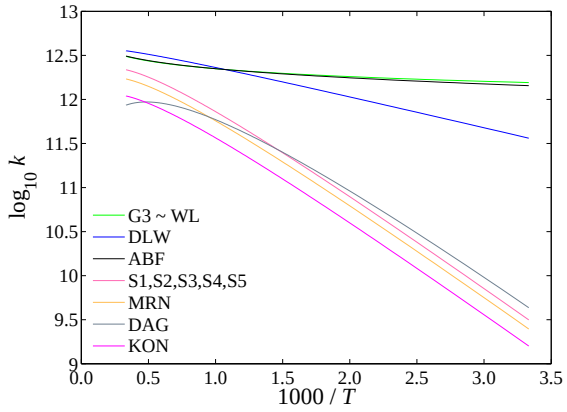

Figure 6.14: $C_2H_3 + O_2 \rightleftharpoons CH_2CHO + O$ kinetic-rate comparison between mechanisms.

9. $H + OH + M \rightleftharpoons H_2O + M$ $\quad (LS < 0)$

Flame position is quite sensitive to this reaction in all the flames studied, except in the richest C_2H_6 and C_2H_4 flames. All mechanisms use the same temperature exponent and zero activation energy in their Arrhenius model. The only difference lies in the exponential prefactor value, and $k^{\mathrm{base}}_{\mathrm{DAG}} < k^{\mathrm{base}}_{\mathrm{G1,G2,G3,DLW,ABF,WL,S1,KON\sim MRN}} < k^{\mathrm{base}}_{\mathrm{BLB}} < k^{\mathrm{base}}_{\mathrm{S2}} \sim k^{\mathrm{base}}_{\mathrm{S3,S4,S5}}$ (the values of the prefactors are respectively: $8.615{\cdot}10^{21}$, $2.2{\cdot}10^{22} \sim 2.21{\cdot}10^{22}$, $2.4{\cdot}10^{22}$, and $3.8{\cdot}10^{22} \sim 4{\cdot}10^{22}$). All SD releases use the same non-default collision efficiencies, thus a comparison of their base reaction rates is sufficient. The significant increase in the prefactor value from S1 to S2 ($k^{\mathrm{base}}_{\mathrm{S3,S4,S5}} \sim 1.05\,k^{\mathrm{base}}_{\mathrm{S2}} \sim 1.05 \cdot 1.7\,k^{\mathrm{base}}_{\mathrm{S1}}$) in order to improve burning-velocity agreement (reported in the log of updates to the SD mechanism,

see San Diego mechanism reference) may contribute to the larger flame-position (or flame-speed) predictions of S1 compared to the other SD releases in CH_4 flames and in lean & stoichiometric C_2H_6 & C_2H_4 flames. Not all mechanisms use the same non-default collision efficiencies: the value of the collision efficiency associated with H_2O differs significantly among all the mechanisms studied. For the reaction with H_2O, the comparison of the actual rates (collision efficiency multiplied by base rate) becomes: $1\,k^{\rm base}_{\rm BLB} < 3.65\,k^{\rm base}_{\rm G1,G2,G3,DLW,ABF,WL} < 6.4\,k^{\rm base}_{\rm MRN\sim KON} \sim 16.25\,k^{\rm base}_{\rm DAG} < 12\,k^{\rm base}_{\rm S1} < 12\,k^{\rm base}_{\rm S2} \sim 12\,k^{\rm base}_{\rm S3,S4,S5}$. The smaller rate in BLB probably contributes to the large predictions of BLB. WL is the only mechanism to have enhanced the collision efficiencies of C_2H_2 and C_2H_4 (both tripled), therefore the enhanced rate of WL in presence of C_2H_4 may contribute to its expected better performance compared to DLW in C_2H_4 flames (lower predictions near stoichiometric conditions).

10. $CH_3 + HO_2 \rightleftharpoons CH_3O + OH \quad (LS > 0)$

Flame positions are mildly sensitive to this reaction in all the flames studied. In all the mechanisms investigated, this reaction rate does not depend on temperature, and $k_{\rm S2,S3,S4,S5,DAG} < k_{\rm MRN} < k_{\rm DLW,WL} < k_{\rm BLB,KON} < k_{\rm G1,G2,ABF,S1} < k_{\rm G3}$ (their values are respectively: $0.5{\cdot}10^{13}$, $0.7{\cdot}10^{13}$, $1.34{\cdot}10^{13}$, $1.8{\cdot}10^{13}$, $2.0{\cdot}10^{13}$, and $3.78{\cdot}10^{13}$). The larger rate of this reaction used in old releases like G1, G2, & S1, and used in ABF, has been revised in S2 ($k_{\rm S2,S3,S4,S5} = k_{\rm DAG} = 0.25\,k_{\rm S1}$) in order to improve agreement with propane autoignition times (reported in the log of updates to the SD mechanism, see San Diego mechanism reference). The larger rate in ABF and S1 may contribute to their overall larger predictions compared to DLW & WL and the newer SD releases, respectively. The smaller rate in DAG is consistent with its low predictions.

11. $C_2H_3 + O_2 \rightleftharpoons CH_2CHO + O \quad (LS > 0)$

The vinoxy radical (CH_2CHO) is one of the major intermediates during C_2H_4 oxidation (Wang & Laskin 1998; it plays an essential role in C_2H_4 ignition, see Egolfopoulos & Dimotakis 1998). It is therefore not surprising that flame position is sensitive to this reaction in C_2H_4 flames. Given that the vinyl radical (C_2H_3) is involved, it is also not surprising that flame position is sensitive to this reaction under rich conditions. In the C_2H_4 flames and in the rich flames (for the three fuels) studied: C_2H_3, CH_2CHO, & O are simultaneously present above 1000 K, and the maximum temperature encountered is 2000 K. In this range of temperatures, Fig. 6.14 shows that $k_{\rm KON} < k_{\rm DAG} < k_{\rm MRN} < k_{\rm S1,S2,S3,S4,S5} < k_{\rm ABF} \sim k_{\rm G3} \sim k_{\rm WL} < k_{\rm DLW}$. The large sensitivity to this reaction and the relatively small rate in MRN probably contribute to its low predictions in rich CH_4 and in C_2H_4 flames. The large rates in DLW & WL may contribute to the increasing trend in the predictions from lean to rich conditions, and although the difference between the rates in WL & DLW is small (10 %), it may explain the lower predictions of WL compared to DLW in C_2H_4 flames.

12. $CH_2OH + H \rightleftharpoons CH_3 + OH \quad (LS > 0)$

Flame position is only (mildly) sensitive to this reaction in rich CH_4 flames, and in lean & stoichiometric CH_4 flames with the BLB mechanism only. In the CH_4 flames studied, the species involved

in this reaction are simultaneously present above $\sim 1300\,\mathrm{K}$. At these temperatures, Fig. 6.15 shows a larger rate for BLB, which may contribute (given the large sensitivities) to its large predictions in CH_4 flames.

13. $CH_3 + OH \rightleftharpoons CH_2(S) + H_2O \quad (LS > 0)$

Flame position is more sensitive to this reaction in CH_4 flames, and is not sensitive to it in rich C_2H_6 and C_2H_4 flames. Figure 6.16 shows that at high temperatures (where OH is present): $k_{\mathrm{DAG}} < k_{\mathrm{S1,S2,S3}} < k_{\mathrm{other\ mechs}}$. The smaller rate in DAG may contribute to its low predictions.

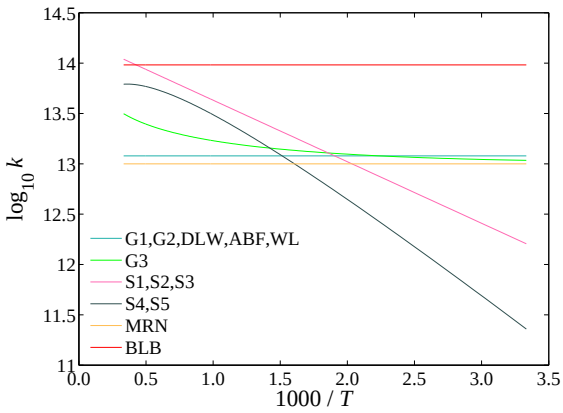

Figure 6.15: $CH_2OH + H \rightleftharpoons CH_3 + OH$ kinetic-rate comparison between mechanisms.

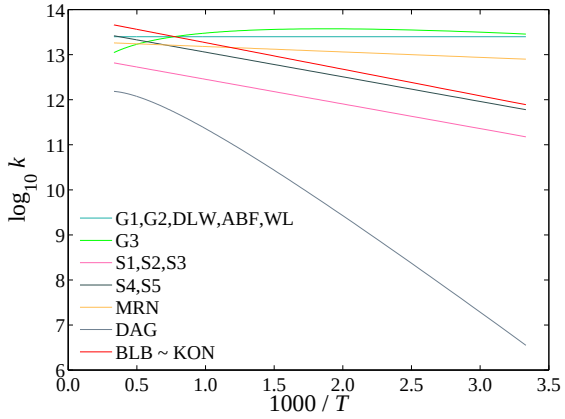

Figure 6.16: $CH_3 + OH \rightleftharpoons CH_2(S) + H_2O$ kinetic-rate comparison between mechanisms.

Chapter 7

Summary and conclusions

The work presented here includes new experimental results for non-reacting impinging jets at Reynolds numbers, Re, between 400 & 9000, and for atmospheric-pressure premixed laminar C_3H_8- & C_3H_6-air flames under very lean to very rich conditions. The C_3-flame data will be submitted to the PrIMe database (http://www.primekinetics.org/) for use as validation and optimization targets by model developers.

Flame simulations would only rarely converge with the Marinov mechanism (MRN), the Dagaut et al. mechanism (DAG), the Battin-Leclerc et al. C_0–C_2 mechanism (BLB), the Battin-Leclerc et al. C_3 mechanism (BL), and the Konnov mechanism (KON), whereas simulations converge with the more-robust mechanisms: GRI-Mech 1.2 (G1), GRI-Mech 2.11 (G2), GRI-Mech 3.0 (G3), the Davis-Law-Wang 1999 mechanism (DLW), the Appel-Bockhorn-Frenklach 2000 mechanism (ABF), the Wang-Laskin 1998 mechanism (WL), and the five releases of the San Diego mechanism (S1, S2, S3, S4, and S5). Therefore, a continuation technique was developed to transition from a solution obtained with a robust mechanism to a new solution obtained with a less-robust mechanism. Stagnation-flame simulations with mechanisms using a large number of species and reactions are very rare in the literature, due to the lack of robustness of these mechanisms. The novel continuation technique documented in the present work has been key. In flames where predictions by small to reasonable-size mechanisms fail, sensitivity analysis conducted on simulations performed with large mechanisms (that should in theory contain most of the reactions and associated reaction rates to model heavy hydrocarbon oxidation) should indicate which species and reactions are missing in the smaller, more robust mechanisms, and therefore lead to better robust mechanisms.

A particle-tracking velocimetry (PTV) technique based on recent technology was devised and validated against a previous investigation of non-reacting impinging jets at Reynolds numbers between 400 and 1400. Measurements up to $Re = 9000$ were performed thanks to the increased PTV spatio-temporal resolution, and confirm that the scaled axial-velocity profile is well represented by an error-function fit with one free parameter that is dependent on Re. In the C_3-flame investigation, accurate, high-resolution velocity profiles were measured using the PTV technique. Under conditions

where the kinetics are appropriately modeled, the entire experimental profile is matched by the simulated profile corrected for particle inertia and thermophoresis, whose effects are discernible only in the high-gradient regions within the flame and close to the wall. Accounting for finite particle-track interval effects is key when lower-resolution velocimetry systems are used.

In the C_3-flame investigation, CH-radical relative concentration profiles were recorded simultaneously by planar laser-induced fluorescence (PLIF). From the information contained in the velocity and CH-radical profiles, two specific scalar validation targets were extracted that capture a significant portion of combustion chemistry: the stagnation flame speed, S_u (insensitive to the particle-tracking corrections), and the CH-peak position, x_{CH}. S_u and x_{CH} can be used to assess the adequacy of kinetic models and do not require any particle-tracking corrections. The lower level of uncertainty in comparisons of measured and simulated x_{CH} values demonstrates the superiority of this validation target over comparisons of S_u.

An experimental error band, Σ_{exp}, taking into account the uncertainty on $S_{u,exp}$ & $x_{CH,exp}$ and the uncertainty on $S_{u,sim}$ & $x_{CH,sim}$ (propagating the uncertainties on the measurements of the simulation input parameters: pressure, equivalence ratio, dilution level, inlet velocity, inlet velocity gradient, inlet temperature, and wall temperature, thanks to the sensitivity of the solution to each simulation input parameter) was evaluated to assess the relative comparison of simulations with experiment. $\sigma_{x_{CH,sim}}$ is larger than $\sigma_{x_{CH,exp}}$, which justifies the extra care spent on the measurements of the premixed combustible mixture composition (measured by thermal mass-flow meters calibrated before each experiment), the inlet temperature, and the inlet velocity & velocity-gradient boundary conditions. More generally, special attention should be paid when comparing flame simulations to experimental data far from stoichiometric conditions, because the sensitivity of the solution to the uncertainty on the measurement of the combustible-mixture composition becomes especially large. An analysis of the uncertainty on the model parameters (the kinetic reaction rates being the most uncertain) that would lead to a simulation error band on the predictions would allow unarguable statements about the validity of the different models regarding their C_1–C_3 flame-speed predictions.

The 2005/12 release of the San Diego mechanism (S5) and BL were found to be the "best" mechanisms to simulate the C_3H_8 and C_3H_6 flames investigated, respectively. When considering all of the C_3H_8 and C_3H_6 flames investigated (each fuel was given the same weight), S5 was found to have the "best" overall performance over the range of fuels and stoichiometries studied. The term "best" is quoted because the present work addresses flame speeds only; similar studies focused on phenomena such as ignition and extinction would bring essential complementary knowledge and may find that another model gives better agreement with these other data sets.

The sensitivity analyses with DLW and S5 reveal that the few reactions that affect flame positions (or flame speeds) are very similar for C_3H_8 and C_3H_6 flames. These reactions include several reactions with C_3H_6 and the allyl radical aC_3H_5. Except for the very rich C_3H_6 flame (for which

flame speeds are largely overpredicted by all the mechanisms tested), BL and KON predict similar results in C_3H_8 and C_3H_6 flames. Better agreement was found in C_3H_8 flames for DLW and S5. Nevertheless, DLW and S5 show larger variation with experiment in C_3H_6 flames. This suggests that reaction pathways for the unsaturated fuel C_3H_6 are missing in DLW and S5 that are present in the larger reaction-number mechanisms BL and KON. Such deficiencies cannot be assessed using sensitivity analyses performed with DLW and S5.

Further analysis was performed on C_1–C_2 flames. A comparative study of fifteen available mechanisms that include C_1–C_3 kinetics was conducted in stagnation flames, and model predictions were compared to experiment to assess the relative performance of each mechanism. Atmospheric CH_4-, C_2H_6-, and C_2H_4-air flames were simulated at all stoichiometries. The information contained in each of these stagnation flames can be reduced to one scalar only: the CH-peak position (indicating flame location), which is a surrogate for flame speed in this geometry. Comparison of the CH-peak position with experiment provided a broad validation test for each mechanism. Two criteria were defined, each quantifying the adequacy of a mechanism to predict flames under any burning regime. DLW, the 2005/03 release of the San Diego mechanism (S2), and the 2005/10 release of the San Diego mechanism (S4) were found to be the "best" mechanism to simulate the CH_4, C_2H_6, and C_2H_4 flames investigated, respectively. This dependency on fuel of the "best" mechanism is not a good sign for the current state of combustion modeling. When considering the CH_4, C_2H_6, and C_2H_4 flames investigated (each fuel was given the same weight), S4 was found to have the "best" overall performance.

Given a reaction set needed to model CH_4, C_2H_6, and C_2H_4 combustion, the open question is to find an optimal set of reaction-rate parameters. To this end, a comparison of the hundreds of constants present in the different kinetic mechanisms was performed, based solely on their influence on the CH-peak position (surrogate for flame speed). A sensitivity analysis of the CH-peak position was conducted in CH_4, C_2H_6, and C_2H_4 flames under very lean, stoichiometric, and very rich conditions, in order to guide a detailed comparison of the most critical reaction rates used in the different mechanisms. This approach has several limits: sensitivity analysis is not useful if important species or reactions are not present in the mechanism, and branching ratios cannot be compared in this manner. However thirteen reactions were thus identified that have leverage on the predictions under specific conditions, and whose rate differences likely contribute to the discrepancies observed in flame-location predictions. This knowledge can be used by kineticists to improve the mechanisms' performance for a targeted set of conditions (to correct a bad flame-speed prediction with a certain fuel and burning regime for example).

The present work makes new C_3 flame experimental data available — and shows how such data can be used to validate different combustion kinetic models. It also shows how comparisons of simulations with experiment combined with comparisons of models between each other allow a focus

on a small number of key reactions and reaction rates among the hundreds of reactions present in the mechanisms, in order to reach a better description of the dominant chemical kinetics.

Appendix A

Particle-tracking velocimetry (PTV)

A.1 Advantages of the new PTV technology

A continuous laser beam was chopped at a maximum frequency, $\nu_{\mathrm{c,max}} = 2.4\,\mathrm{kHz}$, with the previous particle streak velocimetry (PSV) technology (Bergthorson et al. 2005a). In the new PTV technique, the pulsed laser maximum repetition rate is $\nu_{\mathrm{p,max}} = 20\,\mathrm{kHz}$. Combined with a gain of a factor 4 in the axial-direction resolution of the imager, the resulting increase in the spatio-temporal resolution is a factor 16, resulting in smaller particle-tracking corrections and allowing the investigation of faster-burning flames. Dots of diameters 2–3 pixels are processed, therefore differences of 8 pixels between the dot centroids can be resolved, which correspond to $20\,\mu$m in the C_3 flames investigated (see Chapter 5). PTV is more efficient than PSV because half the light is blocked with PSV (the chopper wheel shutters the laser beam half the time) and because light is focused in a $\sim 0.2\,\mu$s pulse, versus a minimum streak duration of $208\,\mu$s. All the light is used with PTV, whereas only the light at the edges of the streak is used with PSV. The larger PTV-laser power (enabling pulse energies of 4.5 mJ at 20 kHz and 9 mJ at 10 kHz, compared to 1 mJ before) combined with the large (14-bit) dynamic range of the PTV imager enables post-processing of the particle dots even within the flame. Also, the scatter in the data was reduced from the old PSV to the new PTV technique (see ϵ_{rms} in Table 3.1, Table 3.2, and Table D.5), reducing the uncertainty in the velocity estimates, and therefore also in the velocity boundary conditions at the inlet (see Table E.1).

Figure A.3 shows the PTV setup that includes a spherical expanding lens, a spherical converging lens to collimate the laser beam, a photodiode linked to an oscilloscope to measure the actual laser repetition rate, three prisms to adjust the laser-beam location, a cylindrical converging lens to make the laser sheet, a spatial filter, and a prism for a 90-degree turn. The bottom-right picture in Fig. A.3 shows how the laser sheet illuminates the flame between the nozzle and the stagnation plate, and Fig. A.3 shows particle trajectories illuminated by the laser sheet in a stoichiometric CH_4-air flame.

The left part of Fig. A.3 shows the raw intensity surface corresponding to a portion of a dotted trajectory of a moving particle in a PTV image, superimposed with a thresholding plane for each dot. Only pixels with intensities larger than the thresholding level are kept (as shown on the right part of Fig. A.3) and used to determine the centroid of each dot, which is the intensity-weighted barycenter. When the particle goes through the flame, noise coming from the flame is added to the background noise and makes it difficult to locate the imaged particles. However, as long as the imager is not saturated, it is possible to alleviate this difficulty by allowing the thresholding value to vary along the axial (x) direction, choosing the threshold to be the same as the intensity at the edge of the box bounding the dot, as recommended by J. Bergthorson (private communication), thus it is possible to substract the noise coming from the flame and resolve velocities within the flame. Once the location of each dot is determined, the particle displacement, $x_{\mathrm{i}+1} - x_{\mathrm{i}-1}$, multiplied by ν_{p} provides the velocity estimate, located at the average position of the particle over the period between pulses, $x_{\mathrm{i}} = 0.5\,(x_{\mathrm{i}+1} + x_{\mathrm{i}-1})$.

A.2 Non-reacting impinging-jet PTV images

Figure A.4 shows the PTV images of the non-reacting impinging jets at variable Reynolds number, Re.

A.3 Premixed C_3H_8- and C_3H_6-air stagnation-flame PTV images

Figures A.5a–j show sample-PTV images of the C_3 stagnation flames investigated. 10–20 such images are usually needed to determine a full velocity profile from the inlet to the vicinity of the stagnation plate.

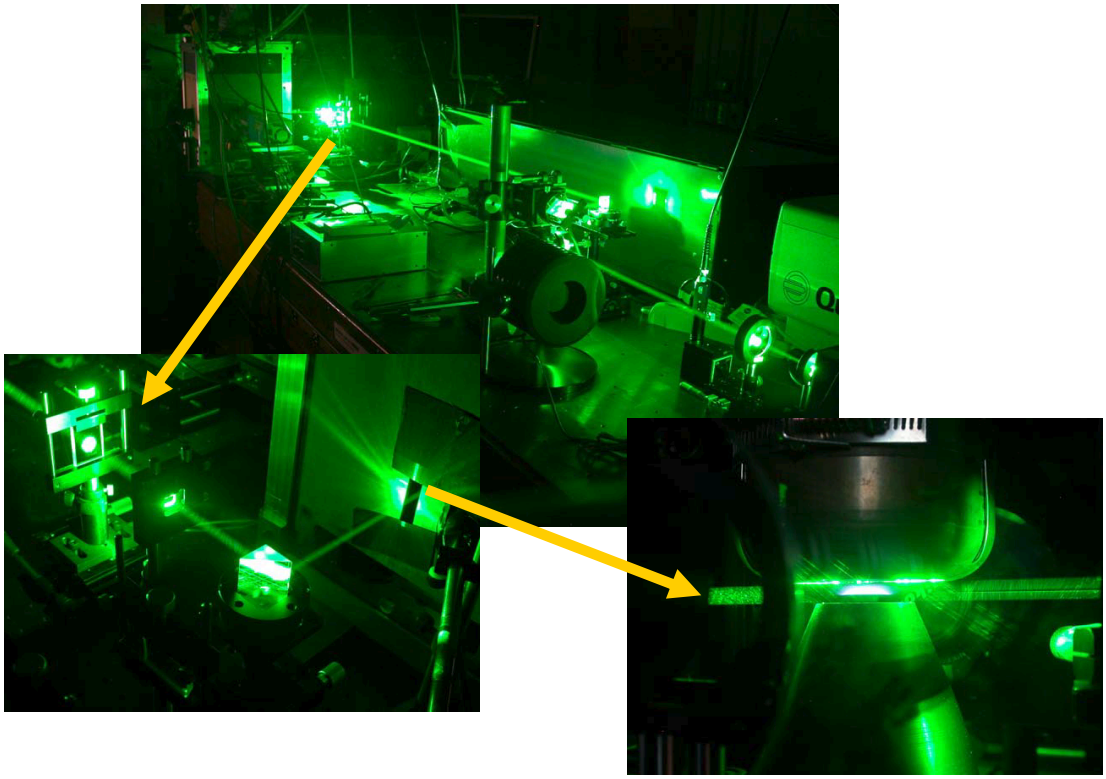

Figure A.1: PTV setup.

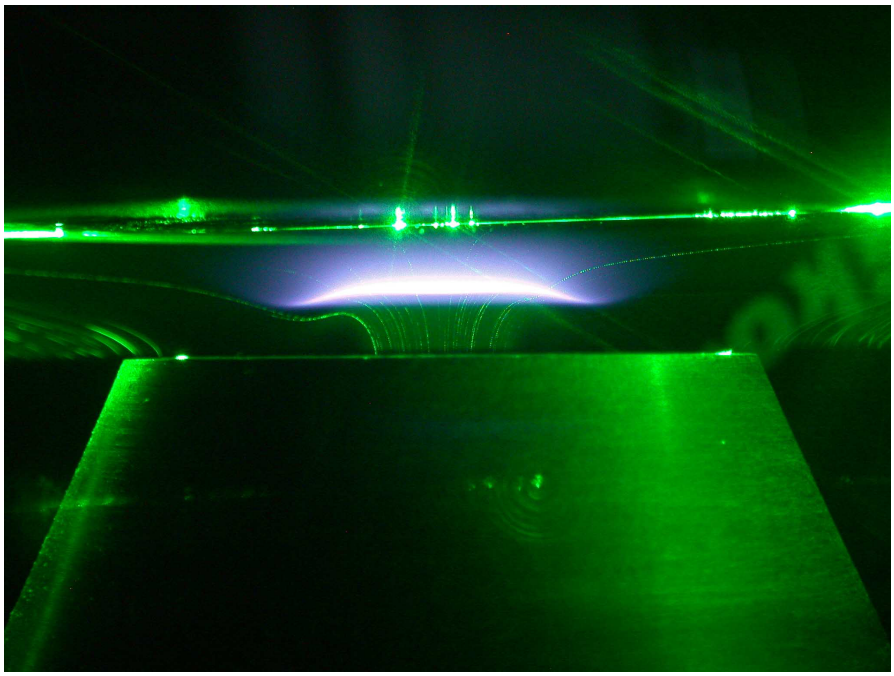

Figure A.2: PTV picture in a stoichiometric CH_4-air flame.

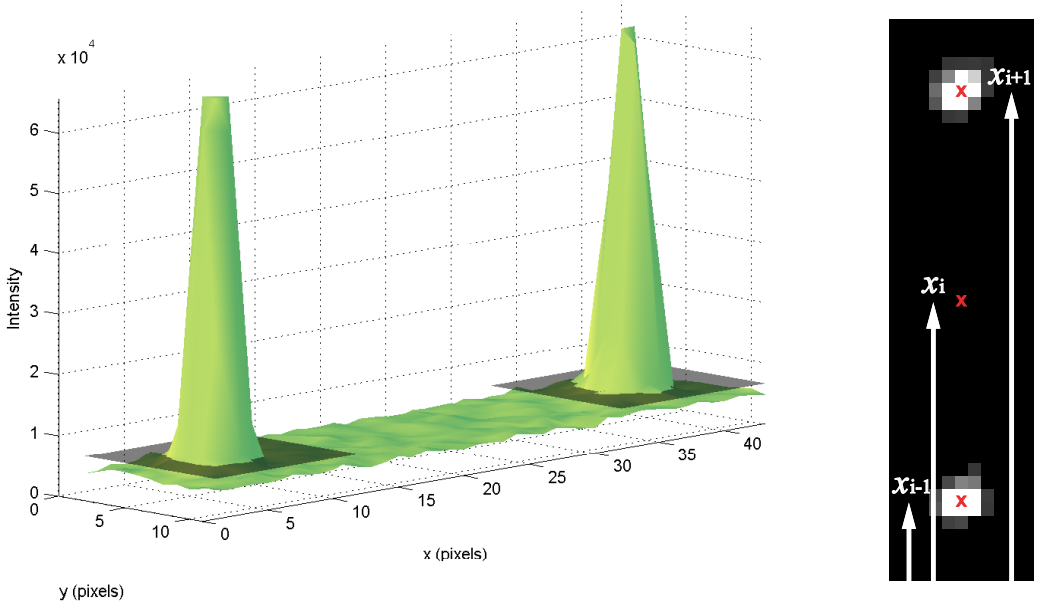

Figure A.3: PTV dots.

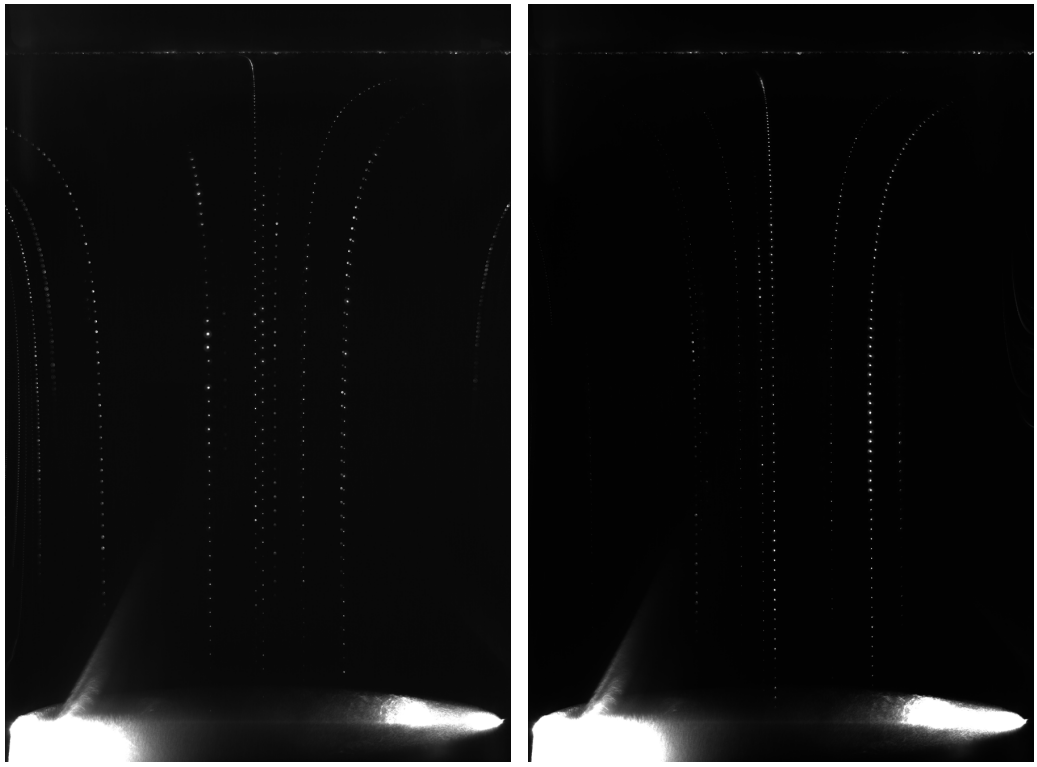

(a) $Re = 407$ ($\nu_\mathrm{p} = 2\,\mathrm{kHz}$)

(b) $Re = 708$ ($\nu_\mathrm{p} = 5\,\mathrm{kHz}$)

Figure A.4: Sample non-reacting impinging-jet PTV images.

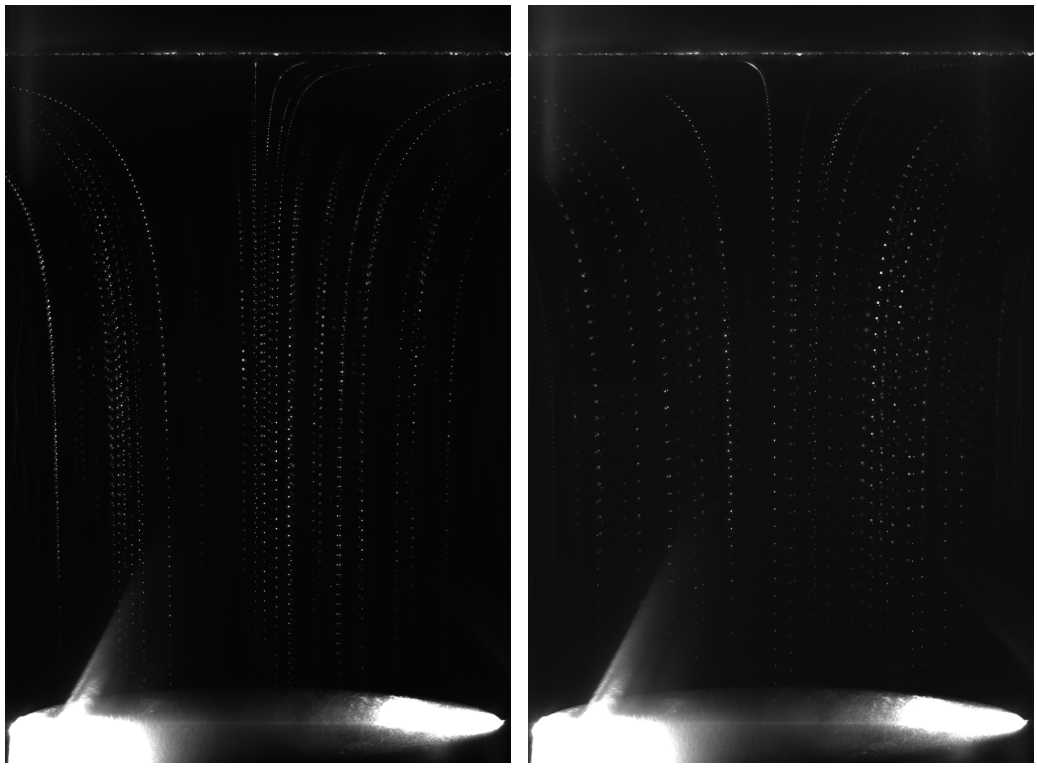

(c) $Re = 1409$ ($\nu_\mathrm{p} = 10\,\mathrm{kHz}$)

(e) $Re = 2524$ ($\nu_\mathrm{p} = 10\,\mathrm{kHz}$)

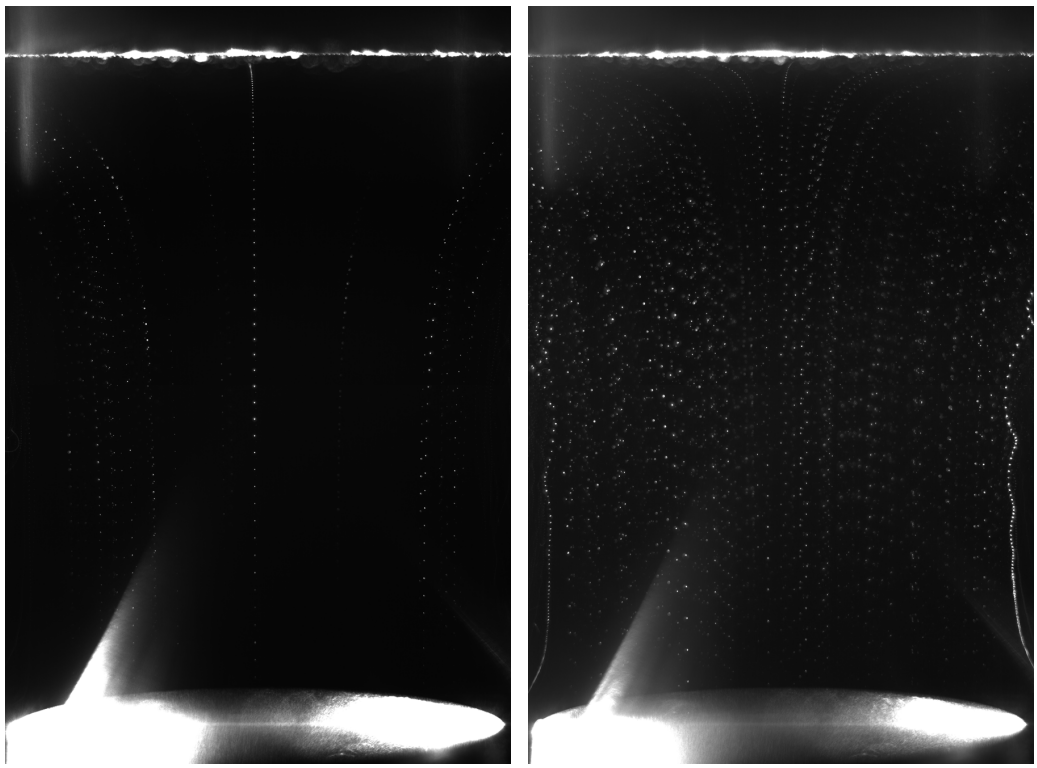

(d) $Re = 5049$ ($\nu_\mathrm{p} = 20\,\mathrm{kHz}$)

(f) $Re = 9120$ ($\nu_\mathrm{p} = 20\,\mathrm{kHz}$)

Figure A.4: Sample non-reacting impinging-jet PTV images. (cont.)

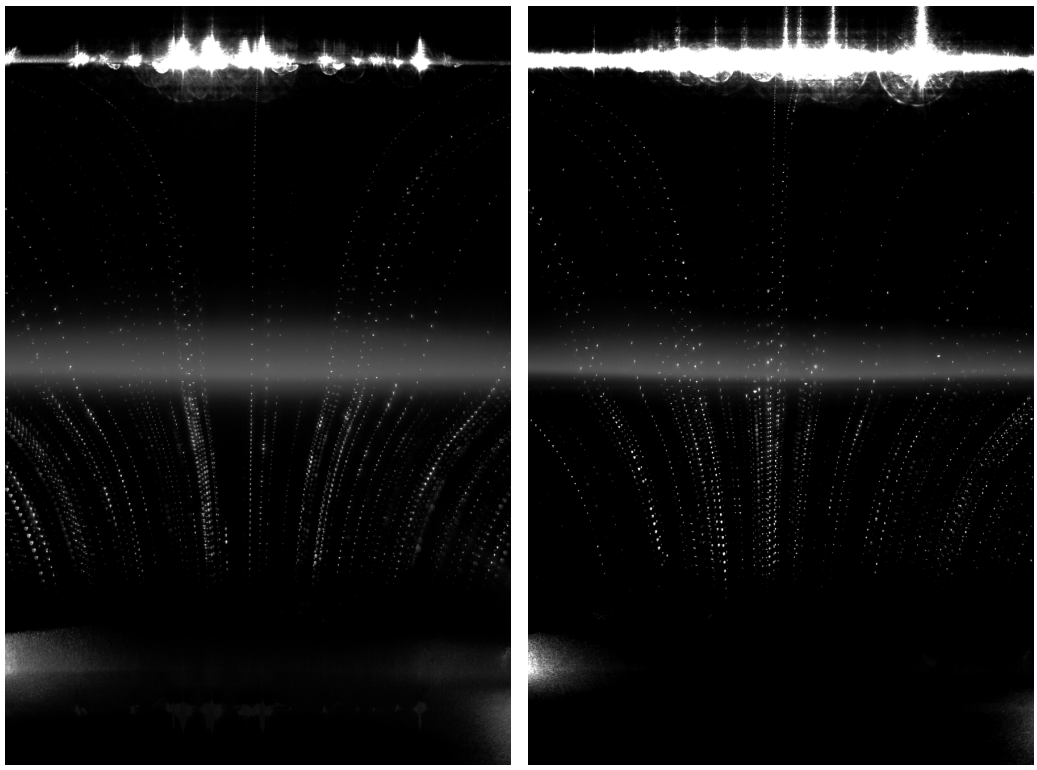

(a) C_3H_8, $\Phi = 0.7$ ($\nu_p = 5\,\mathrm{kHz}$)

(f) C_3H_6, $\Phi = 0.7$ ($\nu_p = 5\,\mathrm{kHz}$)

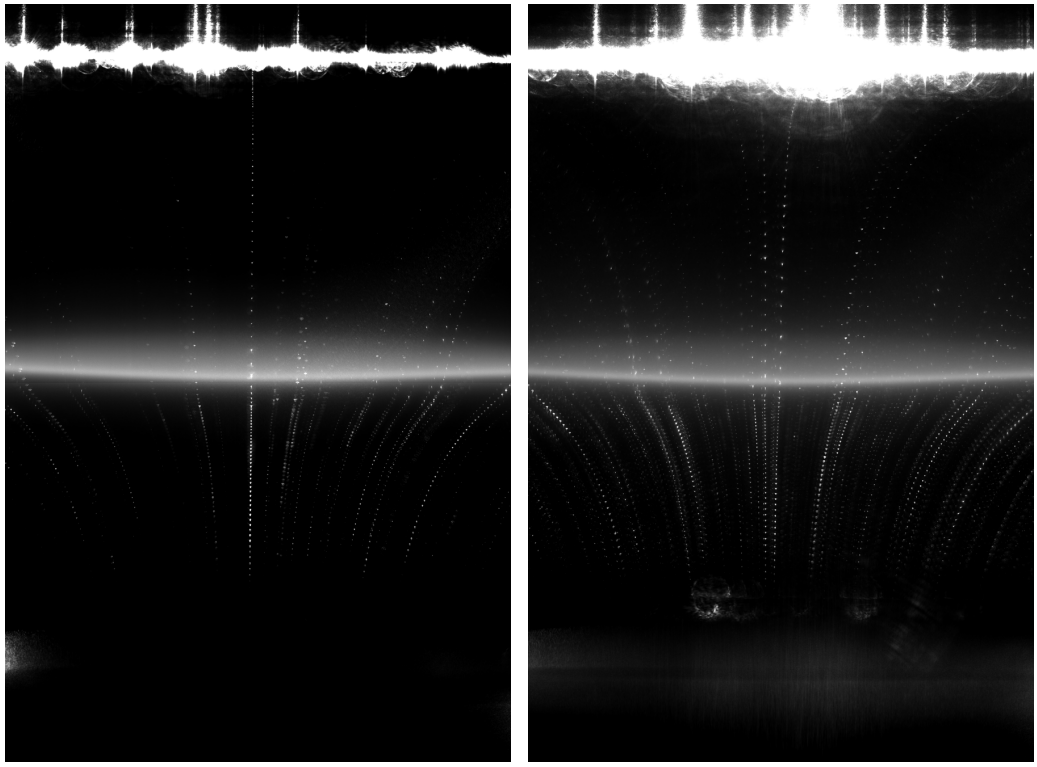

(b) C_3H_8, $\Phi = 0.85$ ($\nu_p = 10\,\mathrm{kHz}$)

(g) C_3H_6, $\Phi = 0.85$ ($\nu_p = 10\,\mathrm{kHz}$)

Figure A.5: Sample stagnation-flame PTV images.

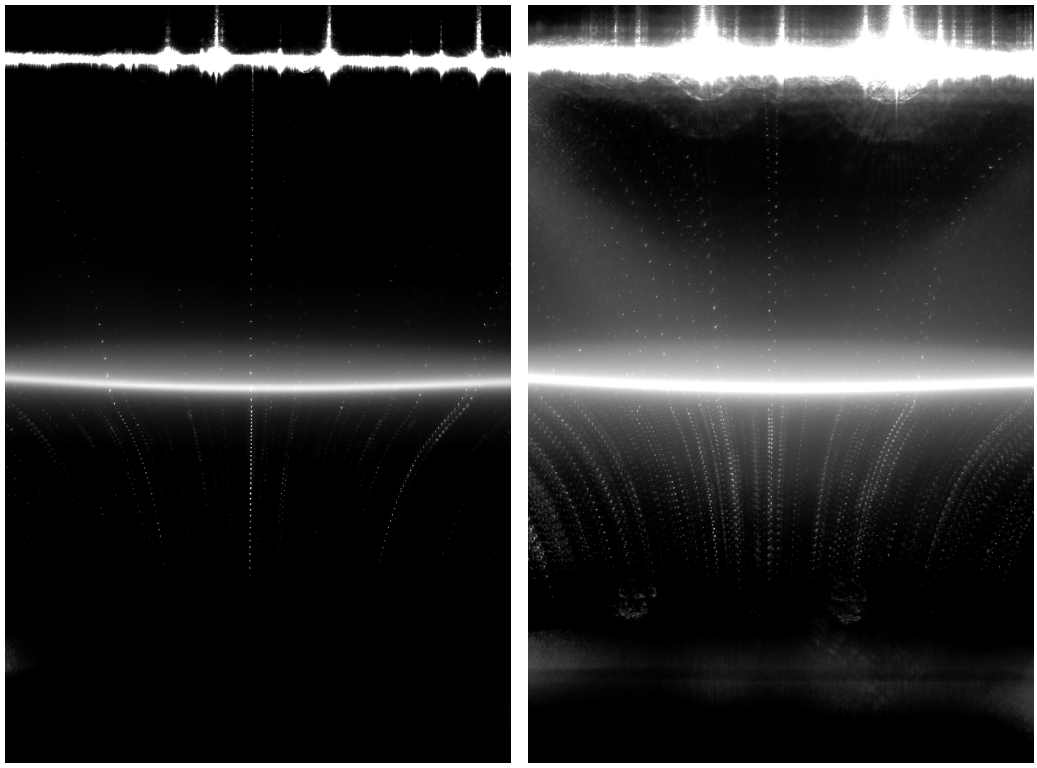

(c) C_3H_8, $\Phi = 1.0$ ($\nu_p = 10\,\mathrm{kHz}$)

(h) C_3H_6, $\Phi = 1.0$ ($\nu_p = 10\,\mathrm{kHz}$)

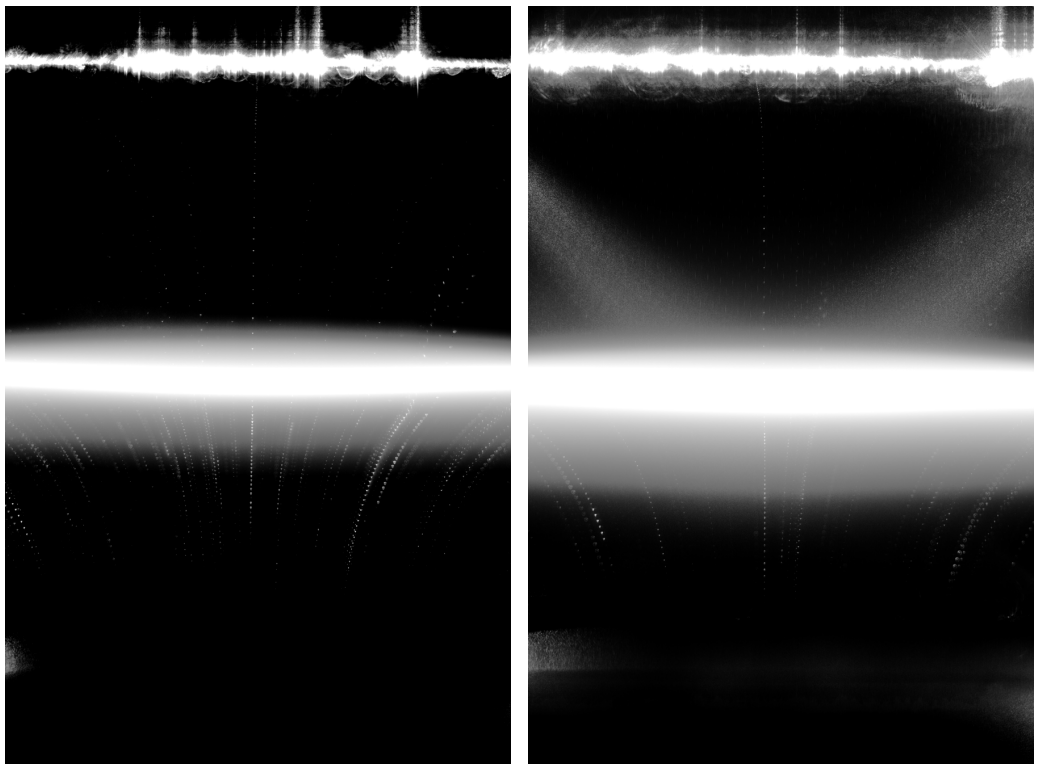

(d) C_3H_8, $\Phi = 1.25$ ($\nu_p = 10\,\mathrm{kHz}$)

(i) C_3H_6, $\Phi = 1.3$ ($\nu_p = 10\,\mathrm{kHz}$)

Figure A.5: Sample stagnation-flame PTV images. (cont.)

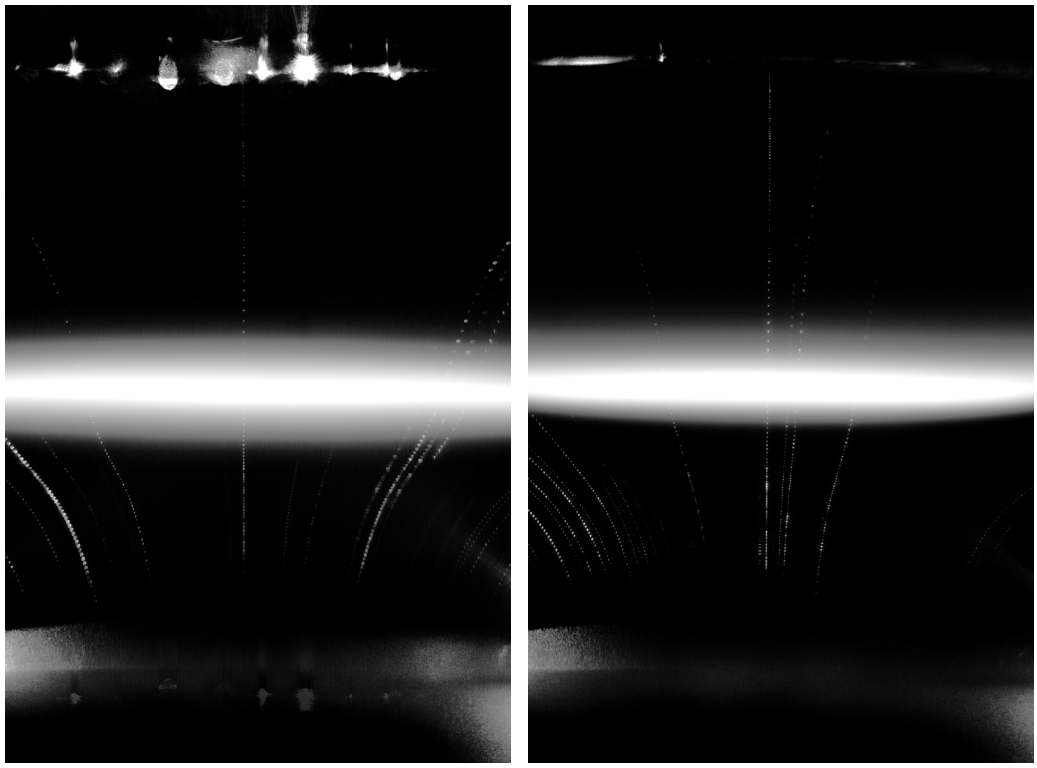

(e) C_3H_8, $\Phi = 1.5$ ($\nu_p = 5\,\mathrm{kHz}$)

(j) C_3H_6, $\Phi = 1.6$ ($\nu_p = 5\,\mathrm{kHz}$)

Figure A.5: Sample stagnation-flame PTV images. (cont.)

Appendix B

Premixed C_3H_8- and C_3H_6-air stagnation-flame CH-PLIF images

Figures B.1a–j show composite CH-PLIF images of the C_3 stagnation flames investigated. For each flame, the left part of the composite image is a single image that shows the signal-to-noise ratio, and the right part of the composite image is the averaged image (over 1000 images). The off-resonance averaged image has been substracted from both the single and averaged images, which explains why the stagnation plate does not appear. For display purpose, a rescaling factor, N, has been used in the moderately rich flame images (Figs. B.1d and B.1f, where the CH-PLIF signal is maximum), and larger rescaling factors were used in the other figures.

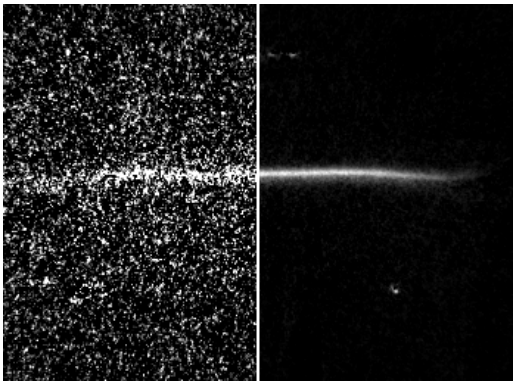

(a) C_3H_8, $\Phi = 0.7$ (intensity $\times$ 16 N)

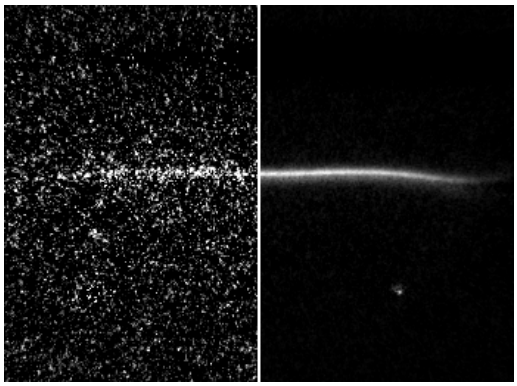

(f) C_3H_6, $\Phi = 0.7$ (intensity $\times$ 16 N)

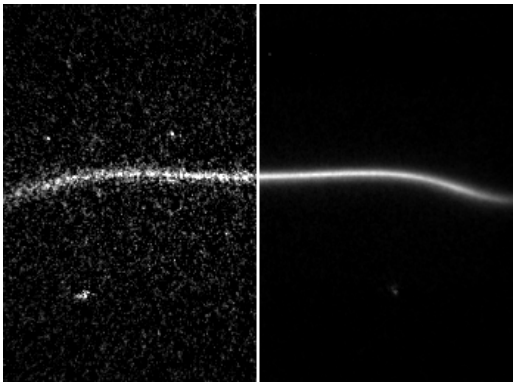

(b) C_3H_8, $\Phi = 0.85$ (intensity $\times$ 4 N)

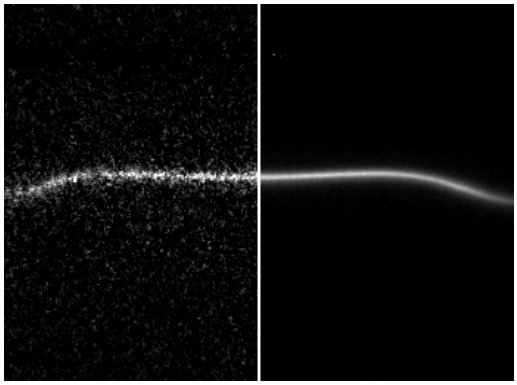

(g) C_3H_6, $\Phi = 0.85$ (intensity $\times$ 4 N)

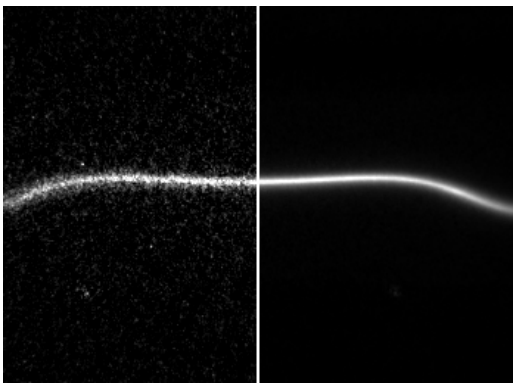

(c) C_3H_8, $\Phi = 1.0$ (intensity $\times$ 2 N)

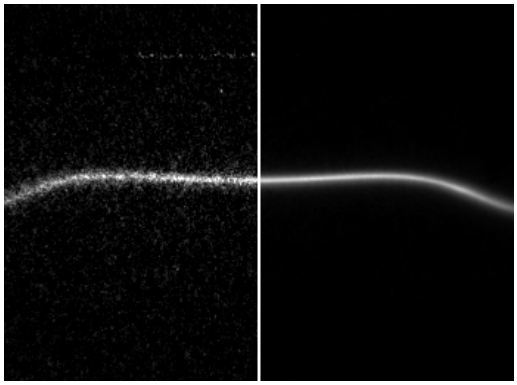

(h) C_3H_6, $\Phi = 1.0$ (intensity $\times$ 2 N)

Figure B.1: Stagnation-flame composite CH-PLIF images: single image (left) and averaged image over 1000 images (right).

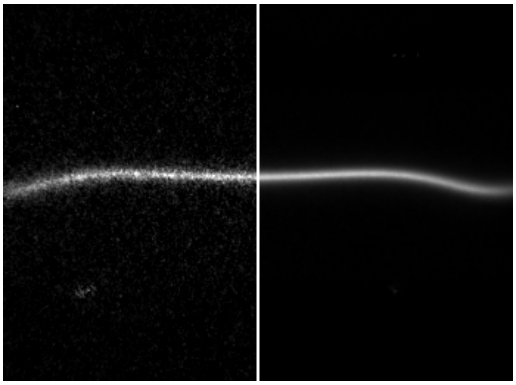

(d) C_3H_8, $\Phi = 1.25$ (intensity $\times$ N)

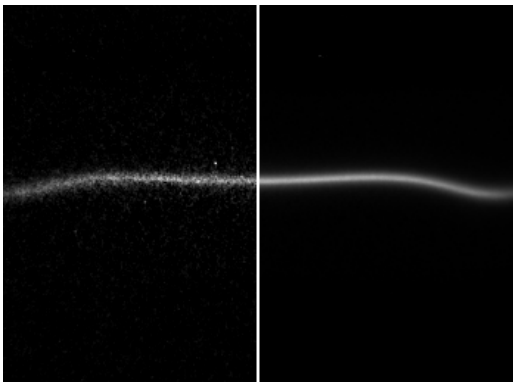

(i) C_3H_6, $\Phi = 1.3$ (intensity $\times$ N)

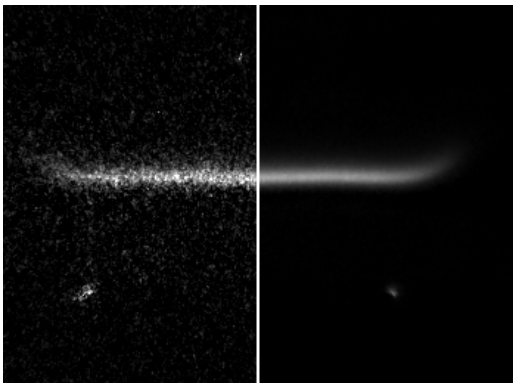

(e) C_3H_8, $\Phi = 1.5$ (intensity $\times$ 2 N)

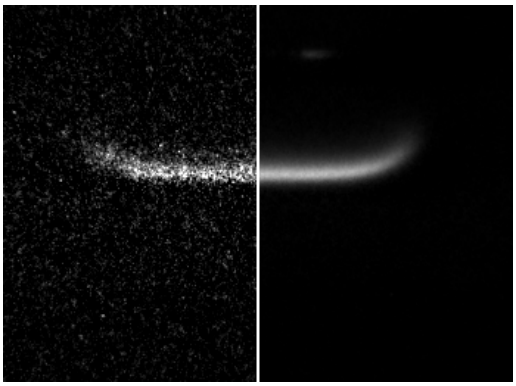

(j) C_3H_6, $\Phi = 1.6$ (intensity $\times$ 4 N)

Figure B.1: Stagnation-flame composite CH-PLIF images: single image (left) and averaged image over 1000 images (right). (cont.)

Appendix C

Cantera stagnation-flame simulations

C.1 Convergence study

A convergence study was conducted for the (adaptive mesh) stagnation-flame simulations performed in the present work (Benezech et al. 2006). The solution with the maximum number of gridpoints that converged was compared to simulations with smaller numbers of gridpoints. The relative difference between the maximum temperature, maximum velocity, & CH-peak position of simulations with 300–500 gridpoints and those of the simulation with the largest number of gridpoints that had converged (750) was smaller than 1 %. Thus all simulation results present in this work have between 300 and 500 gridpoints and are fully converged.

C.2 Impact of Soret effect on flame simulations

Because of a bug in CANTERA, the thermal diffusion (also referred to as "Soret effect") was not included in the multicomponent stagnation-flame simulations in Bergthorson & Dimotakis (2007). In 2007, another bug was found, and the fix suggested, by Anatoli Mokhov in the CANTERA user's group interactions (Goodwin): in "StFlow.cpp", the formula for the gradient of the logarithm of temperature, `gradlogT`, was incorrect:

Instead of "$\texttt{gradlogT} = 2.0 * (\texttt{T}(\texttt{x},\texttt{m}+1) - \texttt{T}(\texttt{x},\texttt{m}))/(\texttt{T}(\texttt{x},\texttt{m}+1) + \texttt{T}(\texttt{x},\texttt{m}))$",

it should be "$\texttt{gradlogT} = 2.0 * (\texttt{T}(\texttt{x},\texttt{m}+1) - \texttt{T}(\texttt{x},\texttt{m}))/(\texttt{T}(\texttt{x},\texttt{m}+1) + \texttt{T}(\texttt{x},\texttt{m}))/(\texttt{z}(\texttt{m}+1) - \texttt{z}(\texttt{m}))$" .

The missing multiplicative factor $1/dz = 1/(\texttt{z}(\texttt{m}+1) - \texttt{z}(\texttt{m}))$ can be very large within the flame, where a finer mesh is used.

Both bugs were fixed in a modified version of the CANTERA source code, such that all the mul-

ticomponent simulations in the present work include thermal diffusion. Moreover, multicomponent simulations that do not include thermal diffusion were also performed in the CH_4, C_2H_6, and C_2H_4 flames discussed in this study, in order to quantify the impact of thermal diffusion on the results shown in Bergthorson & Dimotakis (2007). Figures C.1a–c show the difference in predicted CH-peak location, $x_{\mathrm{CH,sim}}$, with and without thermal diffusion, scaled by the stoichiometric CH-layer thickness simulated with S2, i.e., $\delta_{\mathrm{CH,S2},\Phi=1}$, in the CH_4, C_2H_6, and C_2H_4 flames investigated, respectively. The S2 mechanism was used because of its superior performance among the mechanisms used in Bergthorson & Dimotakis (2007) (G3, DLW, S1, and S2), in the CH_4, C_2H_6, and C_2H_4 flames over the range of stoichiometries investigated. The larger differences shown on Fig. C.1a at $\Phi = 1.2$ and 1.3 are consistent with the larger differences around $\Phi \simeq 1.2$ between CH_4 laminar flame speeds predicted with and without thermal diffusion in Ern & Giovangigli (1999). Except the larger differences (between 0.5 and 1 $\delta_{\mathrm{CH,S2},\Phi=1}$) in the $\Phi = 1.2$ and 1.3 CH_4 flames, the difference in flame location with and without thermal diffusion remains smaller than $0.5\,\delta_{\mathrm{CH,S2},\Phi=1}$ for all other CH_4, C_2H_6, and C_2H_4 flames investigated.

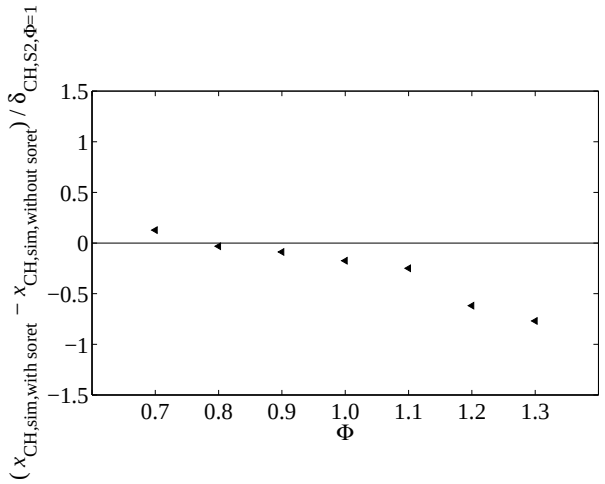

(a) CH_4 flames

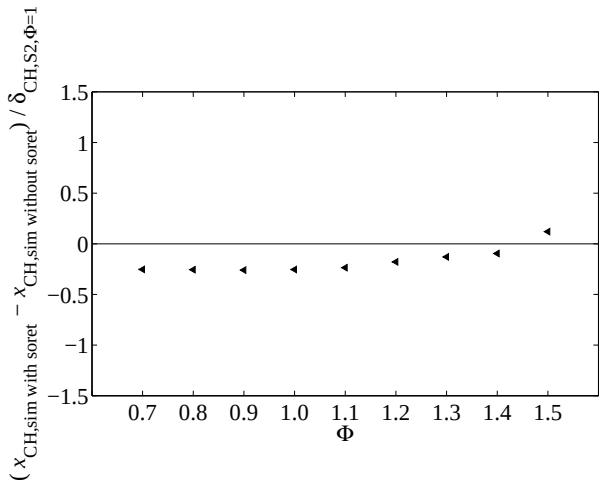

(b) C_2H_6 flames

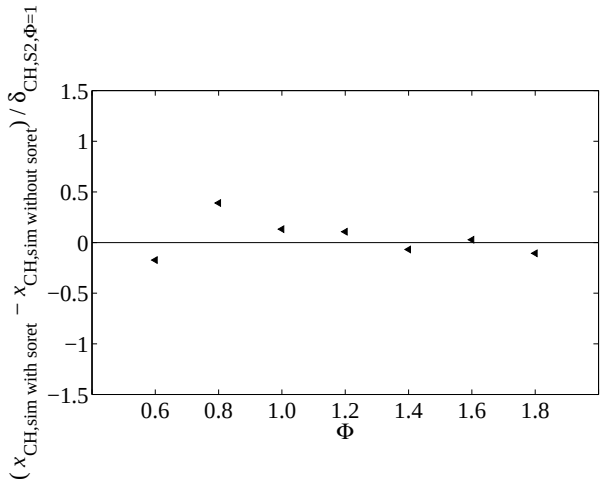

(c) C_2H_4 flames

Figure C.1: Comparison of CH-peak locations predicted by S2 mechanism with and without thermal diffusion included.

Appendix D

Premixed stagnation-flame data

D.1 Boundary conditions

The boundary conditions, BC, corresponding to each experimental flame are reported in Table D.1. At the simulation domain inlet, ℓ, velocity, u_ℓ, spreadrate, $V_\ell = \frac{1}{2}\frac{du}{dx}(\ell)$, and temperature, T_ℓ, are provided. At the stagnation wall, only the temperature, $T_{\rm wall}$, is provided.

D.2 Particle-tracking-correction parameters

Table D.2 shows the experimental parameters used as inputs in the particle-tracking corrections: the diameter, $d_{\rm part}$, the density, $\rho_{\rm part}$, & the thermal conductivity, $K_{\rm part}$, of the particles used for the velocimetry, and the particle-tracking frequency, $\nu_{\rm c}$ in the experiments where particle-streak velocimetry (PSV) was used, or $\nu_{\rm p}$ in the experiments where particle-tracking velocimetry (PTV) was used. Zeeosphere particles were used in the CH_4 experiments (Bergthorson & Dimotakis 2007), and Al_2O_3 particles were used in the C_2H_6 & C_2H_4 experiments (Bergthorson & Dimotakis 2007) as well as in the C_3H_8 & C_3H_8 experiments (present work). The Zeeosphere-particle features are: $d_{\rm part} = 3\,\mu$m, $\rho_{\rm part} = 2400\,{\rm kg/m^3}$, & $K_{\rm part} = 2.3\,{\rm W/(m.K)}$, and the Al_2O_3-particle features are: $d_{\rm part} = 1\,\mu$m, $\rho_{\rm part} = 3830\,{\rm kg/m^3}$, & $K_{\rm part} = {\rm K}_{{\rm part},Al_2O_3}(T)$, where the values of ${\rm K}_{{\rm part},Al_2O_3}(T)$ are shown in Table D.3.

			Inlet BC				Stagnation-plate BC
fuel	Φ	$\%O_2/(O_2+N_2)$	ℓ (mm)	u_ℓ (m/s)	V_ℓ (1/s)	T_ℓ (K)	T_{wall} (K)
	0.70	21.0	6	0.312	50	295.0	320.1
	0.80	21.0	6	0.531	80	295.0	325.8
	0.90	21.0	6	0.671	100	295.0	331.7
CH_4	1.00	21.0	6	0.764	118	295.0	335.9
	1.10	21.0	6	0.769	119	295.0	338.2
	1.20	21.0	6	0.660	102	295.0	331.3
	1.30	21.0	6	0.339	83	295.0	336.9
	0.70	21.0	6	0.440	64	294.3	339.1
	0.80	21.0	6	0.636	96	294.3	341.8
	0.90	21.0	6	0.809	121	294.3	344.1
	1.00	21.0	6	0.913	136	294.3	347.0
C_2H_6	1.10	21.0	6	0.939	145	294.3	346.4
	1.20	21.0	6	0.879	135	294.3	339.4
	1.30	21.0	6	0.729	113	294.3	346.0
	1.40	21.0	6	0.512	82	294.3	343.8
	1.50	21.0	6	0.313	58	294.3	347.7
	0.60	21.0	6	0.518	77	294.3	325.5
	0.80	19.5	6	0.883	129	294.3	340.8
	1.00	17.0	6	0.837	121	294.3	340.0
C_2H_4	1.20	16.5	6	0.765	118	294.3	339.4
	1.40	18.0	6	0.742	118	294.3	338.4
	1.60	21.0	6	0.742	126	294.3	341.5
	1.80	21.0	6	0.402	76	294.3	334.9
	0.70	21.0	6	0.386	65	298.0	314.8
	0.85	21.0	6	0.642	115	298.1	333.8
C_3H_8	1.00	21.0	5.5	0.627	153	298.0	346.0
	1.25	21.0	5.75	0.596	125	297.4	336.8
	1.50	21.0	6.75	0.286	47	296.7	310.5
	0.70	21.0	5.5	0.393	85	298.1	319.7
	0.85	21.0	5.75	0.669	133	298.4	338.9
C_3H_6	1.00	21.0	5.5	0.712	176	298.5	351.7
	1.30	21.0	5.75	0.602	135	297.4	339.4
	1.60	21.0	7	0.250	37	297.0	306.4

Table D.1: Boundary conditions for flame simulations.

fuel	Φ	d_{part} (μm)	ρ_{part} (kg/m^3)	K_{part} (W/(m.K))	ν_{c} (kHz)	ν_{p} (kHz)
	0.70	3	2400	2.3	1.6	-
	0.80	3	2400	2.3	2.0	-
	0.90	3	2400	2.3	2.0	-
CH_4	1.00	3	2400	2.3	2.0	-
	1.10	3	2400	2.3	2.0	-
	1.20	3	2400	2.3	2.0	-
	1.30	3	2400	2.3	2.0	-
	0.70	1	3830	$K_{\text{part,Al}_2\text{O}_3}(T)$	1.6	-
	0.80	1	3830	$K_{\text{part,Al}_2\text{O}_3}(T)$	2.4	-
	0.90	1	3830	$K_{\text{part,Al}_2\text{O}_3}(T)$	2.4	-
	1.00	1	3830	$K_{\text{part,Al}_2\text{O}_3}(T)$	2.4	-
C_2H_6	1.10	1	3830	$K_{\text{part,Al}_2\text{O}_3}(T)$	2.4	-
	1.20	1	3830	$K_{\text{part,Al}_2\text{O}_3}(T)$	2.4	-
	1.30	1	3830	$K_{\text{part,Al}_2\text{O}_3}(T)$	2.4	-
	1.40	1	3830	$K_{\text{part,Al}_2\text{O}_3}(T)$	2.0	-
	1.50	1	3830	$K_{\text{part,Al}_2\text{O}_3}(T)$	1.6	-
	0.60	1	3830	$K_{\text{part,Al}_2\text{O}_3}(T)$	1.6	-
	0.80	1	3830	$K_{\text{part,Al}_2\text{O}_3}(T)$	2.4	-
	1.00	1	3830	$K_{\text{part,Al}_2\text{O}_3}(T)$	2.4	-
C_2H_4	1.20	1	3830	$K_{\text{part,Al}_2\text{O}_3}(T)$	2.4	-
	1.40	1	3830	$K_{\text{part,Al}_2\text{O}_3}(T)$	2.4	-
	1.60	1	3830	$K_{\text{part,Al}_2\text{O}_3}(T)$	2.4	-
	1.80	1	3830	$K_{\text{part,Al}_2\text{O}_3}(T)$	1.6	-
	0.70	1	3830	$K_{\text{part,Al}_2\text{O}_3}(T)$	-	5.0
	0.85	1	3830	$K_{\text{part,Al}_2\text{O}_3}(T)$	-	10.0
C_3H_8	1.00	1	3830	$K_{\text{part,Al}_2\text{O}_3}(T)$	-	10.0
	1.25	1	3830	$K_{\text{part,Al}_2\text{O}_3}(T)$	-	10.0
	1.50	1	3830	$K_{\text{part,Al}_2\text{O}_3}(T)$	-	5.0
	0.70	1	3830	$K_{\text{part,Al}_2\text{O}_3}(T)$	-	5.0
	0.85	1	3830	$K_{\text{part,Al}_2\text{O}_3}(T)$	-	10.0
C_3H_6	1.00	1	3830	$K_{\text{part,Al}_2\text{O}_3}(T)$	-	10.0
	1.30	1	3830	$K_{\text{part,Al}_2\text{O}_3}(T)$	-	10.0
	1.60	1	3830	$K_{\text{part,Al}_2\text{O}_3}(T)$	-	5.0

Table D.2: Experimental parameters used in the particle-tracking corrections.

T (K)	200	400	600	800	1000	1200	1500	2000	2500
$K_{\text{part,Al}_2\text{O}_3}(T)$ (W/(m.K))	55	26.4	15.8	10.4	7.85	6.55	5.66	6	6.4

Table D.3: Al_2O_3-particle thermal conductivity. (Dewitt & Incropera 1990)

D.3 Key experimental results

Table D.4 reports the values of the two key scalars: CH-peak location, x_{CH}, and stagnation flame speed, S_{u}, in all the experiments considered in this study. The CH_4, C_2H_6, & C_2H_4 flame experiments were performed by Bergthorson & Dimotakis (2007), and the C_3H_8 & C_3H_6 flame experiments were performed in the present work.

S_{u} is determined from a cubic fit performed locally, around the minimum-velocity point. Table D.4 also reports the strain rate value, $\sigma = |du/dx|_{\max}$, in each flame. A parabolic fit to the cold-flow portion (between the inlet and the inflection point located close to the minimum-velocity point) of the velocity profile is performed, and σ is evaluated at the inflection point, and therefore corresponds to the maximum slope of the velocity profile upstream of the flame.

No correction to the measured values of x_{CH} and S_{u}, such as the first-order correction suggested by Markstein (Markstein 1951), using curvature Markstein lengths (Bradley et al. 1996), is attempted to account for the effect of the small curvature of the experimental flames (Sone 2007). The curvatures, κ, were obtained from parabolic fits to the central portion (around the jet axis) of the two-dimensional CH-PLIF data (concave towards the stagnation plate for all flames studied) and are listed in Table D.4. x_{CH} is determined from the same parabolic fit to the two-dimensional CH-PLIF data. To determine the experimental CH-peak location, firstly, the intensity averaged value and standard deviation (over the 1000 CH-PLIF images) are calculated for each pixel in the CH-PLIF image. Next, for every pixel column, pixels with intensities larger than 20 % of the column maximum intensity are selected, and the pixel of maximum intensity is determined by a an intensity-weighted barycenter calculation using these selected pixels, to subpixel accuracy. The uncertainty on the pixel of maximum intensity is derived from the barycenter calculation by using the intensity standard deviation at the pixels selected to compute the barycenter. In our experimental set-up, although each flame investigated is nearly flat, their small curvature gives them a camel's back shape in most cases, and a simple parabolic shape under very rich conditions. A parabola is fitted to the pixels (one by column) of maximum intensity, weighted by the inverse squared uncertainties, in the center portion of the flame (in between the two inflection points between the center part and each hump of the flame camel's back shape). Finally, the CH-peak location is determined from the center (corresponding to the jet axis) value of this parabola, the stagnation plate location, and the pixel-to-mm conversion factor.

Flame		CH PLIF		PSV or PTV		Experiments
fuel	Φ	κ (1/m)	$x_{\mathrm{CH,exp}}$ (mm)	σ (1/s)	$S_{\mathrm{u,exp}}$ (m/s)	source
	0.70	26.9	4.068	120	0.217	A
	0.80	40.1	3.886	203	0.309	A
	0.90	47.4	3.914	258	0.382	A
CH_4	1.00	51.3	3.978	302	0.428	A
	1.10	52.0	3.946	295	0.434	A
	1.20	36.5	3.906	260	0.389	A
	1.30	69.4	4.472	166	0.284	A
	0.70	28.2	3.967	159	0.265	A
	0.80	45.5	3.974	240	0.356	A
	0.90	47.0	3.971	320	0.425	A
	1.00	47.4	3.990	355	0.465	A
C_2H_6	1.10	50.5	4.006	371	0.497	A
	1.20	46.4	3.972	351	0.470	A
	1.30	46.7	3.972	281	0.409	A
	1.40	35.4	3.923	199	0.312	A
	1.50	19.7	3.936	127	0.225	A
	0.60	29.8	3.920	188	0.307	A
	0.80	50.9	4.069	331	0.479	A
	1.00	48.5	4.015	317	0.467	A
C_2H_4	1.20	45.8	4.082	294	0.442	A
	1.40	48.3	4.044	296	0.440	A
	1.60	43.9	4.018	306	0.438	A
	1.80	35.0	3.999	171	0.281	A
	0.70	30.2	4.122	142	0.258	B
	0.85	49.8	4.190	250	0.376	B
C_3H_8	1.00	52.4	4.310	328	0.452	B
	1.25	39.7	4.206	264	0.395	B
	1.50	29.3	4.117	98	0.189	B
	0.70	35.5	4.106	189	0.292	B
	0.85	44.5	4.222	270	0.430	B
C_3H_6	1.00	46.3	4.328	373	0.501	B
	1.30	43.8	4.303	303	0.422	B
	1.60	14.6	4.005	83	0.165	B

A: Bergthorson & Dimotakis (2007)
B: Present work

Table D.4: Key experimental results.

D.4 Fits to stagnation-flame experimental velocity and CH-PLIF profiles

D.4.1 Stagnation-flame velocity profile fits

The CH_4, C_2H_6, and C_2H_4 flame-velocity profiles measured with the PSV technique (Bergthorson & Dimotakis 2007) were shown to be accurately represented by a 10-parameter fit (Bergthorson 2005a, Appendix B.2; Bergthorson 2005b). However, the C_3H_8 and C_3H_6 flame-velocity measurements from the present work performed closer to the wall thanks to the PTV technique indicate that there is an inflection point in the velocity profile in the hot region (between the stagnation plate and the maximum-velocity point). Therefore, the second-order polynomial, p_1 (Bergthorson 2005a, Appendix B.2), chosen by Bergthorson (2005a) to describe the velocity profile in the hot region is replaced by a third-order polynomial, p_h, in the present work. The analytic expression of the resulting 11-parameter velocity-profile fit, u_fit, is presented in Eq. D.1–D.5.

$$p_\mathrm{h}(x) \;=\; a_{1,\mathrm{ph}}\,(x - x_{0,\mathrm{ph}}) \;+\; a_{2,\mathrm{ph}}\,(x - x_{0,\mathrm{ph}})^2 \;+\; a_{3,\mathrm{ph}}\,(x - x_{0,\mathrm{ph}})^3 \tag{D.1}$$

$$p_\mathrm{c}(x) \;=\; a_{1,\mathrm{pc}}\,(x - x_{0,\mathrm{pc}}) \;+\; a_{2,\mathrm{pc}}\,(x - x_{0,\mathrm{pc}})^2 \tag{D.2}$$

$$e_1(x) \;=\; 0.5\left(1 - \mathrm{erf}\big(b_{\mathrm{e}1}\,(x - x_{0,\mathrm{e}1})\big)\right) \tag{D.3}$$

$$e_2(x) \;=\; 0.5\left(1 + \mathrm{erf}\big(b_{\mathrm{e}2}\,(x - x_{0,\mathrm{e}2})\big)\right) \tag{D.4}$$

$$u_\mathrm{fit}(x) \;=\; p_\mathrm{h}(x) \,\times\, e_1(x) \;+\; p_\mathrm{c}(x) \,\times\, e_2(x) \;\;, \tag{D.5}$$

where $\mathrm{erf}(x) \;=\; 2/\sqrt{\pi}\,\int_0^x e^{-t^2}\,dt$

and $x_{0,\mathrm{ph}}$, $a_{1,\mathrm{ph}}$, $a_{2,\mathrm{ph}}$, $a_{3,\mathrm{ph}}$, $x_{0,\mathrm{pc}}$, $a_{1,\mathrm{pc}}$, $a_{2,\mathrm{pc}}$, $x_{0,\mathrm{e}1}$, $b_{\mathrm{e}1}$, $x_{0,\mathrm{e}2}$, & $b_{\mathrm{e}2}$ are the 11 fit parameters. p_h represents the hot flow region, p_c represents the cold flow region, and the error functions e_1 & e_2 provide a smooth transition between the cold and hot flow regions.

The fits from Bergthorson (2005b) to the velocity profiles for CH_4, C_2H_6, & C_2H_4 flames and the fits from the present work to the velocity profiles for C_3H_8 & C_3H_6 flames are shown in Table D.5, together with their range of applicability, $[x_\mathrm{min},\, x_\mathrm{max}]$. Table D.5 also shows the rms difference, ϵ_rms, between the velocity fit and the velocity data, as well as the rms difference scaled by the stagnation flame speed.

Figures D.1a–j show the velocity-fit and velocity-data profiles in the C_3H_8 and C_3H_6 flames investigated. Under moderately rich conditions (see Figs. D.1d and D.1i), there is a region within the chemiluminescence zone where PTV data was not obtained. In this region, the fit is unconstrained and should therefore not be used. The 11-parameter fit is able to represent the velocity profiles for all CH_4, C_2H_6, C_2H_4, C_3H_8, and C_3H_6 experiments discussed here.

Table D.5: Fits to experimental velocity profiles.

Flame		Velocity-profile-fit parameters											$[x_{\min},\ x_{\max}]$	$\epsilon_{\rm rms}$	$\epsilon_{\rm rms}/S_{\rm u,exp}$	Fits
fuel	Φ	$x_{0,\rm ph}$	$a_{1,\rm ph}$	$a_{2,\rm ph}$	$a_{3,\rm ph}$	$x_{0,\rm pc}$	$a_{1,\rm pc}$	$a_{2,\rm pc}$	$x_{0,\rm e1}$	$b_{\rm e1}$	$x_{0,\rm e2}$	$b_{\rm e2}$	(mm)			source
	0.70	0.3387	0.3189	-0.02617	0	3.5870	0.1598	-0.01210	4.2960	2.1160	4.4270	5.0550	[1.2, 7.8]	0.0018	0.83 %	A
	0.80	0.2740	0.5818	-0.05780	0	3.3890	0.2536	-0.01830	4.0890	2.8230	4.1430	6.3180	[0.8, 7.8]	0.0034	1.1 %	A
	0.90	0.2732	0.7895	-0.08128	0	3.4930	0.3403	-0.02647	4.1360	2.1800	4.4960	3.6180	[0.9, 7.7]	0.0044	1.2 %	A
CH_4	1.00	0.2977	0.9707	-0.1111	0	3.5540	0.3984	-0.03216	4.1770	2.0140	4.6030	3.6940	[1.0, 7.6]	0.0037	0.86 %	A
	1.10	0.2203	0.9202	-0.08778	0	3.564	0.4003	-0.03176	4.1480	1.9640	4.5990	3.9180	[1.0, 7.6]	0.0063	1.5 %	A
	1.20	0.3466	0.8733	-0.09857	0	3.458	0.3233	-0.02319	4.2070	3.2360	4.3090	7.2530	[1.1, 7.7]	0.0033	0.85 %	A
	1.30	0.2799	0.4431	-0.03139	0	4.2540	0.2263	-0.01764	4.8410	2.1700	4.8700	3.9910	[1.1, 7.8]	0.0037	1.3 %	A
	0.70	0.3760	0.5154	-0.06108	0	3.3370	0.2021	-0.01372	4.1590	2.8250	4.2030	4.2060	[1.1, 7.7]	0.0028	1.1 %	A
	0.80	0.4270	0.8622	-0.12570	0	3.4190	0.3031	-0.02148	4.1550	3.2520	4.2670	6.5400	[1.0, 7.4]	0.0035	0.98 %	A
	0.90	0.2552	0.9578	-0.10680	0	3.4900	0.4033	-0.03151	4.0480	2.9710	4.0010	8.1720	[0.9, 7.5]	0.0077	1.8 %	A
	1.00	0.3015	1.1820	-0.1450	0	3.3810	0.4282	-0.02985	4.0710	2.5520	4.3320	2.9220	[0.9, 7.4]	0.0057	1.2 %	A
C_2H_6	1.10	0.2634	1.1870	-0.1327	0	3.4420	0.4472	-0.03068	4.0830	2.4170	4.3430	2.6630	[0.8, 7.3]	0.0069	1.4 %	A
	1.20	0.2156	1.0830	-0.1054	0	3.5080	0.4414	-0.03454	3.9290	1.4660	4.5530	2.7410	[0.9, 7.3]	0.0108	2.3 %	A
	1.30	0.2148	0.8802	-0.07904	0	3.4710	0.3515	-0.02468	3.9660	1.9390	4.0900	1.8220	[0.7, 7.7]	0.0063	1.5 %	A
	1.40	0.2336	0.5957	-0.04089	0	3.5450	0.2514	-0.01678	4.2020	2.6010	4.3360	3.7720	[0.7, 7.8]	0.0051	1.6 %	A
	1.50	0.1864	0.3303	-0.01296	0	3.7660	0.1643	-0.01064	4.3670	1.9930	4.6140	4.9320	[0.7, 7.6]	0.0034	1.5 %	A

A: Bergthorson (2005b)

Table D.5: Fits to experimental velocity profiles. (cont.)

Flame		Velocity-profile-fit parameters											$[x_{\min},\ x_{\max}]$	$\epsilon_{\rm rms}$	$\epsilon_{\rm rms}/S_{\rm u,exp}$	Fits
fuel	Φ	$x_{0,\rm ph}$	$a_{1,\rm ph}$	$a_{2,\rm ph}$	$a_{3,\rm ph}$	$x_{0,\rm pc}$	$a_{1,\rm pc}$	$a_{2,\rm pc}$	$x_{0,\rm e1}$	$b_{\rm e1}$	$x_{0,\rm e2}$	$b_{\rm e2}$	(mm)			source
	0.60	0.05280	0.4155	-0.01953	0	3.4180	0.2576	-0.02145	4.0720	2.1220	4.3860	3.0050	[0.3, 7.6]	0.0026	0.85 %	A
	0.80	0.1520	0.9302	-0.08610	0	3.3380	0.4072	-0.02786	4.1440	2.3710	4.4820	3.2730	[0.5, 7.5]	0.0051	1.1 %	A
	1.00	0.1351	0.8653	-0.07620	0	3.2510	0.3692	-0.02327	4.0690	3.5270	4.0680	18.9700	[0.4, 7.5]	0.0101	2.2 %	A
C_2H_4	1.20	0.1736	0.8799	-0.08366	0	3.4730	0.3718	-0.02663	4.2300	2.3310	4.5770	3.3410	[0.5, 7.4]	0.0081	1.8 %	A
	1.40	0.1666	0.8682	-0.07211	0	3.5620	0.3724	-0.02742	4.3820	4.0540	4.5760	10.3500	[0.5, 7.4]	0.0047	1.1 %	A
	1.60	0.07875	0.8009	-0.02884	0	4.0320	0.4686	-0.04693	4.0830	1.2490	4.8850	3.5930	[0.3, 7.7]	0.0065	1.5 %	A
	1.80	0.08362	0.4190	-0.004593	0	4.3400	0.2846	-0.03056	4.2250	1.0100	5.1870	2.5670	[0.5, 7.9]	0.0031	1.1 %	A
	0.70	-0.05991	0.2513	0.05155	-0.01264	2.9689	0.1274	$-6.750\cdot10^{-7}$	4.3961	3.3389	4.5025	8.9792	[0.4, 6.8]	0.0015	0.58 %	B
	0.85	-0.05049	0.5071	0.07610	-0.02307	3.3636	0.2666	-0.008942	4.3541	3.7624	4.0365	10.0323	[0.3, 6.8]	0.0038	1.0 %	B
C_3H_8	1.00	-0.04365	0.6660	0.08260	-0.02612	3.6564	0.3856	-0.02566	4.4721	4.0651	4.1543	10.2541	[0.2, 7.2]	0.0057	1.3 %	B
	1.25	0.1403	0.7861	-0.02781	-0.008328	3.5438	0.2927	-0.009884	4.4793	4.0908	4.5884	10.8494	[0.5, 6.4]	0.0029	0.73 %	B
	1.50	0.3415	0.2761	-0.01642	$-1.636\cdot10^{-7}$	3.3824	0.08912	-0.001840	4.6662	1.8778	3.7980	2.9763	[0.7, 6.8]	0.0033	1.7 %	B
	0.70	-0.05200	0.3094	0.06777	-0.01692	3.3133	0.1920	-0.005153	4.3918	3.9568	4.4618	7.7547	[0.3, 6.5]	0.0048	1.6 %	B
	0.85	0.1361	0.8323	-0.03718	-0.009339	3.2428	0.2666	$-1.162\cdot10^{-7}$	4.3759	3.9483	4.1150	9.7252	[0.6, 6.3]	0.0046	1.1 %	B
C_3H_6	1.00	0.02080	0.7924	0.1347	-0.04289	3.5431	0.4059	-0.02116	4.5229	4.5858	3.4500	0.8439	[0.5, 7.4]	0.0089	1.8 %	B
	1.30	0.05501	0.6752	0.1187	-0.03545	3.8663	0.3788	-0.02904	4.6132	3.3806	3.3829	0.7209	[0.9, 7.1]	0.0019	0.45 %	B
	1.60	-0.6802	0.2175	-0.01427	$-1.666\cdot10^{-7}$	4.0865	0.1226	-0.01334	4.6985	1.5519	1.9278	0.3726	[0.2, 7.0]	0.0040	2.4 %	B

A: Bergthorson (2005b)

B: Present work

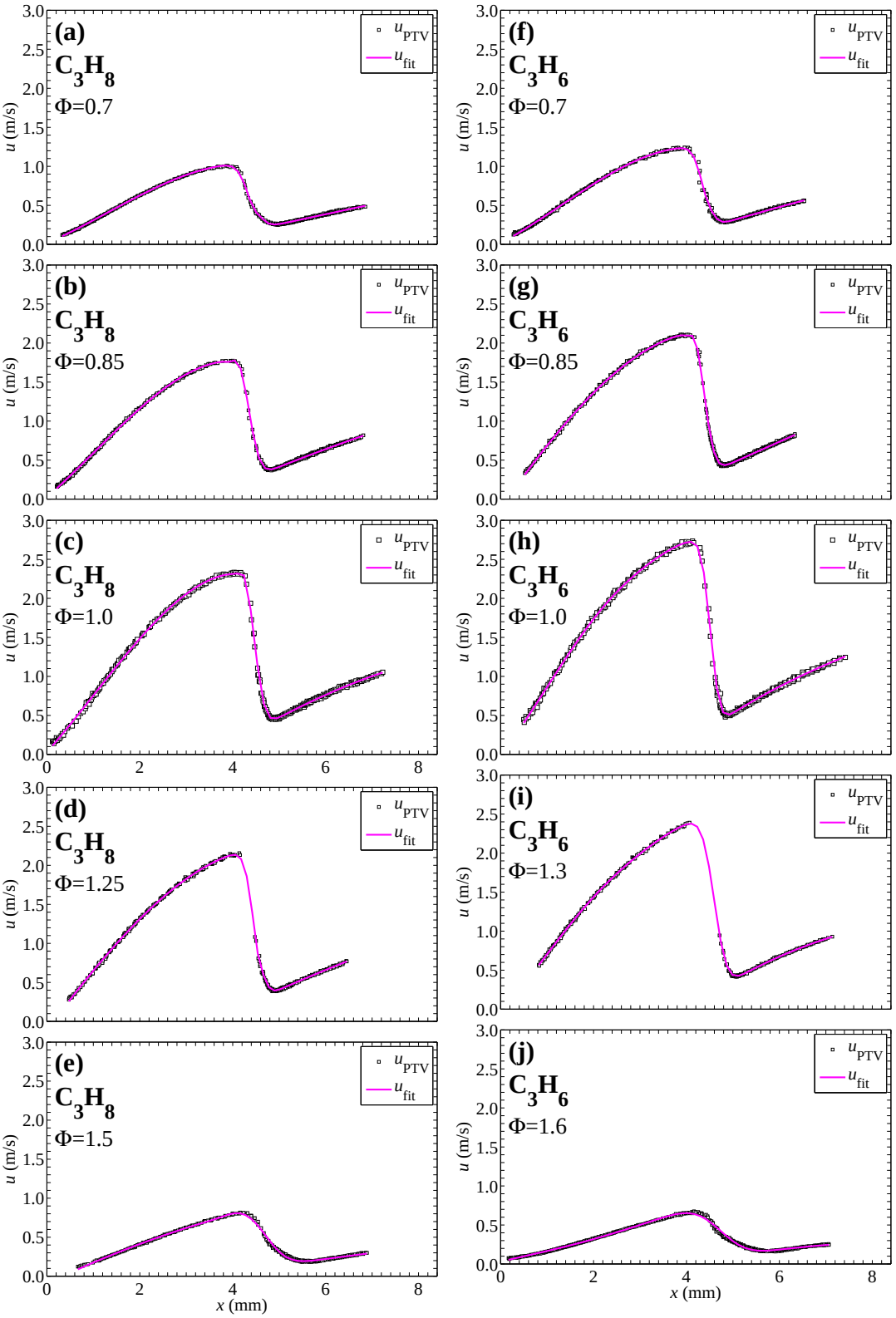

Figure D.1: C_3H_8-air (left) and C_3H_6-air (right) flame experimental velocity profiles and fits.

D.4.2 Stagnation-flame CH-PLIF profile fits

The CH-PLIF profiles are well represented by a "two-sided" Lorentzian 4-parameter fit (Bergthorson 2005a, Appendix C.1; Bergthorson 2005b). A fit is performed for each image to the average profile over the 50 central columns (around the jet axis, where the flame is flat), and the average value of each fit parameter over the 1000 PLIF images is retained. The fits from Bergthorson (2005b) to the CH-PLIF profiles for CH_4, C_2H_6, & C_2H_4 flames and the fits from the present work to the CH-PLIF profiles for C_3H_8 & C_3H_6 flames are shown in Table D.6. The analytic expression of the "two-sided" Lorentzian 4-parameter CH-PLIF-profile fit (Bergthorson 2005a, Appendix C.1) is recalled in Eq. D.6.

$$S_{\mathrm{CH}}\left(x < x_0\right) = \frac{S_{\mathrm{CH,max}}\, {w_1}^2}{(x - x_0)^2 + {w_1}^2} \quad , \quad S_{\mathrm{CH}}\left(x > x_0\right) = \frac{S_{\mathrm{CH,max}}\, {w_2}^2}{(x - x_0)^2 + {w_2}^2} \quad , \tag{D.6}$$

where $S_{\mathrm{CH,max}}$ is the peak intensity, x_0 is the peak location, and w_1 & w_2 are the widths corresponding to the half-maximum value on either side of x_0 (the full width at half maximum is w_1+w_2).

Flame		CH-PLIF-profile-fit parameters				$[x_{\min}, x_{\max}]$	Fits
fuel	Φ	$S_{\mathrm{CH,max}}$	x_0	w_1	w_2	(mm)	source
	0.70	6.59	4.10	0.188	0.188	[0, 7.5]	A
	0.80	7.79	3.93	0.122	0.122	[0, 7.5]	A
	0.90	13.7	3.96	0.104	0.104	[0, 7.5]	A
CH_4	1.00	24.3	4.03	0.097	0.097	[0, 7.5]	A
	1.10	31.5	3.97	0.0994	0.0994	[0, 7.5]	A
	1.20	34.3	3.97	0.110	0.110	[0, 7.5]	A
	1.30	27.6	4.53	0.145	0.145	[0, 7.5]	A
	0.70	1.99	3.99	0.105	0.0096	[0, 7.9]	A
	0.80	4.3	3.98	0.0977	0.0794	[0, 7.9]	A
	0.90	8.28	3.97	0.0938	0.0757	[0, 7.9]	A
	1.00	13	3.99	0.0954	0.0766	[0, 7.9]	A
C_2H_6	1.10	17.7	4.01	0.103	0.0835	[0, 7.9]	A
	1.20	20.9	3.98	0.119	0.0914	[0, 7.9]	A
	1.30	20.7	3.99	0.142	0.096	[0, 7.9]	A
	1.40	15	3.98	0.198	0.106	[0, 7.9]	A
	1.50	8.71	4.05	0.314	0.132	[0, 7.9]	A
	0.60	1.56	3.94	0.114	0.0851	[0, 7.7]	A
	0.80	9.68	4.06	0.0904	0.0692	[0, 7.7]	A
	1.00	9.07	4.01	0.0976	0.0768	[0, 7.7]	A
C_2H_4	1.20	14.4	4.08	0.112	0.0857	[0, 7.7]	A
	1.40	15	4.07	0.152	0.0867	[0, 7.7]	A
	1.60	9.76	4.11	0.248	0.0934	[0, 7.7]	A
	1.80	2.82	4.16	0.364	0.0836	[0, 7.7]	A
	0.70	16.7	4.08	0.114	0.160	[0, 11.1]	B
	0.85	67.5	4.16	0.110	0.141	[0, 11.1]	B
C_3H_8	1.00	150.1	4.29	0.116	0.128	[0, 11.1]	B
	1.25	223.6	4.20	0.139	0.137	[0, 11.1]	B
	1.50	93.1	4.21	0.294	0.158	[0, 11.1]	B
	0.70	16.1	4.05	0.110	0.167	[0, 11.1]	B
	0.85	58.4	4.20	0.107	0.127	[0, 11.1]	B
C_3H_6	1.00	117.4	4.30	0.110	0.130	[0, 11.1]	B
	1.30	188.7	4.30	0.145	0.132	[0, 11.1]	B
	1.60	54.1	4.14	0.354	0.157	[0, 11.1]	B

A: Bergthorson (2005b)
B: Present work

Table D.6: Fits to experimental CH-PLIF profiles.

Appendix E

Uncertainties

E.1 Uncertainty on predicted stagnation-flame speed and CH-peak location

All the simulation input parameters, ν_j: pressure p, equivalence ratio Φ, oxygen percentage in air $\%O_2/(O_2 + N_2)$, inlet velocity u_ℓ, inlet spreading rate V_ℓ (equal to half the inlet velocity gradient), inlet temperature T_ℓ, and wall temperature T_{wall}, have an associated uncertainty, σ_{ν_j}, due to their respective measurements. Model parameters like the hundreds of kinetic reaction-rate parameters also have associated uncertainties, but they are not considered in the simulation input parameters, ν_j. Assuming that the uncertainties σ_{ν_j} are independent, Eqs. E.1–E.4 show how these uncertainties can be propagated using the logarithmic sensitivity of the predicted CH-peak location to each parameter ν_j, $LS(x_{\text{CH,sim}})_j$, in order to estimate the uncertainty on the predicted CH-peak location, $\sigma_{x_{\text{CH,sim}}}$.

$$\sigma^2_{x_{\text{CH,sim}}} = \sum_j \left(\frac{\partial x_{\text{CH,sim}}}{\partial \nu_j} \right)^2 \sigma^2_{\nu_j} \tag{E.1}$$

$$\sigma^2_{x_{\text{CH,sim}}} \simeq \sum_j \left(\frac{x_{\text{CH,sim}}(\nu_j + \Delta\nu_j/2) - x_{\text{CH,sim}}(\nu_j - \Delta\nu_j/2)}{\Delta\nu_j} \right)^2 \sigma^2_{\nu_j} = \sum_j \left(\frac{\Delta x_{\text{CH,sim}}}{\Delta\nu_j} \right)^2 \sigma^2_{\nu_j} \tag{E.2}$$

$$\sigma^2_{x_{\text{CH,sim}}} \simeq x^2_{\text{CH,sim}} \sum_j \left(\frac{\Delta x_{\text{CH,sim}}/x_{\text{CH,sim}}}{\Delta\nu_j/\nu_j} \right)^2 \left(\frac{\sigma_{\nu_j}}{\nu_j} \right)^2 \tag{E.3}$$

$$\sigma_{x_{\text{CH,sim}}} \simeq x_{\text{CH,sim}} \sqrt{\sum_j \left(LS(x_{\text{CH,sim}})_j\right)^2 \left(\frac{\sigma_{\nu_j}}{\nu_j} \right)^2} \tag{E.4}$$

The uncertainty on the predicted stagnation flame speed, $\sigma_{S_{\text{u,sim}}}$, is estimated in the same way:

$$\sigma_{S_{\text{u,sim}}} \simeq S_{\text{u,sim}} \sqrt{\sum_j \left(LS(S_{\text{u,sim}})_j\right)^2 \left(\frac{\sigma_{\nu_j}}{\nu_j} \right)^2} \tag{E.5}$$

Table E.1 reports the relative uncertainties σ_{ν_j}/ν_j, on the simulation input parameters. The uncertainty on p was chosen as the barometric pressure deviation from 1 atm during the days when the C_3-flame experiments were performed. The relative uncertainty on Φ was deduced by propagating the 0.6 % relative uncertainty on the volumetric flux of each stream (not including the C_3H_8 and C_3H_6 purities $\geq 99.5\,\%$). One contributor to the uncertainty on $\%O_2/(O_2+N_2)$ was evaluated as the difference between the percentage of oxygen in dry air (20.95 %) and the percentage of oxygen in the "combustion air" (21 % O_2, 79 % N_2) used in the simulations. It is the only contribution for the C_3-flame experiments considered here since these flames were not diluted; the oxidizer was industrial-grade compressed air. The 0.6 % relative uncertainty on the volumetric flux of each stream must also be taken into account if the oxidizer used in the experiments was a binary mixture (air & N_2, or O_2 & N_2, for example) mixed in our lab, which, alone, would correspond to a 0.7 % relative uncertainty on $\%O_2/(O_2+N_2)$. From the parabola fitted to the measured velocity profile in the cold region (upstream of the flame), the 95 % confidence interval bounds on the velocity-fit values are obtained. The uncertainty on u_ℓ is the half-width of the confidence interval evaluated at the inlet, ℓ. As in Bergthorson 2005a, Section 2.6, two parabolas are fit through the max bound at the start of the fit domain, the fit value at ℓ, & the min bound at the end of the fit domain, and through the min bound at the start of the fit domain, the fit value at ℓ, & the max bound at the end of the fit domain, respectively. The average difference between the slope of each of these two parabolas and the slope of the optimal fit at ℓ indicate a maximum uncertainty on the velocity gradient at ℓ. The relative uncertainty on V_ℓ is the same as the relative uncertainty on the velocity gradient at ℓ. σ_V/V is especially large for the richest C_3H_8 and C_3H_6 flames (see Table E.1) because the inlet was chosen too close to the edge of the velocity data points in these flames and because of the method used to estimate the uncertainty in V. The uncertainty on T_ℓ is deduced from the common accuracy of 1 K for K-type thermocouples and from the (negligible) 0.005 % relative standard deviation of the measurements during the experiment. The uncertainty on T_{wall} is deduced from the relative variation of the stagnation-plate temperature between the beginning and the end of the experiment due to the slight imbalance between heating from the flame and passive water cooling, and from the common accuracy of 1 K for K-type thermocouples.

Figures E.1a & E.1b and E.2a & E.2b show the logarithmic sensitivities $LS(S_{\text{u,sim}})_j$ and $LS(x_{\text{CH,sim}})_j$ of the predicted stagnation flame speed and CH-peak location to each simulation input parameter ν_j for all the C_3 flames investigated. The logarithmic sensitivities are calculated using a centered-difference scheme (see Eq. E.2), with logarithmic increases $\Delta\log\nu_j = \frac{\Delta\nu_j}{\nu_j}$ equal to 1 % for every simulation input parameter except T_{wall}, for which a 10 % logarithmic increase was used, given the weak influence of T_{wall} on S_{u} and x_{CH}. Simulations with a frozen ~ 400 points grid were used since erratic variations of S_{u} and x_{CH} due to numerical errors were present at lower resolutions when simulating flames with slightly different values of T_{wall}, and the mixture-averaged molecular

Flame fuel	Φ		Pressure	Inlet BC					Stagnation-plate BC
		ν_j	P	Φ	$\%O_2/(O_2+N_2)$	u_ℓ	V_ℓ	T_ℓ	T_{wall}
	0.70	$\frac{\sigma_{\nu_j}}{\nu_j}$	$+0.2\,\%$	$\pm 0.8\,\%$	$+0.2\,\%$	$\pm 0.5\,\%$	$\pm 4.0\,\%$	$\pm 0.3\,\%$	$\pm 0.3\,\%$
	0.85	$\frac{\sigma_{\nu_j}}{\nu_j}$	$+0.2\,\%$	$\pm 0.8\,\%$	$+0.2\,\%$	$\pm 0.3\,\%$	$\pm 2.7\,\%$	$\pm 0.3\,\%$	$\pm 0.9\,\%$
C_3H_8	1.00	$\frac{\sigma_{\nu_j}}{\nu_j}$	$+0.2\,\%$	$\pm 0.8\,\%$	$+0.2\,\%$	$\pm 0.4\,\%$	$\pm 2.5\,\%$	$\pm 0.3\,\%$	$\pm 1.0\,\%$
	1.25	$\frac{\sigma_{\nu_j}}{\nu_j}$	$+0.2\,\%$	$\pm 0.8\,\%$	$+0.2\,\%$	$\pm 0.6\,\%$	$\pm 3.5\,\%$	$\pm 0.3\,\%$	$\pm 0.7\,\%$
	1.50	$\frac{\sigma_{\nu_j}}{\nu_j}$	$+0.2\,\%$	$\pm 0.8\,\%$	$+0.2\,\%$	$\pm 1.2\,\%$	$\pm 11.3\,\%$	$\pm 0.3\,\%$	$\pm 0.3\,\%$
	0.70	$\frac{\sigma_{\nu_j}}{\nu_j}$	$+0.2\,\%$	$\pm 0.8\,\%$	$+0.2\,\%$	$\pm 0.6\,\%$	$\pm 3.7\,\%$	$\pm 0.3\,\%$	$\pm 0.4\,\%$
	0.85	$\frac{\sigma_{\nu_j}}{\nu_j}$	$+0.2\,\%$	$\pm 0.8\,\%$	$+0.2\,\%$	$\pm 0.4\,\%$	$\pm 3.3\,\%$	$\pm 0.3\,\%$	$\pm 1.0\,\%$
C_3H_6	1.00	$\frac{\sigma_{\nu_j}}{\nu_j}$	$+0.2\,\%$	$\pm 0.8\,\%$	$+0.2\,\%$	$\pm 0.4\,\%$	$\pm 2.9\,\%$	$\pm 0.3\,\%$	$\pm 2.1\,\%$
	1.30	$\frac{\sigma_{\nu_j}}{\nu_j}$	$+0.2\,\%$	$\pm 0.8\,\%$	$+0.2\,\%$	$\pm 0.5\,\%$	$\pm 2.5\,\%$	$\pm 0.3\,\%$	$\pm 0.9\,\%$
	1.60	$\frac{\sigma_{\nu_j}}{\nu_j}$	$+0.2\,\%$	$\pm 0.8\,\%$	$+0.2\,\%$	$\pm 1.5\,\%$	$\pm 10.9\,\%$	$\pm 0.3\,\%$	$\pm 0.3\,\%$

Table E.1: Uncertainties on simulation input parameters.

transport model was used to save computing time. S_{u} and x_{CH} are most sensitive to the composition of the premixed combustible mixture, especially far from stoichiometric conditions.

Table E.2 shows the resulting uncertainties on the predicted stagnation flame speed, $\sigma_{S_{\text{u,sim}}}$ (see Eq. E.5), and CH-peak location, $\sigma_{x_{\text{CH,sim}}}$ (see Eq. E.4), scaled consistently with the comparisons shown in Fig. 5.6, for all the C_3 flames investigated. For both fuels, $\sigma_{x_{\text{CH,sim}}} \simeq 20$–$45\,\% \, \delta_{\text{CH,S5},\Phi=1}$ under moderately lean, stoichiometric, and moderately rich conditions, $\sigma_{x_{\text{CH,sim}}} \simeq 65\,\% \, \delta_{\text{CH,S5},\Phi=1}$ under very lean conditions, and $\sigma_{x_{\text{CH,sim}}} \simeq 125$–$145\,\% \, \delta_{\text{CH,S5},\Phi=1}$ under very rich conditions. The larger uncertainties under very lean and very rich conditions are due to the larger sensitivity of the solution (see Figs. E.2a and E.2b). The larger uncertainty under very rich conditions is also due to a larger uncertainty on the inlet spreading rate, because there were not enough velocity data points between the starting point of the cold parabolic fit (used to determine the inlet velocity and velocity gradient) and the inlet.

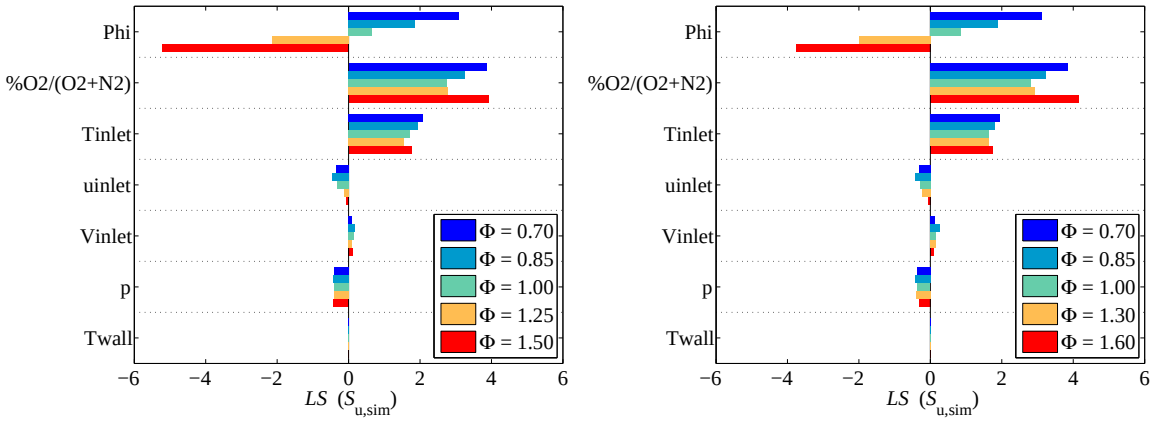

(a) C_3H_8 flames (b) C_3H_6 flames

Figure E.1: Sensitivity of predicted stagnation-flame speed to simulation input parameters.

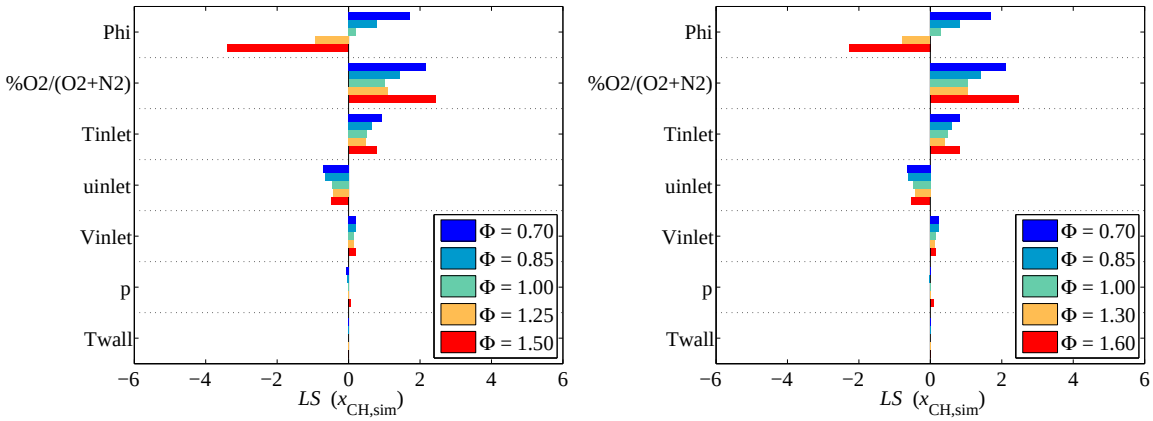

(a) C_3H_8 flames (b) C_3H_6 flames

Figure E.2: Sensitivity of predicted CH-peak location to simulation input parameters.

Flame		$\frac{\sigma_{S_{\mathrm{u,sim}}}}{S_{\mathrm{u,exp}}}$	$\frac{\sigma_{x_{\mathrm{CH,sim}}}}{\delta_{\mathrm{CH,S5},\Phi=1}}$	$\frac{\sigma_{S_{\mathrm{u,exp}}}}{S_{\mathrm{u,exp}}}$	$\frac{\sigma_{x_{\mathrm{CH,exp}}}}{x_{\mathrm{CH,exp}}}$	$\frac{\sigma_{x_{\mathrm{CH,exp}}}}{\delta_{\mathrm{CH,S5},\Phi=1}}$
fuel	Φ					
C_3H_8	0.70	2.7 %	67 %	1.4 %	0.16 %	6.3 %
	0.85	1.8 %	38 %	1.6 %	0.05 %	1.8 %
	1.00	1.0 %	21 %	1.2 %	0.04 %	1.5 %
	1.25	1.9 %	39 %	1.2 %	0.03 %	1.0 %
	1.50	4.5 %	142 %	2.4 %	0.07 %	2.7 %
C_3H_6	0.70	2.3 %	64 %	2.1 %	0.14 %	5.9 %
	0.85	1.7 %	44 %	1.3 %	0.05 %	2.0 %
	1.00	1.1 %	27 %	2.0 %	0.04 %	1.7 %
	1.30	1.8 %	34 %	1.6 %	0.04 %	1.5 %
	1.60	3.9 %	124 %	2.4 %	0.20 %	8.0 %

Table E.2: Uncertainties on predicted and measured stagnation-flame speed and CH-peak location.

E.2 Uncertainty on measured stagnation-flame speed and CH-peak location

Table E.2 reports the uncertainties on the stagnation flame speed measured by PTV and on the CH-peak location measured by CH-PLIF.

The uncertainty on the PTV velocities is taken as the root-mean-squared (rms) difference between the measured velocity profile and the corresponding fitted profile (see Section D.4.1), and is scaled by the stagnation flame speed (see Table D.5). The uncertainty on the measured stagnation flame speed, $\sigma_{S_{\mathrm{u,exp}}}$, is determined from the half-width of the 95 % confidence interval on the cubic fit (fitted to the portion of the velocity profile around the minimum-velocity point, upstream of the flame) value at the minimum-velocity point.

The uncertainty on the measured CH-peak location, $\sigma_{x_{\mathrm{CH,exp}}}$, is determined from the half-width of the 95 % confidence interval on the value at the center (corresponding to the jet axis) of the parabola fitted to the two-dimensional CH-PLIF data (see Section D.3). $\sigma_{x_{\mathrm{CH,exp}}}$ is larger under very lean conditions and in the $\Phi = 1.6$ C_3H_6 flame (richer than the $\Phi = 1.5$ C_3H_8 flame), where the signal-to-noise ratio is poor (see Figs. B.1a, B.1f, and B.1j).

The relative uncertainty on $x_{\mathrm{CH,exp}}$ is one order of magnitude smaller than the relative uncertainty on $S_{\mathrm{u,exp}}$. The scaled uncertainty on the measured CH-peak location, $\sigma_{x_{\mathrm{CH,exp}}} / \delta_{\mathrm{CH,S5},\Phi=1}$ in Table E.2 is clearly smaller than the scaled uncertainty on the predicted CH-peak location in Table E.2.

E.3 Total uncertainty on the comparisons of predicted and measured stagnation-flame speed and CH-peak location

The predicted & measured values of stagnation flame speed and CH-peak location are compared by plotting $\widetilde{dS}_{\rm u} = (S_{\rm u,sim} - S_{\rm u,exp}) / S_{\rm u,exp}$ and $\widetilde{dx}_{\rm CH} = (x_{\rm CH,sim} - x_{\rm CH,exp}) / \delta_{\rm CH,S5,\Phi=1}$, respectively (see Fig. 5.6). It is reasonable to assume that the uncertainties on $S_{\rm u,sim}$ & $S_{\rm u,exp}$ are independent, as well as the uncertainties on $x_{\rm CH,sim}$ & $x_{\rm CH,exp}$. As a result, the total uncertainties, $\Sigma_{\rm exp}$, on the comparison of predicted and measured values due to experimental measurement uncertainties are:

$$\Sigma^2_{{\rm exp},\widetilde{dx}_{\rm CH}}(mech) = \left(\frac{\partial \widetilde{dx}_{\rm CH}}{\partial x_{\rm CH,sim}}\right)^2 \sigma^2_{x_{\rm CH,sim}} + \left(\frac{\partial \widetilde{dx}_{\rm CH}}{\partial x_{\rm CH,exp}}\right)^2 \sigma^2_{x_{\rm CH,exp}} \quad \text{(E.6)}$$

$$\Sigma_{{\rm exp},\widetilde{dx}_{\rm CH}}(mech) = \frac{1}{\delta_{\rm CH,S5,\Phi=1}} \sqrt{\sigma^2_{x_{\rm CH,sim}} + \sigma^2_{x_{\rm CH,exp}}} \quad \text{(E.7)}$$

$$\Sigma_{{\rm exp},\widetilde{dx}_{\rm CH}}(mech) \simeq \frac{1}{\delta_{\rm CH,S5,\Phi=1}} \sqrt{x^2_{\rm CH,sim}(mech) \cdot \left(\frac{\sigma_{x_{\rm CH,sim}}}{x_{\rm CH,sim}}\right)^2 + \sigma^2_{x_{\rm CH,exp}}} \quad \text{(E.8)}$$

$$\Sigma_{{\rm exp},\widetilde{dx}_{\rm CH}} \simeq \max_{\rm mechs\,DLW,S5,BL,KON}\left(\Sigma_{{\rm exp},\widetilde{dx}_{\rm CH}}(mech)\right) \quad \text{(E.9)}$$

and

$$\Sigma^2_{{\rm exp},\widetilde{dS}_{\rm u}}(mech) = \left(\frac{\partial \widetilde{dS}_{\rm u}}{\partial S_{\rm u,sim}}\right)^2 \sigma^2_{S_{\rm u,sim}} + \left(\frac{\partial \widetilde{dS}_{\rm u}}{\partial S_{\rm u,exp}}\right)^2 \sigma^2_{S_{\rm u,exp}} \quad \text{(E.10)}$$

$$\Sigma_{{\rm exp},\widetilde{dS}_{\rm u}}(mech) \simeq S_{\rm u,sim}(mech) \cdot \frac{1}{S_{\rm u,exp}} \sqrt{\left(\frac{\sigma_{S_{\rm u,sim}}}{S_{\rm u,sim}}\right)^2 + \left(\frac{\sigma_{S_{\rm u,exp}}}{S_{\rm u,exp}}\right)^2} \quad \text{(E.11)}$$

$$\Sigma_{{\rm exp},\widetilde{dS}_{\rm u}} \simeq \max_{\rm mechs\,DLW,S5,BL,KON}\left(\Sigma_{{\rm exp},\widetilde{dS}_{\rm u}}(mech)\right) \quad . \quad \text{(E.12)}$$

The relative uncertainties on $S_{\rm u,sim}$ & $x_{\rm CH,sim}$ only depend (see Eq. E.4) on the uncertainties on the simulation input parameters that are independent of the mechanism used for the simulation, and on the sensitivity of the solution to the simulation input parameters, which was evaluated using a specific mechanism: S5. These sensitivities should be very similar when using different mechanisms. Therefore, the relative uncertainties on $S_{\rm u,sim}$ and $x_{\rm CH,sim}$ should be very similar when using different mechanisms. However, $\Sigma_{{\rm exp},\widetilde{dx}_{\rm CH}}(mech)$ and $\Sigma_{{\rm exp},\widetilde{dS}_{\rm u}}(mech)$ keep a small dependence on the mechanism via $S_{\rm u,sim}$ and $x_{\rm CH,sim}$ that are at variance among the different mechanisms. Table E.3 shows the values of $\Sigma_{\rm exp}$ for the different mechanisms and flames investigated. The values of $\Sigma_{\rm exp}$ plotted in Fig. 5.6 are the largest $\Sigma_{\rm exp}$ among all mechanisms used but G3 (included for reference only), as shown in Eqs. E.9 and E.12.

Finally, it is essential to note that the uncertainties associated with each model are not considered here. Analyses of the uncertainty on the thermodynamic, molecular transport, and more importantly kinetic model parameters such as the study conducted by Zádor et al. (2005) are needed to close the

discussion on the uncertainties by adding a specific uncertainty band for each model curve shown in Fig. 5.6.

Mechanism		G3	DLW	S5	BL	KON
Flame fuel	Φ	$\Sigma_{\exp,\widetilde{dS}_u}$	$\Sigma_{\exp,\widetilde{dS}_u}$	$\Sigma_{\exp,\widetilde{dS}_u}$	$\Sigma_{\exp,\widetilde{dS}_u}$	$\Sigma_{\exp,\widetilde{dS}_u}$
C_3H_8	0.70	4.2 %	3.1 %	3.5 %	3.7 %	3.5 %
	0.85	3.5 %	2.8 %	2.9 %	3.1 %	3.1 %
	1.00	2.6 %	2.2 %	2.1 %	2.3 %	2.4 %
	1.25	3.8 %	3.2 %	2.9 %	3.2 %	3.2 %
	1.50	8.2 %	6.7 %	5.9 %	6.6 %	7.2 %
C_3H_6	0.70	-	3.4 %	3.6 %	4.4 %	4.3 %
	0.85	-	2.8 %	2.8 %	3.3 %	3.5 %
	1.00	-	5.4 %	5.3 %	6.1 %	6.2 %
	1.30	-	2.9 %	2.8 %	3.2 %	3.2 %
	1.60	-	5.3 %	5.2 %	5.6 %	6.3 %

Flame fuel	Φ	$\Sigma_{\exp,\widetilde{dx}_{CH}}$	$\Sigma_{\exp,\widetilde{dx}_{CH}}$	$\Sigma_{\exp,\widetilde{dx}_{CH}}$	$\Sigma_{\exp,\widetilde{dx}_{CH}}$	$\Sigma_{\exp,\widetilde{dx}_{CH}}$
C_3H_8	0.70	76 %	62 %	67 %	71 %	69 %
	0.85	42 %	38 %	38 %	40 %	40 %
	1.00	23 %	21 %	21 %	21 %	22 %
	1.25	45 %	41 %	39 %	41 %	42 %
	1.50	183 %	159 %	142 %	155 %	166 %
C_3H_6	0.70	-	61 %	64 %	72 %	71 %
	0.85	-	44 %	44 %	47 %	48 %
	1.00	-	27 %	27 %	29 %	29 %
	1.30	-	35 %	34 %	37 %	36 %
	1.60	-	126 %	124 %	130 %	143 %

Table E.3: Weak dependence on mechanism of the total uncertainty on comparisons of predicted & measured stagnation-flame speed and CH-peak location. (C_3H_6 is not present in G3.)

Appendix F

High-repetition-rate Nd:YLF pulsed velocimetry laser

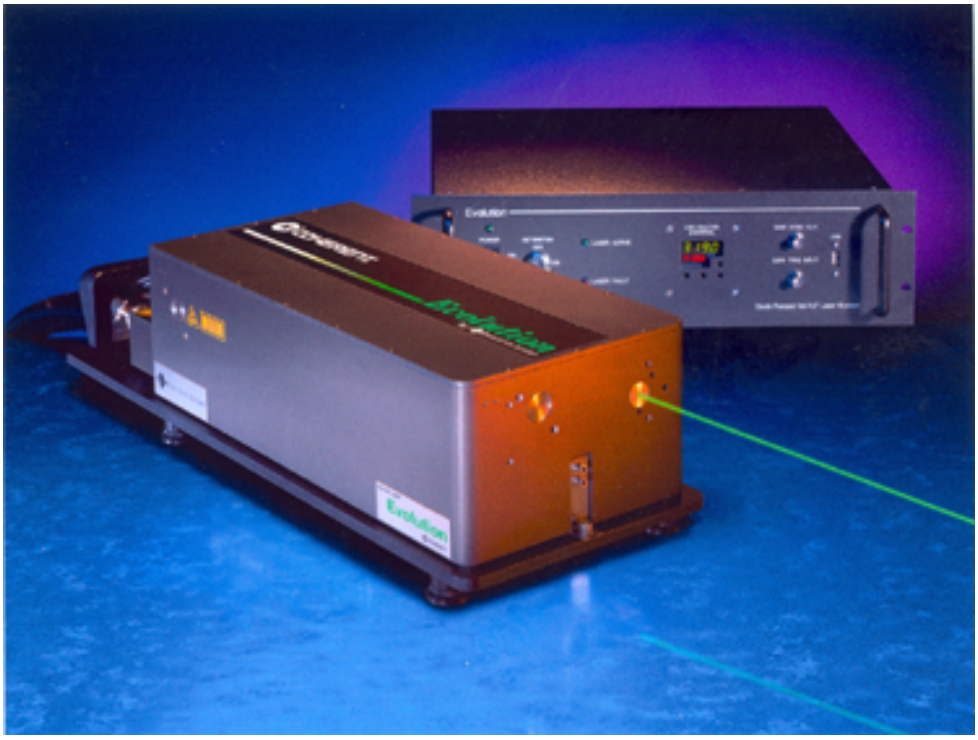

Figure F.1: Coherent Evolution-90 laser.

F.1 Introduction

As explained in Section A.1, the key upgrade in the velocimetry technique that enables investigations of faster flames and permits overall more accurate measurements is the use of a high-power, high-repetition-rate, laser: the Coherent laser Evolution-90. The Coherent Evolution-90 is a 97 W,

527 nm, diode-pumped solid-state, intra-cavity doubled, Q-switched, Nd:YLF pulsed laser able to operate at repetition rates, $\nu_{\rm p} = 1$–$20\,{\rm kHz}$, with an energy stability $< 1\,\%\,{\rm rms}$. The lower thermal birefringence and longer upper-state lifetime ($470\,\mu{\rm s}$, enabling greater energy storage) of Nd:YLF make it superior to Nd:YAG when operating at repetition rates of the order of the kHz. Moreover, diode pumping presents several advantages compared with lamps: higher power efficiency, longer lifetime (10000 hours versus ~ 500 for lamps), and lower power & cooling requirements. The double purpose of this appendix is:

- to document the results of our testing of the Coherent Evolution-90 laser used in our lab.
- to provide additional knowledge of essential features of the laser overlooked in the manual, and subsequent practical advice on how to use the laser safely.

F.2 Laser testing

The laser was tested shortly after arrival in March 2006. A Spiricon Cohu-6400 632×480 pixels^2 ($1\,{\rm pix} = 0.0099\,{\rm mm}$) camera was used to analyze the laser beam at three different stations, 1, 2, and 3, located at x_1 very close to the laser-ouput port, $x_2 = x_1 + 27\,{\rm inches}$, and $x_3 = x_1 + 46\,{\rm inches}$. At each station, the laser beam was analyzed at repetition rates, $\nu_{\rm p} = 1\,{\rm kHz}$ and $10\,{\rm kHz}$, at low power ($P = 10.2\,{\rm W}$) and at high power ($P = 97\,{\rm W}$ at $10\,{\rm kHz}$, but only $P = 20\,{\rm W}$ at $1\,{\rm kHz}$ because optical damage is possible above $20\,{\rm mJ/pulse}$). Figure F.2 shows the laser-beam images and Fig. F.3 shows the corresponding raw statistics.

The **beam diameter**, $\rm d_{beam}$, measured value is 5.4–5.5 mm (the advertised nominal beam-diameter value was 4-5 mm).

The **beam divergence**, θ, was calculated as follows:

$$\begin{aligned} \theta \;&=\; \text{Average of } \Big\{ \text{ 2 Atan } \big(\, (d_{{\rm beam},i} - d_{{\rm beam},j})/2 \;/\; (x_i - x_j) \, \big) \Big\} \\ &\quad\; \text{over the three different pairs of stations } (i,j) \text{ and} \\ &\quad\; \text{over the range of repetition rates and powers tested} \\ &\simeq\; 0.4 \;\pm\; 0.2\,{\rm mrad} \quad . \end{aligned} \tag{F.1}$$

This measured value is below the advertised specification of 4.5–7.5 mrad. Our measurement method was probably not the best, but the important answer is that the beam does not diverge by a large amount.

The **pointing stability** for changes in repetition rate and/or power was estimated to be $\simeq 10\,\%\,{\rm d_{beam}}$ (smaller than the advertised value of $\simeq 20\,\%\,{\rm d_{beam}}$), and the pulse-to-pulse pointing stability over a period of one minute at any given power and repetition rate was estimated to be $\simeq 0.01\,\%\,{\rm d_{beam}}$ (advertised value of $\simeq 10\,\%\,{\rm d_{beam}}$ over a period of an hour).

The **pulse separation uncertainty (timing jitter)** needs be small given that the velocity estimate directly depends on the output-pulses repetition rate (see Section A.1). Its advertised value was $< 50\,\text{ns}$ at any given power and repetition rate. The pulse separation uncertainty depends on the quality of the laser **Q-switch triggering**. There are two different ways to trigger the Q-switch: internal triggering (that relies on the laser timing unit) and external triggering. I would advise using external triggering via a reliable, low timing jitter signal generator such as the Berkeley-Nucleonics Model-565 that probably has a superior performance than the laser timing unit. The timing jitter of the Berkeley-Nucleonics Model-565 is $\simeq 500\,\text{ps}$, which is negligible compared to the repetition rates and pulse widths involved to trigger the Q-switch: 1-20 kHz and $\simeq 5\,\mu\text{s}$. Indeed, during the laser testing, when the Q-switch was internally triggered, repetition rates were found systematically 10% smaller than expected, and the cause was found: the Q-switch driver clock was 24.6 MHz instead of 27 MHz. The Q-switch driver was replaced, which fixed this issue.

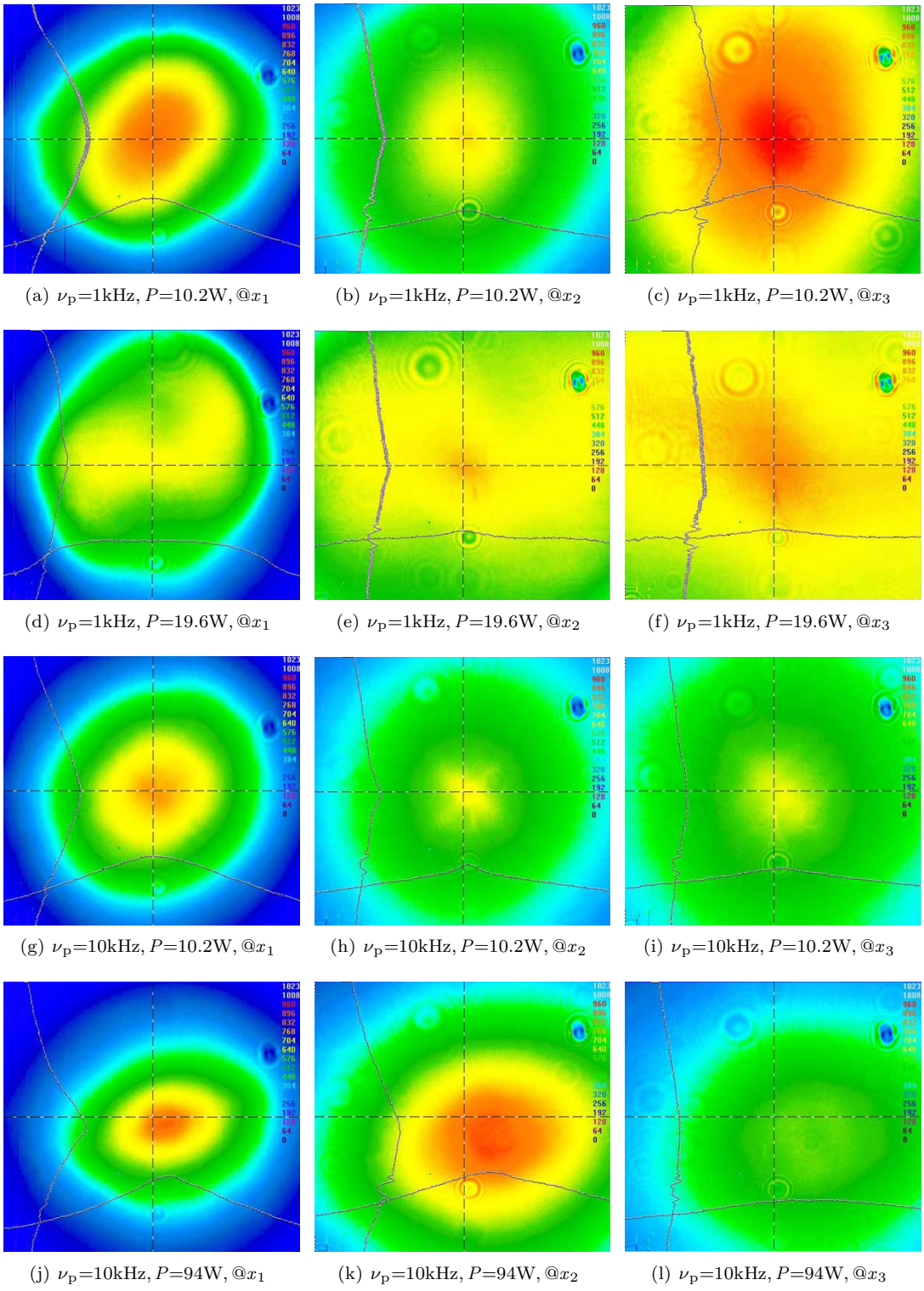

(a) ν_{p}=1kHz, P=10.2W, @x_1 (b) ν_{p}=1kHz, P=10.2W, @x_2 (c) ν_{p}=1kHz, P=10.2W, @x_3

(d) ν_{p}=1kHz, P=19.6W, @x_1 (e) ν_{p}=1kHz, P=19.6W, @x_2 (f) ν_{p}=1kHz, P=19.6W, @x_3

(g) ν_{p}=10kHz, P=10.2W, @x_1 (h) ν_{p}=10kHz, P=10.2W, @x_2 (i) ν_{p}=10kHz, P=10.2W, @x_3

(j) ν_{p}=10kHz, P=94W, @x_1 (k) ν_{p}=10kHz, P=94W, @x_2 (l) ν_{p}=10kHz, P=94W, @x_3

Figure F.2: Comparison of the laser-beam quality at different repetition rates, powers, and stations.

	Current	Mean	Deviation	Minimum	Maximum	Units
–Statistics–						
Samples	128	128	128	128	128	
–Quantitative– 90/10 Knife Edge						
Total	108,510,637	108,780,538	774,401	108,127,434	109,916,454	
% in Aperture	86.52	86.62	.7	86.50	86.72	%
Peak	9.060e+02	9.067e+02	6.326e+00	8.700e+02	9.140e+02	
Min	1.930e+02	1.924e+02	1.130e+00	1.890e+02	1.950e+02	
Peak Loc X	2.490e+02	2.512e+02	2.842e+00	2.420e+02	2.620e+02	PX
Peak Loc Y	2.390e+02	2.370e+02	5.223e+00	2.270e+02	2.520e+02	PX
Centroid X	2.569e+02	2.570e+02	6.987e-02	2.568e+02	2.573e+02	PX
Centroid Y	2.371e+02	2.387e+02	9.616e-01	2.352e+02	2.421e+02	PX
Width X	5.608e+02	5.605e+02	6.153e-01	5.595e+02	5.612e+02	PX
Width Y	5.248e+02	5.235e+02	1.371e+00	5.215e+02	5.293e+02	PX
Diameter	5.428e+02	5.420e+02	8.777e-01	5.406e+02	5.451e+02	PX

(a) ν_{p}=1kHz, P=10.2W, @x_1

	Current	Mean	Deviation	Minimum	Maximum	Units
–Statistics–						
Samples	256	256	256	256	256	
–Quantitative– 90/10 Knife Edge						
Total	121,257,063	122,001,420	961,177	121,071,357	123,390,340	
% in Aperture	86.67	86.68	.10	86.50	86.87	%
Peak	7.540e+02	7.538e+02	3.033e+00	7.390e+02	7.600e+02	
Min	2.380e+02	2.409e+02	3.258e+00	2.340e+02	2.540e+02	
Peak Loc X	2.590e+02	2.611e+02	3.151e+00	2.520e+02	2.670e+02	PX
Peak Loc Y	2.390e+02	2.379e+02	2.997e+00	2.320e+02	2.460e+02	PX
Centroid X	2.572e+02	2.572e+02	1.284e-01	2.569e+02	2.576e+02	PX
Centroid Y	2.355e+02	2.358e+02	8.944e-01	2.328e+02	2.390e+02	PX
Width X	6.037e+02	6.036e+02	2.520e-01	6.030e+02	6.041e+02	PX
Width Y	5.765e+02	5.764e+02	3.927e-01	5.755e+02	5.779e+02	PX
Diameter	5.901e+02	5.900e+02	2.762e-01	5.893e+02	5.909e+02	PX

(b) ν_{p}=1kHz, P=10.2W, @x_2

	Current	Mean	Deviation	Minimum	Maximum	Units
–Statistics–						
Samples	256	256	256	256	256	
–Quantitative– 90/10 Knife Edge						
Total	177,290,624	175,148,413	1,713,612	173,279,640	177,432,917	
% in Aperture	86.76	86.65	.7	86.50	86.79	%
Peak	1.011e+03	1.007e+03	3.006e+00	9.890e+02	1.014e+03	
Min	2.920e+02	2.913e+02	2.857e+00	2.840e+02	2.980e+02	
Peak Loc X	2.670e+02	2.646e+02	3.188e+00	2.560e+02	2.720e+02	PX
Peak Loc Y	2.360e+02	2.342e+02	5.502e+00	2.270e+02	2.780e+02	PX
Centroid X	2.585e+02	2.583e+02	2.034e-01	2.577e+02	2.589e+02	PX
Centroid Y	2.335e+02	2.334e+02	1.095e+00	2.297e+02	2.374e+02	PX
Width X	6.080e+02	6.083e+02	1.967e-01	6.079e+02	6.087e+02	PX
Width Y	5.818e+02	5.820e+02	3.648e-01	5.808e+02	5.833e+02	PX
Diameter	5.949e+02	5.951e+02	2.340e-01	5.944e+02	5.959e+02	PX

(c) ν_{p}=1kHz, P=10.2W, @x_3

	Current	Mean	Deviation	Minimum	Maximum	Units
–Statistics–						
Samples	256	256	256	256	256	
–Quantitative– 90/10 Knife Edge						
Total	107,861,773	106,859,128	758,409	106,172,423	107,942,428	
% in Aperture	86.61	86.58	.4	86.50	86.67	%
Peak	6.860e+02	6.895e+02	4.101e+00	6.700e+02	6.970e+02	
Min	1.930e+02	1.927e+02	1.202e+00	1.880e+02	1.960e+02	
Peak Loc X	2.110e+02	2.226e+02	1.972e+01	1.680e+02	2.490e+02	PX
Peak Loc Y	2.240e+02	2.295e+02	3.055e+00	2.230e+02	2.430e+02	PX
Centroid X	2.600e+02	2.600e+02	1.053e-01	2.597e+02	2.604e+02	PX
Centroid Y	2.311e+02	2.311e+02	6.055e-01	2.290e+02	2.336e+02	PX
Width X	5.534e+02	5.539e+02	6.930e-01	5.524e+02	5.550e+02	PX
Width Y	5.488e+02	5.497e+02	8.456e-01	5.486e+02	5.532e+02	PX
Diameter	5.511e+02	5.518e+02	6.715e-01	5.507e+02	5.540e+02	PX

(d) ν_{p}=1kHz, P=19.6W, @x_1

	Current	Mean	Deviation	Minimum	Maximum	Units
–Statistics–						
Samples	256	256	256	256	256	
–Quantitative– 90/10 Knife Edge						
Total	153,996,645	154,953,906	1,441,745	153,010,600	157,783,116	
% in Aperture	86.57	86.67	.10	86.50	86.85	%
Peak	8.730e+02	8.692e+02	5.564e+00	8.480e+02	8.800e+02	
Min	2.820e+02	2.838e+02	3.755e+00	2.730e+02	2.970e+02	
Peak Loc X	4.700e+02	4.700e+02	1.243e-01	4.690e+02	4.700e+02	PX
Peak Loc Y	8.600e+01	8.603e+01	6.883e-01	8.500e+01	8.800e+01	PX
Centroid X	2.707e+02	2.704e+02	3.699e-01	2.686e+02	2.725e+02	PX
Centroid Y	2.206e+02	2.201e+02	1.944e+00	2.146e+02	2.280e+02	PX
Width X	6.316e+02	6.319e+02	2.968e-01	6.309e+02	6.330e+02	PX
Width Y	5.823e+02	5.823e+02	4.519e-01	5.810e+02	5.840e+02	PX
Diameter	6.070e+02	6.071e+02	3.190e-01	6.060e+02	6.081e+02	PX

(e) ν_{p}=1kHz, P=19.6W, @x_2

	Current	Mean	Deviation	Minimum	Maximum	Units
–Statistics–						
Samples	256	256	256	256	256	
–Quantitative– 90/10 Knife Edge						
Total	169,576,431	171,070,400	1,699,710	168,389,161	174,560,372	
% in Aperture	86.56	86.73	.15	86.50	87.04	%
Peak	9.090e+02	9.084e+02	5.886e+00	8.870e+02	9.250e+02	
Min	2.850e+02	2.902e+02	3.030e+00	2.820e+02	2.980e+02	
Peak Loc X	4.630e+02	4.639e+02	3.562e-01	4.630e+02	4.640e+02	PX
Peak Loc Y	8.900e+01	8.875e+01	7.289e-01	8.700e+01	9.100e+01	PX
Centroid X	2.652e+02	2.651e+02	8.670e-01	2.630e+02	2.686e+02	PX
Centroid Y	2.195e+02	2.208e+02	3.116e+00	2.107e+02	2.327e+02	PX
Width X	6.359e+02	6.358e+02	1.705e-01	6.352e+02	6.363e+02	PX
Width Y	5.872e+02	5.872e+02	3.711e-01	5.857e+02	5.888e+02	PX
Diameter	6.116e+02	6.115e+02	2.189e-01	6.106e+02	6.123e+02	PX

(f) ν_{p}=1kHz, P=19.6W, @x_3

Figure F.3: Raw statistics corresponding to the laser-beam images shown in Fig. F.2.

	Current	Mean	Deviation	Minimum	Maximum	Units
—Statistics—						
Samples	256	256	256	256	256	
—Quantitative—90/10 Knife Edge—						
Total	102,498,388	102,506,674	48,744	102,374,091	102,603,413	
% in Aperture	86.55	86.58	.3	86.50	86.72	%
Peak	8.010e+02	8.025e+02	2.099e+00	7.960e+02	8.080e+02	
Min	1.910e+02	1.926e+02	1.261e+00	1.890e+02	1.950e+02	
Peak Loc X	2.510e+02	2.638e+02	6.429e+00	2.420e+02	2.720e+02	PX
Peak Loc Y	2.360e+02	2.477e+02	5.515e+00	2.310e+02	2.560e+02	PX
Centroid X	2.612e+02	2.611e+02	1.551e-01	2.608e+02	2.614e+02	PX
Centroid Y	2.419e+02	2.420e+02	2.940e-01	2.413e+02	2.426e+02	PX
Width X	5.616e+02	5.616e+02	1.526e-01	5.612e+02	5.618e+02	PX
Width Y	5.400e+02	5.401e+02	3.082e-01	5.394e+02	5.408e+02	PX
Diameter	5.508e+02	5.509e+02	1.900e-01	5.504e+02	5.513e+02	PX

(g) ν_{p}=10kHz, P=10.2W, @x_1

	Current	Mean	Deviation	Minimum	Maximum	Units
—Statistics—						
Samples	256	256	256	256	256	
—Quantitative—90/10 Knife Edge—						
Total	112,112,839	112,097,194	71,342	111,918,092	112,242,571	
% in Aperture	86.67	86.72	.9	86.51	86.95	%
Peak	7.130e+02	7.096e+02	2.028e+00	7.050e+02	7.160e+02	
Min	2.370e+02	2.379e+02	1.528e+00	2.340e+02	2.420e+02	
Peak Loc X	2.670e+02	2.650e+02	2.087e+00	2.590e+02	2.700e+02	PX
Peak Loc Y	2.460e+02	2.434e+02	2.130e+00	2.390e+02	2.480e+02	PX
Centroid X	2.663e+02	2.661e+02	2.535e-01	2.654e+02	2.668e+02	PX
Centroid Y	2.425e+02	2.419e+02	4.123e-01	2.410e+02	2.428e+02	PX
Width X	6.109e+02	6.109e+02	2.257e-02	6.108e+02	6.109e+02	PX
Width Y	5.785e+02	5.785e+02	1.889e-01	5.781e+02	5.789e+02	PX
Diameter	5.947e+02	5.947e+02	9.832e-02	5.945e+02	5.949e+02	PX

(h) ν_{p}=10kHz, P=10.2W, @x_2

	Current	Mean	Deviation	Minimum	Maximum	Units
—Statistics—						
Samples	256	256	256	256	256	
—Quantitative—90/10 Knife Edge—						
Total	120,229,412	120,292,029	52,955	120,154,293	120,414,437	
% in Aperture	86.71	86.83	.8	86.50	86.97	%
Peak	6.600e+02	6.603e+02	1.842e+00	6.560e+02	6.660e+02	
Min	2.580e+02	2.578e+02	1.493e+00	2.530e+02	2.620e+02	
Peak Loc X	2.720e+02	2.716e+02	3.336e+00	2.620e+02	2.820e+02	PX
Peak Loc Y	2.540e+02	2.500e+02	4.089e+00	2.360e+02	2.590e+02	PX
Centroid X	2.677e+02	2.677e+02	1.704e-01	2.672e+02	2.681e+02	PX
Centroid Y	2.431e+02	2.428e+02	4.576e-01	2.418e+02	2.438e+02	PX
Width X	6.174e+02	6.174e+02	1.719e-02	6.173e+02	6.174e+02	PX
Width Y	5.834e+02	5.834e+02	1.734e-01	5.830e+02	5.837e+02	PX
Diameter	6.004e+02	6.004e+02	8.918e-02	6.002e+02	6.005e+02	PX

(i) ν_{p}=10kHz, P=10.2W, @x_3

	Current	Mean	Deviation	Minimum	Maximum	Units
—Statistics—						
Samples	256	256	256	256	256	
—Quantitative—90/10 Knife Edge—						
Total	92,212,182	92,352,148	99,129	92,162,832	92,567,071	
% in Aperture	86.65	86.65	.10	86.50	86.78	%
Peak	9.060e+02	9.126e+02	4.303e+00	9.020e+02	9.240e+02	
Min	1.920e+02	1.922e+02	1.240e+00	1.890e+02	1.960e+02	
Peak Loc X	2.770e+02	2.795e+02	2.979e+00	2.700e+02	2.870e+02	PX
Peak Loc Y	2.540e+02	2.522e+02	1.547e+00	2.480e+02	2.560e+02	PX
Centroid X	2.779e+02	2.774e+02	3.342e-01	2.767e+02	2.782e+02	PX
Centroid Y	2.515e+02	2.508e+02	3.810e-01	2.498e+02	2.516e+02	PX
Width X	5.750e+02	5.748e+02	2.256e-01	5.744e+02	5.754e+02	PX
Width Y	5.362e+02	5.358e+02	4.399e-01	5.347e+02	5.368e+02	PX
Diameter	5.556e+02	5.553e+02	2.976e-01	5.546e+02	5.560e+02	PX

(j) ν_{p}=10kHz, P=94W, @x_1

	Current	Mean	Deviation	Minimum	Maximum	Units
—Statistics—						
Samples	256	256	256	256	256	
—Quantitative—90/10 Knife Edge—						
Total	137,725,070	138,296,645	366,694	137,607,934	138,993,343	
% in Aperture	86.52	86.62	.7	86.50	86.75	%
Peak	9.330e+02	9.394e+02	4.422e+00	9.270e+02	9.490e+02	
Min	2.260e+02	2.288e+02	1.658e+00	2.240e+02	2.330e+02	
Peak Loc X	3.000e+02	2.921e+02	5.424e+00	2.800e+02	3.050e+02	PX
Peak Loc Y	2.970e+02	2.966e+02	2.559e+00	2.870e+02	3.040e+02	PX
Centroid X	2.870e+02	2.869e+02	2.365e-01	2.864e+02	2.875e+02	PX
Centroid Y	2.708e+02	2.705e+02	3.876e-01	2.696e+02	2.712e+02	PX
Width X	6.026e+02	6.023e+02	2.092e-01	6.019e+02	6.028e+02	PX
Width Y	5.573e+02	5.570e+02	3.293e-01	5.562e+02	5.579e+02	PX
Diameter	5.799e+02	5.797e+02	2.407e-01	5.791e+02	5.803e+02	PX

(k) ν_{p}=10kHz, P=94W, @x_2

	Current	Mean	Deviation	Minimum	Maximum	Units
—Statistics—						
Samples	256	256	256	256	256	
—Quantitative—90/10 Knife Edge—						
Total	110,667,047	110,944,522	131,620	110,652,230	111,264,455	
% in Aperture	86.93	86.74	.13	86.50	86.96	%
Peak	5.940e+02	5.998e+02	2.069e+00	5.940e+02	6.070e+02	
Min	2.290e+02	2.308e+02	1.366e+00	2.270e+02	2.350e+02	
Peak Loc X	2.800e+02	2.791e+02	1.111e+01	2.540e+02	3.230e+02	PX
Peak Loc Y	3.700e+02	3.533e+02	2.427e+01	2.580e+02	3.760e+02	PX
Centroid X	2.869e+02	2.868e+02	3.809e-01	2.859e+02	2.878e+02	PX
Centroid Y	2.666e+02	2.674e+02	4.754e-01	2.662e+02	2.685e+02	PX
Width X	6.188e+02	6.187e+02	6.218e-02	6.186e+02	6.189e+02	PX
Width Y	5.757e+02	5.753e+02	2.169e-01	5.747e+02	5.759e+02	PX
Diameter	5.972e+02	5.970e+02	1.208e-01	5.967e+02	5.973e+02	PX

(l) ν_{p}=10kHz, P=94W, @x_3

Figure F.3: Raw statistics corresponding to the laser-beam images shown in Fig. F.2. (cont.)

F.3 Laser vital point: the temperature of the frequency-doubling crystal

The conversion from the fundamental 1053 nm to the second harmonic 527 nm is performed via a temperature-controlled Lithium Triborate (LBO) nonlinear optical crystal. A vital (for the laser) point mentioned in the laser manual needs more emphasis: under any given operating conditions (given by a couple of values for the two parameters repetition rate and power), the temperature of the LBO crystal must be such that the conversion efficiency is high. The optimum temperatures, T_{LBO} (for which the conversion efficiency is the highest), were therefore mapped for every repetition rate of interest at variable power, starting at low power and slowly incresing power via the diode current, I_{real}. Tables F.1–F.7 (last updated on 2006/05/19) show the results of this mapping in single-pulse mode. In these tables, I_{set} is the diode-current setpoint adjustable via the laser control software, $QSPW$ is the Q-switch pulse width used in the external trigger signal, P is the measured laser power, E is the corresponding pulse energy ($E = P \times \nu_{\mathrm{p}}$), and PW is the measured pulse width. The range of optimum temperatures, T_{LBO} shortens when power is increased, therefore the risk of non-optimum conversion is higher while operating at high power, which could result in optical damage. Operating the laser with confidence requires prior mapping of T_{LBO}.

The LBO crystal should be constantly maintained at the optimum temperature, T_{LBO} (between 310 °F and 340 °F), even when the laser is not in use. If necessary, the temperature of the LBO crystal can be ramped down (typically no faster than 10 °F per minute to prevent cracking of the LBO crystal antireflection coatings) to room temperature for long-term storage of the laser or before an anticipated power interruption.

While operating with the LBO-crystal-temperature optimum value, an additional way to increase the output power by a small amount is to modify slightly the Q-switch trigger pulse width. Generally, a value of 5 μs should be used, but smaller values can lead to increased output power under certain operating conditions. However decreasing the Q-switch trigger pulse width too much can be detrimental to the laser-ouput stability.

As can be seen in Tables F.1–F.7, the laser-ouput repetition rate can be unstable at low power. The actual laser-ouput repetition rate is essential in the determination of the velocity (see Section. 5.2). Therefore, a Thorlabs DET10A photodiode was used to monitor the output-pulses actual repetition rate and stability while mapping $\mathrm{T_{LBO}}$. Thus, it was discovered that the actual repetition rate (measured by the photodiode) can differ from the desired repetition rate (set via, and equal to the Q-switch triggering signal frequency) at low power. For example, setting the Q-switch triggering signal frequency to 10 kHz will generate pulses with an unstable repetition rate jumping between 5 and 10 kHz for powers smaler than 6 W (see F.5), whereas the observed repetition rate becomes a rock-steady 10 kHz for powers $\gtrsim$ 11 W. Between 6 W and 11 W, the repetition rate is 10 kHz but there

are amplitude and width differences between odd and even pulses. For powers $\gtrsim 11\,\mathrm{W}$, differences are not noticeable between odd and even pulses.

I_{set} (A)	I_{real} (A)	$QSPW$ (μs)	T_{LBO} (°F)	P (W)	E (mJ/pulse)	PW (ns)	Stability
11.3	11.45	5	317.0	7.0	7.0	-	-
12.4	12.5	5	317.0	10.2	10.2	-	-
13.4	13.55	5	317.0	13.3	13.3	-	-
14.5	14.65	5	316.5	16.7	16.7	-	-
15.5	15.7	5	316.5	19.6	19.6	-	-

Table F.1: Optimum temperatures of the frequency-doubling crystal in single-pulse mode at 1 kHz.

I_{set} (A)	I_{real} (A)	$QSPW$ (μs)	T_{LBO} (°F)	P (W)	E (mJ/pulse)	PW (ns)	Stability
9.4	9.5	5	317.5	1.3	0.7	980	stable 2 kHz
9.8	10.0	5	317.5	2.7	1.4	810	stable 2 kHz
10.4	10.6	5 / 4.2	317.0	4.96 / 4.99	2.5	630 /610	stable 2 kHz
10.9	11.05	5 / 3.8	316.5	6.97 / 7.00	3.5	510 /500	stable 2 kHz
11.3	11.45	5	316.5	8.8	4.4	470	stable 2 kHz

Table F.2: Optimum temperatures of the frequency-doubling crystal in single-pulse mode at 2 kHz.

I_{set} (A)	I_{real} (A)	$QSPW$ (μs)	T_{LBO} (°F)	P (W)	E (mJ/pulse)	PW (ns)	Stability
11.3	11.45	5	316.1	11.6	3.9	-	-
12.4	12.5	5	315.7	17.8	5.9	-	-
13.4	13.55	5	315.6	22.4	7.5	-	-
14.5	14.65	5	314.8	29.7	9.9	-	-
15.5	15.7	5	314.5	37.8	12.6	-	-
16.6	16.75	5	314.2	44.4	14.8	-	-
17.6	17.8	5	313.8	51.6	17.2	-	-
15.5	15.7	5	313.3	58.9	19.6	-	-

Table F.3: Optimum temperatures of the frequency-doubling crystal in single-pulse mode at 3 kHz.

I_{set} (A)	I_{real} (A)	$QSPW$ (μs)	T_{LBO} (°F)	P (W)	E (mJ/pulse)	PW (ns)	Stability
9.4	9.5	5	317.0	1.3	0.3	-	unstable 2.5 kHz
9.8	10.0	5 / 5.7	317.0	2.53 / 2.61	0.5	690 / 960	stable 5 kHz
10.4	10.6	5 / 4.5	317.0	4.91 / 4.96	1.0	790 /740	stable 5 kHz
10.9	11.05	5 / 4.0	316.5	7.04 / 7.26	1.4	730 /640	stable 5 kHz
11.3	11.45	5 / 3.8	316.0	9.04 / 9.34	1.8 / 1.9	660 /570	stable 5 kHz
11.9	12.05	5	315.5	12.2	2.4	580	stable 5 kHz
12.4	12.5	5	315.5	14.8	3.0	550	stable 5 kHz
12.9	13.05	5	315.5	17.8	3.6	510	stable 5 kHz
13.4	13.55	5	315.0	20.8	4.2	470	stable 5 kHz
14.0	14.15	5	314.7	24.5	4.9	440	stable 5 kHz
14.5	14.65	5	314.5	27.5	5.5	410	stable 5 kHz
15.5	15.7	5	315.2	34.8	7.0	-	stable 5 kHz
16.6	16.75	5	314.6	43.0	8.6	-	stable 5 kHz
17.6	17.8	5	314.3	51.2	10.2	-	stable 5 kHz
18.7	18.85	5	312.8	62.0	12.4	-	stable 5 kHz
19.7	19.9	5	312.5	69.0	13.8	-	stable 5 kHz

Table F.4: Optimum temperatures of the frequency-doubling crystal in single-pulse mode at 5 kHz.

I_{set} (A)	I_{real} (A)	$QSPW$ (μs)	T_{LBO} (°F)	P (W)	E (mJ/pulse)	PW (ns)	Stability
9.4	9.5	5	317.2	0.9	0.1	-	unstable 5 kHz
9.8	10.0	5	317.2	2.6	0.3	-	unstable 5 kHz
10.4	10.6	5	316.6	4.9	0.5	-	unstable 5 kHz
10.9	11.05	5	316.3	6.2	0.6	-	stable 10 kHz, but differences between even and odd pulses
11.3	11.45	5 / 4.7	315.7	7.99 / 8.03	0.8	780 /700	stable 10 kHz, but tiny differences between even and odd pulses
11.9	12.05	5 / 4.2	315.5	10.8 / 11.2	1.1	730 / 630	stable 10 kHz
12.4	12.5	5 / 3.9	314.8	13.0 / 13.6	1.3 / 1.4	710 / 570	stable 10 kHz
12.9	13.05	5 / 3.7	314.5	15.5 / 16.5	1.5 / 1.6	680/540	stable 10 kHz
13.4	13.55	5	314.0	18.1	1.8	-	stable 10 kHz
14.0	14.15	5	314.0	21.5	2.2	-	stable 10 kHz
14.5	14.65	5	314.0	24.3	2.4	-	stable 10 kHz
15.0	15.15	5	313.5	27.5	2.8	-	stable 10 kHz
15.5	15.7	5	313.3	30.5	3.1	-	stable 10 kHz
16.0	16.15	5	313.0	33.3	3.3	-	stable 10 kHz
16.6	16.75	5	312.6	37.1	3.7	-	stable 10 kHz
17.1	17.25	5	312.3	40.2	4.0	-	stable 10 kHz
17.6	17.8	5	312.1	43.4	4.3	-	stable 10 kHz
18.2	18.45	5	311.8	47.4	4.7	-	stable 10 kHz
18.7	18.85	5	311.5	50.3	5.0	-	stable 10 kHz
19.2	19.4	5	311.3	53.4	5.3	-	stable 10 kHz
19.7	19.9	5	311.0	56.4	5.6	-	stable 10 kHz
20.3	20.5	5	311.0	59.8	6.0	-	stable 10 kHz
20.8	21.0	5	311.0	62.6	6.3	-	stable 10 kHz
23.0	-	5	309.0	97.0	9.7	-	stable 10 kHz

Table F.5: Optimum temperatures of the frequency-doubling crystal in single-pulse mode at 10 kHz.

I_{set} (A)	I_{real} (A)	$QSPW$ (μs)	T_{LBO} ($^{\circ}$F)	P (W)	E (mJ/pulse)	PW (ns)	Stability
9.4	9.5	5	317.2	0.6	0.0	-	unstable 7.5 kHz
9.8	10.0	5	317.0	1.9	0.1	-	unstable 7.5 kHz
10.4	10.6	5	316.5	4.4	0.3	-	unstable 7.5 kHz
10.9	11.05	5	316.2	6.5	0.4	-	unstable 7.5 kHz
11.3	11.45	5	315.9	8.4	0.6	-	unstable 7.5 kHz
11.9	12.05	5	315.9	10.1	0.7	-	unstable 7.5 kHz
12.4	12.5	5	314.5	11.9	0.8	-	stable 15 kHz, but differences between even and odd pulses
12.9	13.05	5	314.5	14.2	0.9	-	stable 15 kHz, but small differences between even and odd pulses
13.4	13.55	5	314.0	16.6	1.1	-	stable 15 kHz, but tiny differences between even and odd pulses
14.0	14.15	5 / 4.2	314.0	19.5 / 20.6	1.3 / 1.4	720 / 620	stable 15 kHz & no pulse differences / stable 15 kHz & tiny pulse differences
14.5	14.65	5 / 3.8	313.4	21.7 / 23.4	1.4 / 1.6	700 / 560	stable 15 kHz & no pulse differences / stable 15 kHz & tiny pulse differences
15.0	15.15	5 / 3.6	313.2	24.2 / 26.6	1.6 / 1.8	670 / 520	stable 15 kHz & no pulse differences / stable 15 kHz & tiny pulse differences

Table F.6: Optimum temperatures of the frequency-doubling crystal in single-pulse mode at 15 kHz. (Note: if $QSPW$ is decreased further, power increases slightly but stability deteriorates quickly.)

I_{set} (A)	I_{real} (A)	$QSPW$ (μs)	T_{LBO} ($^{\circ}$F)	P (W)	E (mJ/pulse)	PW (ns)	Stability
9.4	9.5	5	317.2	0.3	0.0	-	weak and unstable pulses
9.8	10.0	5	317.0	1.5	0.1	-	unstable 10 kHz
10.4	10.6	5	317.0	3.8	0.2	-	unstable 10 kHz
10.9	11.05	5	316.0	6.1	0.3	-	unstable 10 kHz
11.3	11.45	5	315.8	8.1	0.4	-	unstable 10 kHz
11.9	12.05	5	315.2	10.8	0.5	-	unstable 10 kHz
12.4	12.5	5	315.0	12.9	0.6	-	unstable 10 kHz
12.9	13.05	5	314.5	14.3	0.7	-	stable 20 kHz, but very large differences between even and odd pulses
13.4	13.55	5	313.9	15.4	0.8	-	stable 20 kHz, but large differences between even and odd pulses
14.0	14.15	5	313.7	17.9	0.9	760	stable 20 kHz, but differences between even and odd pulses
14.5	14.65	5 / 4.6	313.4	20.1 / 20.8	1.0 / 1.0	720 / 700	stable 20 kHz, but small differences between even and odd pulses
15.0	15.15	5 / 4.1	312.8	22.5 / 23.8	1.1 / 1.2	730 / 580	stable 20 kHz
15.5	15.7	5 / 3.9	312.8	24.7 / 26.9	1.2 / 1.3	710 / 560	stable 20 kHz

Table F.7: Optimum temperatures of the frequency-doubling crystal in single-pulse mode at 20 kHz.

F.4 Double-pulse operating (DPO) mode

The double-pulse operating (DPO) mode allows shorter pulse separations than those corresponding to the sustained repetition rate 1–20 kHz by triggering the Q-switch with a signal containing 2 successive pulses at a given frequency. Such a capability is useful in particle image velocimetry (PIV) type measurements. The advertised pulse separation can be adjusted between 5–150 μs, which corresponds to 6.7 kHz – 200 kHz. However, in practice, finding the right settings for stable double-pulse operation (the 2nd pulse only appears above a certain power that depends on the repetition rate used) can be difficult, especially at low pulse separations. Tables F.8–F.9 show a few combinations of settings for which stable double-pulse operation was obtained, down to a pulse separation of 1.28 μs (corresponding to 780 kHz) with a repetition rate of 10 kHz. $QSPW_1$ and $QSPW_2$ are the Q-switch-trigger first and second pulse widths, the pulse separation between them is also set in the Q-switch trigger signal, and the Amplitude & pulse width, PW, of the ouput pulses are measured with a photodiode. Adjusting $QSPW_1$ and $QSPW_2$ allows some flexibility in the energy balance between the two pulses (pulse energy proportional to $Amplitude \times PW$). The energy balance depends on the total energy in the two pulses. Working with a total energy of 10 mJ should allow the balance to be maintained within $\tilde{1}0\%$ over all specified repetition rates (5–10 kHz) and pulse separations (5–150 μs). However, for example with a repetition rate of 5 kHz, if the total energy is 15 mJ, the balance can be $< 20\%$ for pulse separations $>10\,\mu$s but the system appears to be overdriven, and for pulse separations $<10\,\mu$s, the balance can degrade to $\sim 80\,\% / 20\,\%$ or worse.

A DPO-Q-switch-trigger box coming with the laser can be used to generate the Q-switch trigger signal in DPO mode, however, I would advise generating the Q-switch-trigger signal with a flexible signal generator given that the Coherent DPO-Q-switch-trigger box is limited in the number of values that can be set for $QSPW_1$, $QSPW_2$, and the pulse separation.

My guess is that the laser could allow a burst of more than 2 pulses, but I would strongly advise prior discussions with the laser designer before attempting to find the right settings for such multi-pulse operation mode, which can be dangerous for the laser.

I_{set} (A)	I_{real} (A)	$QSPW_1$ (μs)	*Pulse Separation* (μs)	$QSPW_2$ (μs)	T_{LBO} ($^{\circ}$F)	P (W)	Amplitude - PW of 1^{st} / 2^{nd} pulse (mV) - (ns) / (mV) - (ns)	*Energy balance* between 1^{st} / 2^{nd} pulse
12.4	12.5	2.55	50	5.1	315.0	14.0	same - 400 / same - 400	50 % / 50 %

Table F.8: Optimum temperatures of the frequency-doubling crystal and energy balance between 1^{st} and 2^{nd} pulse in double-pulse mode at 5 kHz. (Note: the 2^{nd} pulse will not appear below 14 W.)

I_{set} (A)	I_{real} (A)	$QSPW_1$ (μs)	*Pulse Separation* (μs)	$QSPW_2$ (μs)	T_{LBO} (°F)	P (W)	Amplitude - PW of 1^{st} / 2^{nd} pulse (mV) - (ns) / (mV) - (ns)	*Energy balance* between 1^{st} / 2^{nd} pulse
18.7	18.85	2.55	40.00	2.73	310.0	49.0	$\simeq$same - 200 / $\simeq$same - 250	$\simeq 50\,\%$ / $50\,\%$
18.7	18.85	2.22	1.28	5.10	309.1	-	17.5 - 190 / 10 - 400	$45\,\%$ / $55\,\%$

Table F.9: Optimum temperatures of the frequency-doubling crystal and energy balance between 1^{st} and 2^{nd} pulse in double-pulse mode at 10 kHz.

Bibliography

Appel, J., Bockhorn, H., & Frenklach, M., 2000. Kinetic modeling of soot formation with detailed chemistry and physics: laminar premixed flames of C_2 hydrocarbons. *Combust. Flame*, **121**:122–136. available at <http://www.me.berkeley.edu/soot/mechanisms/abf.html>.

Barbe, P., Battin-Leclerc, F., & Come, G. M., 1995. Experimental and modeling study of methane and ethane oxidation between 773 and 1573 K. *J. Chim. Phys.*, **92**:1666–1692. available at <http://www.ensic.u-nancy.fr/DCPR/Anglais/GCR/softwaresdescription/base.htm>.

Bauge, J. C., Glaude, P. A., Pommier, P., Battin-Leclerc, F., Scacchi, G., Come, G. M., & Paillard, C., 1997. Experimental and modeling study of the effect of CF_3H, C_2F_6 and CF_3Br on the ignition dalays of methane-oxygen-argon mixtures behind shock waves. *J. Chim. Phys.*, **94**:460–476.

Baulch, D. L., Cobos, C. J., Cox, R. A., Franck, P., Hayman, G. D., Just, T., Kerr, J. A., Murrells, T. P., Pilling, M. J., Troe, J., Walker, R. W., & Warnatz, J., 1994. Summary table of evaluated kinetic data for combustion modeling — supplement-1. *Combust. Flame*, **98**:59–79.

Benezech, L. J., Bergthorson, J. M., & Dimotakis, P. E., 2006. Experimental investigation of planar strained methane-air and ethylene-air flames. *Technical report GALCITFM:2006.002*, California Institute of Technology. available at <http://resolver.caltech.edu/CaltechGALCITFM:2006.002>.

Benezech, L. J., Bergthorson, J. M., & Dimotakis, P. E., 2008. Premixed laminar C_3H_8- and C_3H_6-air stagnation flames: experiments and simulations with detailed kinetic models. *Proc. Combust. Inst.*, **32**:, *(accepted for presentation).*

Bergthorson, J. M., 2005a. *Experiments and Modeling of Impinging Jets and Premixed Hydrocarbon Stagnation Flames.* Ph.D. thesis, California Institute of Technology. available at <http://resolver.caltech.edu/CaltechETD:etd-05242005-165713>.

Bergthorson, J. M., 2005b. Premixed stagnation flame data and boundary conditions. available at <http://caltechblob.library.caltech.edu/4/01/Premixed_Flame_Data.htm>.

Bergthorson, J. M. & Dimotakis, P. E., 2006. Particle velocimetry in high-gradient/-curvature flows. *Exp. Fluids*, **41**:255–263.

Bergthorson, J. M. & Dimotakis, P. E., 2007. Premixed laminar C_1-C_2 stagnation flames: experiments and simulations with detailed thermochemistry models. *Proc. Combust. Inst.*, **31**: 1139–1147.

Bergthorson, J. M. & Dimotakis, P. E., 2008. Stagnation-flame experiments and combustion model validation. *Combust. Flame.* , *(submitted for publication).*

Bergthorson, J. M., Goodwin, D. G., & Dimotakis, P. E., 2005a. Particle streak velocimetry and CH laser-induced fluorescence diagnostics in strained, premixed, methane-air flames. *Proc. Combust. Inst.*, **30**:1637–1644.

Bergthorson, J. M., Sone, K., Mattner, T. W., Dimotakis, P. E., Goodwin, D. G., & Meiron, D. I., 2005b. Impinging laminar jets at moderate Reynolds numbers and separation distances. *Phys. Rev. E*, **72**. Art. No. 066307 Part 2.

Bowman, C. T., Hanson, R. K., Davidson, D. F., Gardiner, W. C., Lissianski, V., Smith, G. P., Golden, D. M., Frenklach, M., & Goldenberg, M. Gri-mech 2.11. available at <http://www.me.berkeley.edu/gri_mech/>.

Bradley, D., Gaskell, P. H., & Gu, X. J., 1996. Burning velocities, Markstein lengths, and flame quenching for spherical methane-air flames: A computational study. *Combust. Flame*, **104**: 176–198.

Carter, C. D., Donbar, J. M., & Driscoll, J. F., 1998. Simultaneous CH planar laser-induced fluorescence and particle imaging velocimetry in turbulent nonpremixed flames. *Appl. Phys. B*, **66**:129–132.

Castaldi, M. J., Marinov, N. M., Melius, C. F., Huang, J., Senkan, S. M., Pitz, W. J., & Westbrook, C. K., 1996. Experimental and modeling investigation of aromatic and polycyclic aromatic hydrocarbon formation in a premixed ethylene flame. *Proc. Combust. Inst.*, **26**:693–702.

Crosley, D. R., 1989. Semiquantitative laser-induced fluorescence in flames. *Combust. Flame*, **78**: 153–167.

Dagaut, P., 2002. On the kinetics of hydrocarbons oxidation from natural gas to kerosene and diesel fuel. *Phys. Chem. Chem. Phys.*, **4**:2079–2094.

Dagaut, P. & Hadj, K., 2003. Kinetics of oxidation of a LPG blend mixture in a JSR: Experimental and modeling study. *Fuel*, **82**:475–480.

Dagaut, P. & Nicolle, A., 2005. Experimental and detailed kinetic modeling study of hydrogen-enriched natural gas blend oxidation over extended temperature and equivalence ratio ranges. *Proc. Combust. Inst.*, **30**:2631–2638.

Davis, S. G., Law, C. K., & Wang, H., 1999. Propene pyrolysis and oxidation kinetics in a flow reactor and laminar flames. *Combust. Flame*, **119**:375–399. available at <http://ame-www.usc.edu/research/combustion/combustionkinetics/c3_download.html>.

Dewitt, F. P. & Incropera, D. P., 1990. In *Fundamentals of Heat and Mass Transfer, 3rd edition*. John Wiley & Sons Inc.

Egolfopoulos, F. N. & Dimotakis, P. E., 1998. Non-premixed hydrocarbon ignition at high strain rates. *Proc. Combust. Inst.*, **27**:641–648.

Egolfopoulos, F. N. & Dimotakis, P. E., 2001. A comparative numerical study of premixed and non-premixed ethylene flames. *Combust. Sci. Technol.*, **162**:19–35.

Egolfopoulos, F. N., Zhang, H., & Zhang, Z., 1997. Wall effects on the propagation and extinction of steady, strained, laminar premixed flames. *Combust. Flame*, **109**:237–252.

Ern, A. & Giovangigli, V., 1999. Impact of detailed multicomponent transport on planar and counterflow hydrogen/air and methane/air flames. *Combust. Sci. Technol.*, **149**:157–181.

Feeley, R., Seiler, P., Packard, A., & Frenklach, M., 2004. Consistency of a reaction dataset. *J. Phys. Chem. A*, **108**:9573–9583.

Frenklach, M., 1984. Modeling. In *Combustion Chemistry*, W. C. Gardiner Jr. (Ed.), Chapter 7, pages 423–453. Springer-Verlag, New York.

Frenklach, M., Packard, A., Seiler, P., & Feeley, R., 2004. Collaborative data processing in developing predictive models of complex reaction systems. *Int. J. Chem. Kinet.*, **36**:57–66.

Frenklach, M., Wang, H., Goldenberg, M., Smith, G. P., Golden, D. M., Bowman, C. T., Hanson, R. K., Gardiner, W. C., & Lissianski, V., 1995. Gri-mech — an optimized detailed chemical reaction mechanism for methane combustion. *Technical report GRI-95/0058*, Gas Research Institute.

Frenklach, M., Wang, H., & Rabinowitz, M. J., 1992. Optimization and analysis of large chemical kinetic mechanisms using the solution mapping method — combustion of methane. *Prog. Energy Combust. Sci.*, **18**:47–73.

Frenklach, M., Wang, H., Yu, C.-L., Goldenberg, M., Bowman, C. T., Hanson, R. K., Davidson, D. F., Chang, E. J., Smith, G. P., Golden, D. M., Gardiner, W. C., & Lissianski, V. Gri-mech 1.2. available at <http://www.me.berkeley.edu/gri_mech/>.

Gardiner-Jr., W. C., 1999. Hydrocarbon combustion chemistry. In *Gas-Phase Combustion Chemistry*, 2nd ed. W. C. Gardiner Jr. (Ed.), Chapter 1, page 33. Springer-Verlag, New York.

Gardiner-Jr., W. C. & Troe, J., 1984. Rate coefficients of thermal dissociation, isomerization, and recombination reactions. In *Combustion Chemistry*, W. C. Gardiner Jr. (Ed.), Chapter 4, pages 173–196. Springer-Verlag, New York.

Goodwin, D. G. Cantera object-oriented software for reacting flows. <http://www.cantera.org/>.

Goodwin, D. G., 2003. An open-source, extensible software suite for CVD process simulation. In *Proc. of CVD XVI and EuroCVD Fourteen,* Electrochem. Soc., pages 155–162.

Gueniche, H. A., Glaude, P. A., Dayma, G., Fournet, R., & Battin-Leclerc, F., 2006. Rich methane premixed laminar flames doped with light unsaturated hydrocarbons i. allene and propyne. *Combust. Flame*, **146**:620–634.

Hughes, K. J., Turányi, T., Clague, A. R., & Pilling, M. J., 2001. Development and testing of a comprehensive chemical mechanism for the oxidation of methane. *Int. J. Chem. Kinet.*, **33**: 513–538.

Jomaas, G., Zheng, X. L., Zhu, D. L., & Law, C. K., 2005. Experimental determination of counterflow ignition temperatures and laminar flame speeds of C_2–C_3 hydrocarbons at atmospheric and elevated pressures. *Proc. Combust. Inst.*, **30**:193–200.

Kee, R. J., Coltrin, M. E., & Glarborg, P., 2003. *Chemically Reacting Flow — Theory & Practice*. John Wiley & Sons, Hoboken, NJ.

Kee, R. J., Miller, J. A., Evans, G. H., & Dixon-Lewis, G., 1989. A computational model of the structure and extinction of strained, opposed flow, premixed methane-air flames. *Proc. Combust. Inst.*, **22**:1479–1494.

Konnov, A. A., 2000. Detailed reaction mechanism for small hydrocarbons combustion, version 0.5. available at <http://homepages.vub.ac.be/∼akonnov/>.

Laskin, A. & Wang, H., 1999. On initiation reactions of acetylene oxidation in shock tubes. *Chem. Phys. Lett.*, **303**:43–49.

Marinov, N. M., 1998. A detailed chemical kinetic model for high temperature ethanol oxidation. *Int. J. Chem. Kinet.*, **31**:183–220.

Marinov, N. M., Castaldi, M. J., Melius, C. F., & Tsang, W., 1997. Aromatic and polycyclic aromatic hydrocarbon formation in a premixed propane flame. *Combust. Sci. Technol.*, **128**:295–342.

Marinov, N. M. & Malte, P., 1995. Ethylene oxidation in a well-stirred reactor. *Int. J. Chem. Kinet.*, **27**:957–986.

Marinov, N. M., Pitz, W. J., Westbrook, C. K., Castaldi, M. J., & Senkan, S. M., 1996a. Modeling of aromatic and polycyclic aromatic hydrocarbon formation in premixed methane and ethane flames. *Combust. Sci. Technol.*, **116**:211–287.

Marinov, N. M., Westbrook, C. K., & Pitz, W. J., 1996b. Detailed and global chemical kinetics model for hydrogen. In *Transport phenomena in combustion*, S. H. Chen (Ed.), page 118. Eighth International Symposium on Transport Processes.

Markstein, G. H., 1951. Experimental and theoretical studies of flame-front stability. *J. Aeronaut. Sci.*, **18**:199–209.

Norton, T. S. & Smyth, K. C., 1991. Laser-induced fluorescence of CH^* in a laminar CH_4 / air diffusion flame: Implications for diagnostic measurements and analysis of chemical rates. *Combust. Sci. Technol.*, **76**:1–20.

Patera, A. T., 1984. A spectral element method for fluid dynamics: Laminar flow in a channel expansion. *J. Comput. Phys.*, **54**:468–488.

Rolland, S. & Simmie, J. M., 2004. The comparison of detailed chemical kinetic mechanisms: Application to the combustion of methane. *Int. J. Chem. Kinet.*, **36**:467–471.

San Diego mechanism, Center for Energy Research (Combustion Division), University of California at San Diego. available at <http://maeweb.ucsd.edu/∼combustion/cermech/>.

Smith, G. P., Golden, D. M., Frenklach, M., Moriarty, N. W., Eiteneer, B., Goldenberg, M., Bowman, C. T., Hanson, R. K., Song, S., Gardiner, W. C., Lissianski, V. V., & Qin, Z. Gri-mech 3.0. available at <http://www.me.berkeley.edu/gri_mech/>.

Sone, K., 2007. *Modeling and simulation of axisymmetric stagnation flames*. Ph.D. thesis, California Institute of Technology. available at <http://resolver.caltech.edu/CaltechETD:etd-04252007-170838>.

Sun, C. J., Sung, C. J., Wang, H., & Law, C. K., 1996. On the structure of nonsooting counterflow ethylene and acetylene diffusion flames. *Combust. Flame*, **107**:321–335.

Sutton, J. A. & Driscoll, J. F., 2003. Optimization of CH fluorescence diagnostics in flames: range of applicability and improvements with hydrogen addition. *Appl. Opt.*, **42**:2819–2828.

Tan, Y., Dagaut, P., Cathonnet, M., Boettner, J. C., Bachman, J. S., & Carlier, P., 1994. Natural gas and blends oxidation and ignition: experiments and modeling. *Proc. Combust. Inst.*, **25**:1563–1569.

Tsang, W., 1987. Chemical kinetic data base for combustion chemistry. part 2. methanol. *J. Phys. Chem. Ref. Data*, **16**:471–508.

Tsang, W. & Hampson, R. F., 1986. Chemical kinetic database for combustion chemistry. part 1. methane and related-compounds. *J. Phys. Chem. Ref. Data*, **15**:1087–1279.

Vagelopoulos, C. M., Egolfopoulos, F. N., & Law, C. K., 1994. Further considerations on the determination of laminar flame speeds with the counterflow twin-flame technique. *Proc. Combust. Inst.*, **25**:1341–1347.

Wang, H. & Frenklach, M., 1997. A detailed kinetic modeling study of aromatics formation in laminar premixed acetylene and ethylene flames. *Combust. Flame*, **110**:173–221. available at <http://www.me.berkeley.edu/soot/mechanisms/wf.html>.

Wang, H. & Laskin, A., 1998. A comprehensive kinetic model of ethylene and acetylene oxidation at high temperatures. , Internal report. available at <http://ame-www.usc.edu/research/combustion/combustionkinetics/c2_download.html>.

Warnatz, J., 1984. Rate coefficients in the C/H/O system. In *Combustion Chemistry*, W. C. Gardiner Jr. (Ed.), Chapter 5, pages 197–360. Springer-Verlag, New York.

Zádor, J., Zsély, I. G., Turányi, T., Ratto, M., Tarantola, S., & Saltelli, A., 2005. Local and global uncertainty analyses of a methane flame model. *J. Phys. Chem. A*, **109**:9795–9807.